UNCLASSIFIED

AD_____

DEFENSE DOCUMENTATION CENTER

FOR

SCIENTIFIC AND TECHNICAL INFORMATION

CAMERON STATION ALEXANDRIA. VIRGINIA

UNCLASSIFIED

DISCLAIMER NOTICE

ADVANCED RESEARCH

AB No. 218944

ASTIA FILE COPY

FC

FC
BAC

DIVISION OF HILLER AIRCRAFT

DYNAMIC STABILITY ANALYSIS

OF

DUCTED FAN TYPE FLYING PLATFORMS

CONTRACT NO. NONR 1357 (00)

PHASE IV

Report No. ARD-233

29 May 1959

DYNAMIC STABILITY ANALYSIS OF DUCTED FAN
TYPE FLYING PLATFORMS
Contract No. Nonr 1357(00), Phase IV

R. N. Greenman
M. G. Gaffney

ADVANCED RESEARCH
DIVISION OF HILLER AIRCRAFT CORPORATION

TABLE OF CONTENTS

Page

LIST OF TABLES

Table

LIST OF FIGURES

LIST OF FIGURES (cont.)

Figure

LIST OF FIGURES (cont.)

Figure

SUMMARY

An analysis is presented of the longitudinal dynamic stability characteristics in hovering and in level low-speed flight $(\lambda \leq .12)$, of the Hiller 7-foot diameter ducted fan flying platform. In addition, several configuration variations were investigated, including duct section and chord, number of propeller blades, propeller blade setting, and clearance between tips of propellers and inside of duct. The equations of motion are developed using standard methods. Time histories, obtained with an analog computer, and the resulting stability parameters are presented graphically. The present gyrobar stabilizer system provides sufficient damping in hovering flight but will not overcome the divergent motion in forward flight. For this reason, the dynamic characteristics deteriorate with increasing speed. This is primarily due to the static (angle-of-attack) instability which occurs at higher speeds.

1. INTRODUCTION

The use of a ducted propeller as a man carrying vehicle has been considered for the past few years by the Military. Various theoretical and experimental programs have been initiated to investigate the performance and stability and control characteristics of such a vehicle. This contractor was awarded a contract by the Office of Naval Research in 1954, Nonr 1357(00), to determine in part the flight characteristics of a personnel flying ducted propeller that was kinestheticly controlled. This means of control was conceived by Zimmerman of the NACA in 1952 (Ref. 1). It makes use of the same instinctive reactions a person uses to stand and walk. The pilot standing on the platform acts unconciously as an autopilot in counteracting any disturbance that might occur and for steady flight he simply shifts his weight by leaning in the direction of desired motion. This contractor has completed several phases of the subject contract in which stability and control analyses and flight test programs have been conducted on a 5-foot platform. The stability and control results of these various phases have indicated that the 5-foot platform can be controlled kinesthetically in hovering and low-speed forward flight in calm air but that problems arise in windy and gusty conditions, (see Ref. 2).

In order to improve the flight characteristics, a mechanical gyrobar stabilizer was developed which automatically applies corrective control application in both pitch and roll. This stabilizer, shown in Figure 1-A, is a system of two bars which rotate with the lower propeller and have the freedom to pivot relative to the propeller plane. On each end of the bars is an airfoil-shaped paddle to give aerodynamic damping. These stabilizer bars, excited by gyroscopic moments, actuate a set of pitch and roll vanes mounted below the platform. Figure 1-B shows the mechanical operation of the system for the case of the duct pitched down at the nose. The dash lines show the relative position of the bar and vanes to the duct and the force "L" thus produced by the vanes. This force of the vanes produces a damping moment opposing the pitching or rolling disturbances of the platform.

In order that a quantitative analysis of the platform stability and control problem might be carried out, a wind tunnel test program, additional flight tests, and theoretical studies were contracted for under Annex B to Contract No. Nonr 1357(00). The wind tunnel program consisted of testing various duct shapes, propellers, and centerbodies in many combinations at various angles of attack, propeller blade pitch settings and advance ratios (tunnel airspeed/propeller tip speed). Measurements were made of total lift, propulsive force, pitching moment, and power. Since the original 5-foot platform was underpowered it was redesigned into a 7-foot diameter vehicle capable of developing higher thrust.

1

In this report a dynamic stability analysis is performed for the 7-foot platform, shown in Figure 2, with and without the gyrobar stabilizer system and with various configuration changes, such as duct section and chord, number of propeller blades, propeller blade pitch setting, and clearance between tips of propellers and inside of duct. The stability derivatives used in the analysis are obtained from the wind tunnel tests conducted by Hiller Aircraft Corporation at David Taylor Model Basin during the period of June-September 1958; the results of those tests have been published in Reference 3.

Solutions to the stability equations are obtained on an analog computer with a pilot control step input and a horizontal gust pulse input as alternate excitation functions. These solutions yield stability characteristics, such as period of oscillation, damping factor, and percent overshoot. In addition, the stability characteristics for the ship are examined with the aid of vector diagrams and stability boundary charts.

2. LIST OF SYMBOLS

a_g Lift-curve slope of gyrobar paddle, rad^{-1}

a_p Lift-curve slope of propeller blade, rad^{-1}

a_v Lift-curve slope of slipstream vane, rad^{-1}

A_g Planform area of one gyrobar paddle, ft^2

A_v Planform area of one slipstreat control vane, ft^2 (there are 2 vanes each for pitch and roll)

b Total number of propeller blades

c Mean chord of propeller blade, ft

CG   Center of gravity of platform and pilot

F   Propulsive force, positive forward, lbs (see Sketch 1)

g Gravitational acceleration, (32.2 ft/sec^2)

I   Total moment of inertia in pitch of platform and pilot about center of gravity, lb ft sec^2

I_g Total moment of inertia of one gyrobar about its pivot, lb ft sec^2

k_F Propulsive force coefficient, $\dfrac{F}{\rho(\Omega R)^2 \pi R^2}$

k_L Lift coefficient, $\dfrac{L}{\rho(\Omega R)^2 \pi R^2}$

k_M Pitching moment coefficient, $\dfrac{M}{\rho(\Omega R)^2 \pi R^3}$

$k_{M_{\dot{u}}}$ Speed stability derivative in forward flight, $\dfrac{M_{\dot{u}}}{\rho(\Omega R)^2 \pi R^3}$

3

k_{M_u} Speed stability derivative in hovering, $\dfrac{M_u}{\rho(\Omega R)^2 \pi R^3}$

k_{M_w} Angle-of-attack stability derivative in forward flight, $\dfrac{M_w}{\rho(\Omega R)^2 \pi R^3}$

k_{M_δ} Gyrobar control effectiveness, $\dfrac{M_\delta}{\rho(\Omega R)^2 \pi R^3}$

k_{M_θ} Rotary damping in pitch, $\dfrac{M_{\dot\theta}}{\rho(\Omega R)^2 \pi R^3}$, sec

$k_{X_u} = \dfrac{X_u}{\rho(\Omega R)^2 \pi R^2}$

$k_{X_{\bar u}} = \dfrac{X_{\bar u}}{\rho(\Omega R)^2 \pi R^2}$

$k_{X_w} = \dfrac{X_w}{\rho(\Omega R)^2 \pi R^2}$

$k_{X_\delta} = \dfrac{X_\delta}{\rho(\Omega R)^2 \pi R^2}$

$k_{X_{\dot\theta}} = \dfrac{X_{\dot\theta}}{\rho(\Omega R)^2 \pi R^2}$, sec

$k_Y = \dfrac{I}{\rho(\Omega R)^2 \pi R^3}$, sec^2

$k_{Z_u} = \dfrac{Z_u}{\rho(\Omega R)^2 \pi R^2}$

$k_{Z_w} = \dfrac{Z_{\bar w}}{\rho(\Omega R)^2 \pi R^2}$

K   Specific damping (damping/critical damping) of gyrobar

KΩ Gyrobar damping term, $\dfrac{1}{2 I_g} \rho R_g^2 a_g (\Omega R_g) A_g$, sec^{-1}

ℓ Axial distance from the center of gravity (positive in direction of slipstream), ft

ℓ_0 Distance from shroud trailing edge to center of gravity, ft (see Sketch 2)

ℓ_1 Distance from shroud leading edge to center of gravity, ft (see Sketch 2)

ℓ_2 Axial component of shroud chord, ft (see Sketch 2)

ℓ_3 Distance from aerodynamic center of slipstream vane to shroud trailing edge, ft (see Sketch 2)

L   Total lift, lb (see Sketch 1)

M   Pitching moment about center of gravity, lb ft (see Sketch 1)

n   Linkage ratio between pitch vane angular displacement and gyrobar longitudinal tilt, vane deflection/gyrobar tilt

P   Power required, lb ft/sec

R   Propeller radius, ft

R_g Radius of center of lift of gyrobar paddle, ft

t   Time, sec

u,w   Perturbation velocities along the x and z axes, ft/sec (see Sketch 1)

$\bar{u},\bar{w}$ Perturbation velocities divided by equilibrium forward velocity

$\tilde{u}$ Perturbation velocity divided by tip speed

v_a Average axial velocity in the duct, ft/sec

V   Forward flight velocity, ft/sec

W   Gross weight, lb

x,z   Stability axes, fixed to the platform (see Sketch 1)

X,Z   Forces in x and z directions, lb

β Propeller blade pitch setting at 0.7 radius station, deg

γ   Platform angle of attack, zero if platform center line (propeller axis) is perpendicular to flight velocity, positive if platform is tilted to the rear, (see Sketch 1)
In steady level flight γ is also angle between vertical and propeller axis

δ   Perturbation displacement in fore-aft tilt of gyrobar tip path plane, positive if tip path plane is tilted to the rear, rad

ε   Forward flight efficiency, $\dfrac{LV}{P - FV}$

θ   Perturbation in platform attitude, rad (see Sketch 1)

λ   Advance ratio, $\dfrac{V}{\Omega R}$

μ   Average duct axial velocity divided by forward flight velocity

ρ   Density of air, assumed 0.00238 slugs/ft^3

σ   Solidity of the propellers, $\dfrac{bc}{\pi R}$

τ   Mass coefficient, $\dfrac{W}{g\rho(\Omega R)\pi R^2}$, sec

Ψ   Propeller blade azimuth angle measured from rear position in direction of rotation, rad

Ω   Propeller shaft angular velocity, sec^{-1}

Subscripts

ℓ_4 Quarter-chord of duct

u, w, θ, etc. indicate $\dfrac{\partial}{\partial u}$, $\dfrac{\partial}{\partial w}$, $\dfrac{\partial}{\partial \theta}$, etc.

Superscript dot indicates the time rate of change of the variable

6

CONFIGURATION NOTATION

D_1 Duct No. 1, Modified NACA 6421 profile (see Table 1)

D_2 Duct No. 2, NACA 0018 profile (see Table 2)

D_3 Duct No. 3, Modified lemniscate profile (see Table 3)

D_4 Duct No. 4, Modified NACA 6421 profile, 0.6 chord of D_1 (see Table 4)

HB   Indicates presence of simulated platform engines and pilot on wind-tunnel model

P_2 2-bladed twisted, contra-rotating propellers (see Tables 5 and 6)

P_3 3-bladed twisted, contra-rotating propellers (see Tables 5 and 6)

ΔR Indicates that average clearance (0.0038R) between duct and propeller tips has been doubled

V_0 Indicates presence of exit vanes at zero deflection angle with duct axis

7

3. THE EQUATIONS OF MOTION OF THE PLATFORM

For the investigation of the dynamic characteristics we use a right-handed system of axes which is fixed to the platform and has its origin at the CO of the manned aircraft. This system of axes, generally referred to as "body axes", is oriented in such a way that the positive x-axis falls in the direction of the initial, undisturbed flight velocity. For the investigation of the longitudinal dynamics in forward flight both the x- and z-axis lie in the longitudinal plane of symmetry where the positive direction of z is down, see Sketch 1.

The undisturbed flight condition is characterized by the velocity V and the attitude γ of the platform with reference to the vertical. By definition, γ is positive if the ship is tilted to the rear. In forward flight the platform must be tilted forward, therefore normal forward flight occurs at negative γ-values. For level forward flight the attitude or pitch angle γ is identical with the platform angle of attack.

The three degrees of freedom considered are:

u   translational perturbation velocity in direction of x

w   translational perturbation velocity in direction of z

θ angular disturbance in the attitude of the platform

The corresponding equations of motion are:

$$\sum X = 0$$
$$\sum Z = 0$$
$$\sum M = 0$$

By definition, the x-axis is given by the direction of the initial un-disturbed flight. Therefore, the translational velocity disturbance u changes the magnitude of the relative speed but not the angle of attack of the plat-form. On the other hand, provided that the disturbances are small, the trans-lational disturbance w changes the platform angle of attack but not the magni-tude of the relative velocity. As it is convenient to introduce the platform advance ratio $\lambda = V/\Omega R$, we can summarize the aerodynamic effects of the dis-turbances u an w as follows:
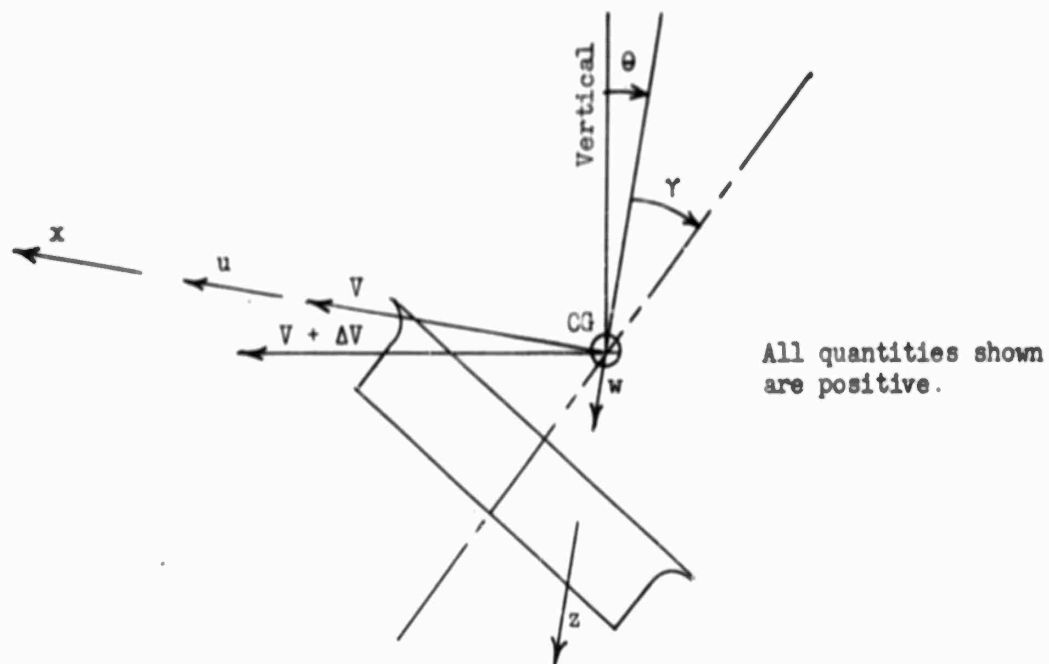
u results in a change $d\lambda$ of the advance ratio
$$d\lambda = u/\Omega R$$

w results in a change $d\gamma$ of the platform angle of attack
$$d\gamma = w/V .$$

8

a) STEADY STATE FLIGHT CONDITION
   (Level Flight)
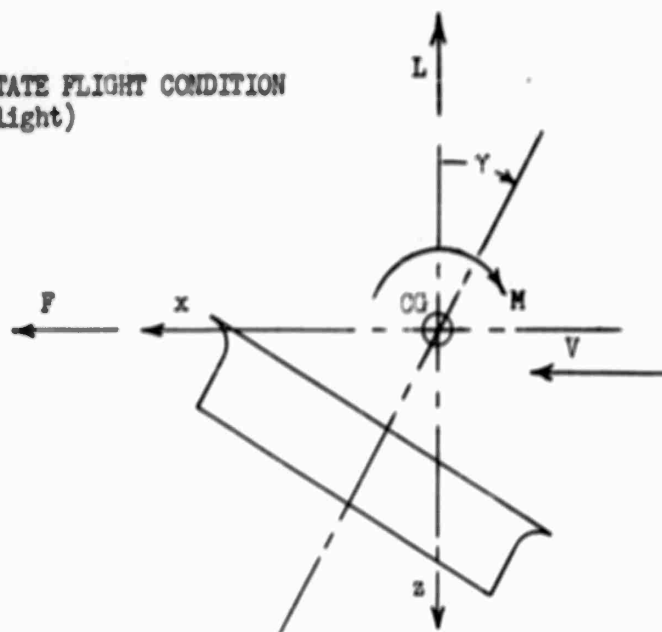
b) DISTURBED FLIGHT CONDITION

All quantities shown
are positive.

GROUND

SKETCH 1

9

The angular attitude disturbance Θ, as such, does not affect the aerodynamic forces. It will be shown later, however, that its rate of change $\dot{\Theta}$, ($\dot{\Theta}$ = pitching velocity) has a pronounced effect on both the X-force and the pitching moment M.

3.1 Hovering Flight

As there is no direction of undisturbed flight in hovering, the choice of the direction of axes becomes somewhat arbitrary. For convenience, we choose as z-axis the propeller axis, positive down; and as x-axis the normal to the z-axis in the longitudinal plane of symmetry, positive in the direction of conventional forward flight. As discussed previously, the system of axes is fixed to the aircraft. For symmetry reasons, $X_w = M_w = 0$ and the three equations of motions are no longer coupled. As any translational disturbance in the direction of z is damped ($Z_w < 0$), we can restrict ourselves in hovering to the degrees of freedom u and Θ, i.e., to the equations for the equilibrium of X-forces and pitching moments: (see also Ref. 4)

$$X_u u - \frac{W}{g} \dot{u} - W\Theta + X_{\dot{\Theta}}\dot{\Theta} = 0$$

$$M_u u + M_{\dot{\Theta}}\dot{\Theta} - I \ddot{\Theta} \quad = 0 \tag{1}$$

where

W is the gross weight of ship

I is the total moment of inertia in pitch about the CG of the aircraft

X_u, $X_{\dot{\Theta}}$, M_u, $M_{\dot{\Theta}}$ are the partial derivatives of the X-force and pitching moment with respect to u and $\dot{\Theta}$.

The gyrobar stabilizer system, with the longitudinal component of the gyrobar angular deflection δ, increases by one the number of degrees of freedom. Considering the effect of feedback in the gyrobar system to be negligible, the simplified equation of motion of the bars is (see Ref. 5)

$$\dot{\Theta} + K\Omega\delta + \dot{\delta} = 0 \tag{2}$$

where K is the specific damping of the gyrobar and Ω its angular velocity.

The cross-coupling between pitch and roll in the gyrobar system has been investigated and found to be quite small (in the order of one percent of the control application) for the expected platform frequencies of 3 radians per second or less. The gyrobars, by actuating vanes in the propeller slipstream, add aerodynamic feedback terms $X_\delta\delta$ and $M_\delta\delta$ to the platform equations.

10

Thus, the platform with stabilizer is characterized by the following set of equations:

$$X_u u - \frac{W}{g} \dot{u} - W\theta + X_{\dot\theta}\dot\theta + X_\delta\delta = 0$$

$$M_u u + M_{\dot\theta}\dot\theta - I\ddot\theta + M_\delta\delta \qquad = 0$$

$$\dot\theta + K\Omega\delta + \dot\delta \qquad = 0 \qquad (3)$$

In order to facilitate handling of the non-dimensional aerodynamic stability derivatives that will be obtained from the wind tunnel tests of Reference 3, it is convenient to non-dimensionalize the equations. This will be accomplished by dividing all forces by $\rho(\Omega R)^2 \pi R^2$ and all moments by $\rho(\Omega R)^2 \pi R^3$. In so doing, the set of equations becomes

$$k_{X_{\tilde{u}}}\tilde{u} - \tau\frac{d\tilde{u}}{dt} - k_L\theta + k_{X_{\dot\theta}}\dot\theta + k_{X_\delta}\delta = 0$$

$$k_{M_{\tilde{u}}}\tilde{u} + k_{M_{\dot\theta}}\dot\theta - k_Y\ddot\theta + k_{M_\delta}\delta \qquad = 0$$

$$\dot\theta + K\Omega\delta + \dot\delta \qquad = 0 \qquad (4)$$

where u has been made non-dimensional by dividing by the propeller tip speed, i.e., $\tilde{u} = \frac{u}{\Omega R}$.

3.2 Forward Flight

The equations of motion in the longitudinal plane for forward flight express the equilibrium of forces in the x and z directions and of pitching moments about the center of gravity. For level flight these equations are,

$$X_u u - \frac{W}{g}\dot{u} + X_w w - W\theta + X_{\dot\theta}\dot\theta + X_\delta\delta = 0$$

$$Z_u u + Z_w w - \frac{W}{g}\dot{w} + \frac{W}{g}V\dot\theta \qquad = 0$$

$$M_u u + M_w w + M_{\dot\theta}\dot\theta - I\ddot\theta + M_\delta\delta \qquad = 0$$

$$\dot\theta + K\Omega\delta + \dot\delta \qquad = 0 \qquad (5)$$

11

The last of these equations is again the simplified equation of motion for the gyrobar stabilizer.

Non-dimensionalized as in hovering, the equations become

$$k_{X_{\bar{U}}} \bar{U} - \tau\lambda \frac{d\bar{U}}{dt} + k_{X_{\bar{W}}} \bar{W} + k_L \theta + k_{X_{\dot{\theta}}} \dot{\theta} + k_{X_{\delta}} \delta = 0$$

$$k_{Z_{\bar{U}}} \bar{U} + k_{Z_{\bar{W}}} \bar{W} - \tau\lambda \frac{d\bar{W}}{dt} + \tau\lambda \dot{\theta} \qquad\qquad = 0$$

$$k_{M_{\bar{U}}} \bar{U} + k_{M_{\bar{W}}} \bar{W} + k_{M_{\dot{\theta}}} \dot{\theta} - k_Y \ddot{\theta} + k_{M_{\delta}} \delta \qquad = 0$$

$$\dot{\theta} + K\Omega\delta + \dot{\delta} \qquad\qquad\qquad\qquad = 0 \qquad\qquad (6)$$

where u and w have been made non-dimensional by dividing by the forward velocity, i.e., $\bar{U} = \frac{u}{V}$, $\bar{W} = \frac{w}{V}$.

Equations (4) and (6) now represent the equations of motion in the longitudinal plane for a 4-degree of freedom system symbolizing the platform with the gyrobar stabilizer. Note that in the hovering case the number of degrees of freedom is reduced by one. The remainder of this report is concerned with the determination of the required derivatives and the subsequent solution of these equations.

12

4. AERODYNAMIC STABILITY DERIVATIVES

In this section, expressions will be presented for the aerodynamic stability derivatives required in the solution of the equations of motion. The derivatives are divided into two groups; derivatives obtained directly from the wind tunnel data of Reference 3 and those for which mathematical expressions involving the data are to be developed.

The derivatives of the first group involve only the aerodynamic forces and the pitching moment of the platform and are easily found, from Sketch 1, to be

$$X_u = \frac{1}{2R} F_\lambda$$

$$X_w = \frac{1}{V} (L + F_\gamma)$$

$$Z_u = -\frac{1}{2R} L_\lambda$$

$$Z_w = -\frac{1}{V} L_\gamma$$

$$M_u = \frac{1}{2R} M_\lambda$$

$$M_w = \frac{1}{V} M_\gamma \tag{7}$$

These terms are assumed constant for the duration of a disturbance, their values being those occuring in the initial equilibrium condition.

Equations (7) are non-dimensionalized and the resulting coefficients for use in equations (4) and (6) become

$$k_{X_{\bar{u}}} = k_{F_\lambda}$$

$$k_{X_{\bar{u}}} = \lambda \, k_{F_\lambda}$$

$$k_{X_{\bar{w}}} = k_L + k_{F_\gamma}$$

$$k_{Z_{\bar{u}}} = -\lambda \, k_{L_\lambda}$$

$$k_{Z_{\bar{w}}} = -k_{L_\gamma}$$

$$k_{M_U} = k_{M_\lambda}$$

$$k_{M_U} = \lambda\, k_{M_\lambda}$$

$$k_{M_W} = k_{M_\gamma} \tag{8}$$

where the terms on the right are obtained directly from the wind tunnel data curves. It should be noted that in the wind tunnel data curves, Reference 3, the platform angle of attack α is by definition positive if the platform is tilted forward, i. e., $\gamma = -\alpha$.

The derivatives of the second group are the damping terms, $k_{X_{\dot\theta}}$ and $k_{M_{\dot\theta}}$, and the gyrobar feedback terms, k_{X_δ} and k_{M_δ}. The latter represent the forces and moments, respectively, generated by the control vanes due to the automatic control input δ. In the following paragraph the damping terms $k_{X_{\dot\theta}}$ and $k_{M_{\dot\theta}}$ will be derived.

A pitching velocity $\dot\theta$ about the CG of the aircraft affects the equilibrium of forces and moments due to

a) the change of momentum of the fluid at the duct inlet

b) the Coriolis forces generated by the fluid during its passage through the duct

c) forces caused by changes in the angle of attack of propeller blade elements.

The first two are mass forces, the latter is of an aerodynamic nature.

a) Change of Momentum at Duct Inlet

If v_a denotes the mean axial velocity of the fluid through the duct (assumed to be cylindrical), the mass flow per second amounts to $\rho\pi R^2 v_a$. The change in velocity due to a pitching velocity $\dot\theta$ at the duct inlet is $\dot\theta \ell_1$ (see Sketch 2). The force generated by this momentum change is

$$X_1 = -\rho\pi R^2 v_a \ell_1 \dot\theta \tag{9}$$

As this force acts at the duct inlet, the resulting pitching moment about the CG becomes

$$M_1 = -\rho\pi R^2 v_a \ell_1^2 \dot\theta \tag{10}$$

14
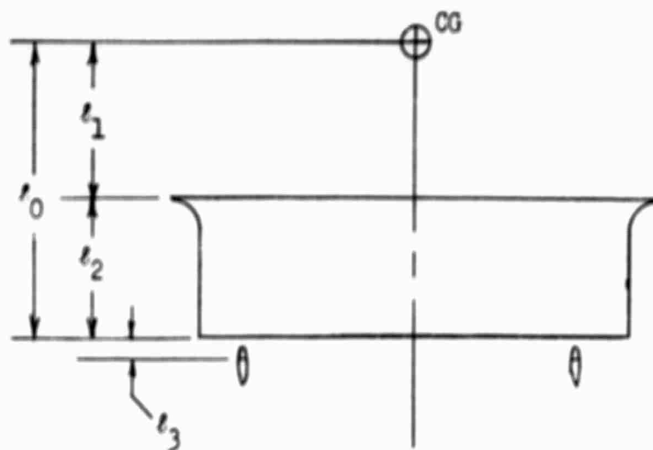
SKETCH 2

b) Coriolis Forces

The elemental Coriolis force exerted by the duct flow on the ring of depth $d\ell$ is given by twice the product of the axial velocity v_a, the pitching velocity $\dot{\theta}$ and the mass dm contained within the ring at any instant, i.e.,

$$dX_2 = -2v_a \dot{\theta} \, dm = -2v_a \dot{\theta} \rho \pi R^2 d\ell$$

Integration over the shroud gives

$$X_2 = -2v_a \dot{\theta} \rho \pi R^2 \int_{\ell_1}^{\ell_0} d\ell = -2v_a \rho \pi R^2 \ell_2 \dot{\theta} \tag{11}$$

The pitching moment generated by the force dX_2 is

$$dM = dX_2 \cdot \ell$$

$$= -2v_a \dot{\theta} \rho \pi R^2 \ell \, d\ell$$

Integration over the shroud length gives

15

$$M_2 = -2v_a \dot{\theta} \rho \pi R^2 \int_{\ell_1}^{\ell_0} \ell \, d\ell$$

$$= -v_a \rho \pi R^2 \dot{\theta} \left(\ell_0^2 - \ell_1^2 \right) \tag{12}$$

c) Aerodynamic Propeller Forces

For the calculation of the aerodynamic forces due to a pitching velocity $\dot{\theta}$, we replace the two contra-rotating propellers by a hypothetical single propeller having the same total number of blades. It is further assumed that the propeller oscillates about an axis which passes through its center, i.e., the translational velocity due to a pitching velocity $\dot{\theta}$ about the CG is neglected. As the ducts used are relatively short, for a first approximation it may be assumed that the propeller blade angle of attack changes are identical with those of an open propeller.

For a blade element dr at a radius r and an azimuth position Ψ the change in angle of attack due to pitching velocity $\dot{\theta}$ is $r\dot{\theta}\cos\Psi/r\Omega$ $= \cos\Psi \cdot (\dot{\theta}/\Omega)$. The resulting elemental pitching moment amounts to

$$dM_3 = -c(\Omega r)^2 r \frac{\rho}{2} a_p \frac{\dot{\theta}}{\Omega} \cos^2\Psi \, dr$$

For a total of b number of blades, integration over radius and azimuth gives

$$M_3 = -\frac{1}{2\pi} bc \frac{\rho}{2} a_p \Omega \dot{\theta} \int_0^{2\pi} \int_0^R \cos^2\Psi \, r^3 \, d\Psi \, dr$$

$$= -\frac{1}{16} bc\rho a_p R^4 \Omega \dot{\theta}$$

$$= -\frac{1}{16} \sigma\rho a_p (\Omega R) \pi R^4 \dot{\theta} \tag{13}$$

Summation of the various components finally leads to the following expressions

$$X_{\dot{\theta}} = -\rho \pi R^2 v_a (\ell_1 + 2\ell_2)$$

$$= -\rho \pi R^2 v_a (\ell_0 + \ell_2)$$

$$M_{\dot{\theta}} = -\left[\rho \pi R^2 v_a \ell_0^2 + \frac{1}{16} \sigma\rho a_p (\Omega R) \pi R^4 \right] \tag{14}$$

16

In non-dimensional form, the above equations simplify to

$$k_{X_\theta} = - \frac{v_a(\ell_0 + \ell_2)}{(\Omega R)^2}$$

$$k_{M_\theta} = - \frac{1}{\Omega R} \left[\frac{v_a \ell_0^2}{(\Omega R)R} + \frac{\sigma a_p R}{16} \right] \tag{15}$$

If the mean axial velocity v_a is not known, its value can be calculated from momentum theory, which states that for hovering flight

$$\text{Thrust} = \rho \pi R^2 v_a^2$$

$$\text{i.e.,} \quad v_a = \sqrt{\frac{W}{\rho \pi R^2}} \tag{16}$$

For forward flight conditions it is convenient to write

$$v_a = \mu V \tag{17}$$

Where μ is a non-dimensional quantity which can again be calculated from momentum theory, (see Ref. 6). From this reference the equation in μ may be written:

$$\mu^4 (1 - f_i + \frac{1}{4} f_i^2 - \sin^2 \gamma) + \mu^2 f_i \sin^2 \gamma = \frac{1}{4} C_L^2$$

$$+ \frac{1}{4} f_i^2 \sin^2 \gamma \tag{18}$$

Thus, with $C_L = \frac{2k_L}{\lambda^2}$ and an internal drag coefficient $f_i = .08$, as suggested in the above reference, the equation becomes

$$\mu^4 (.9216 - \sin^2 \gamma) + \mu^2 (.08 \sin^2 \gamma) - \frac{k_L^2}{\lambda^4} - .0016 \sin^2 \gamma = 0 \tag{19}$$

For small λ, it is found possible to ignore the μ^2 term and, hence, obtain the following approximate equation

17

$$\mu = \left[\frac{k_L^2}{\lambda^4 (\cos^2 \gamma - .0784)} \right]^{1/4} \tag{20}$$

where the values of k_L, γ and λ are obtained from the wind tunnel test data (Ref. 3).

The gyrobar feedback terms, k_{X_δ} and k_{M_δ}, result from the aerodynamic force and moment exerted on the vanes which are actuated by the gyrobar. It should be noted that by definition the vane displacement = $n\delta$, where a positive gyrobar deflection δ generates a positive X-force and a positive pitching moment M.

Thus,

$$k_{X_\delta} = \frac{a_v \Lambda_v (v_a)^2 n}{(\Omega R)^2 \pi R^2}$$

$$k_{M_\delta} = \frac{a_v \Lambda_v (v_a)^2 n(\ell_0 + \ell_3)}{(\Omega R)^2 \pi R^3} = k_{X_\delta} \left[\frac{\ell_0 + \ell_3}{R} \right] \tag{21}$$

Equations (8), (15) and (21) represent all the aerodynamic stability derivatives required for the solution of the equations of motion (eqs. 4 and 6). The physical dimensions and mass properties of the 7-foot platform, also necessary to the solution, will, of course, depend upon the exact configuration chosen for the dynamic analysis. Several configurations will be studied in this report and their selection will be considered in the next section.

18

5. SELECTION OF CONFIGURATIONS

For the present study, configurations exhibiting a combination of small aerodynamic moments in forward flight equilibrium coupled with high efficiencies in both hovering and forward flight are of primary interest. On this basis, a selection of configurations to be analyzed will be made using the wind tunnel data of Reference 3.

Wind tunnel and static tests were conducted on four ducts of 2.0 foot diameter in combination with three different sets of contra-rotating adjustable-pitch propellers. In addition, vanes mounted in the slipstream and centerbodies of the type used in flying platforms were investigated. A more detailed description of the model and components is given in Tables 1 through 6.

The model was tested at advance ratios of 0, 0.05, 0.10 and 0.15 for various tilt angles and propeller blade settings sufficient to cover the maximum efficiency conditions for each configuration. Measurements were made of the total lift, propulsive force, pitching moment and power and the data are presented in the form of coefficients based on propeller tip speed, duct area and propeller radius.

In order to correctly represent the manned 7-foot platform, it was necessary to apply corrections to the data. The vanes and the center-bodies mentioned above were investigated only for one duct and were not tested simultaneously. Therefore, corrections in the force and moment coefficients were made to all configurations for simulation of the pilot and engines of the platform and for the slipstream vanes at zero deflection angle, when applicable. The corrections applied for pilot and engines (without vanes) were

$\lambda = 0$	$\Delta k_L = -.0005$	$\Delta k_F = 0$	$\Delta k_{M_{\ell/4}} = 0$
.05	-.0005	-.00025	.0004
.10	-.0005	-.00075	.0008
.15	-.0005	-.0010	.0006

The corrections for pilot and engines and slipstream vanes at zero deflection angle were

$\lambda = 0$	$\Delta k_L = -.0010$	$\Delta k_F = 0$	$\Delta k_{M_{\ell/4}} = 0$
.05	-.0025	-.00125	.0006
.10	-.0005	-.00275	-.0009
.15	.0015	-.0010	-.0001

A correction was also applied to the data plots of moment versus advance ratio due to the presence of extraneous measured moments at zero advance ratio. These moment curves were reduced by a constant amount equal to the value measured at zero advance ratio. The hovering efficiency, or figure of merit, for the corrected configurations is listed in Table 7 and the corrected equilibrium plots of forward flight efficiency, tilt angle, lift and moment coefficients versus advance ratio are shown in Figures 3 through 18.

After comparing the corrected data, it was decided to investigate the dynamic responses of all four ducts with primary emphasis of study upon the open 'bell-mouth' Duct 3, because it developed the highest efficiencies in hovering and in forward flight. The three-bladed propeller is considered throughout the program, except for one configuration of Duct 3 with a two-bladed propeller. This choice was determined by the questionable reliability of the two-bladed propeller test data and the sparseness of data on the untwisted, constant chord propeller.

Several blade pitch settings have been selected for each configuration, as no single pitch setting is optimum in regard to both efficiencies in hovering and forward flight and aerodynamic moments. In general, maximum efficiency in hovering occurs at a pitch setting of approximately 15 to 18° at 0.7 radius station. Maximum efficiency in forward flight occurs at the lower pitch settings, and minimum moments at higher pitch settings.

The configurations selected for dynamic studies are

1) Duct 3: modified lemniscate or 'bell-mouth' section with 3-bladed propeller at blade pitch settings of 12, 18 and 24°, with and without gyrobar stabilizer. Notation - $D_3 P_3 HB$ and $D_3 P_3 HB\ V_0$

2) Duct 3 with 3-bladed propeller but with twice the normal clearance between propeller tips and inner duct surface (normal clearance = .0038R) at blade pitch settings of 12 and 18°. Notation - $D_3 P_3 HB\ \Delta R$

20

3) Duct 3 with 2-bladed propeller at blade pitch setting of 12°. Notation - D_3P_2HB

4) Duct 1: modified NACA 6421 section with 3-bladed propeller at blade pitch settings of 12 and 18°, and with gyrobar stabilizer at blade pitch setting of 12°. Notation - D_1P_3HB and $D_1P_3HB\ V_0$

5) Duct 2: NACA 0018 section with 3-bladed propeller at blade pitch settings of 12 and 18°. Notation - D_2P_3HB

6) Duct 4: of same section as Duct 1 but with 0.6 chord of Duct 1 with 3-bladed propeller at blade pitch settings of 12 and 18°. Notation - D_4P_3HB

7) Unducted 3-bladed propeller at blade pitch settings of 12 and 18°. Notation - P_3HB

The physical dimensions and mass properties of the 7-foot platform for the above configurations are listed in Table 8. The lift coefficient, tilt angle, and the derivatives k_{L_γ}, k_{L_λ}, $\dfrac{\partial k_{M_{\ell/4}}}{\partial \gamma}$, $\dfrac{\partial k_{M_{\ell/4}}}{\partial \lambda}$, k_{F_γ}, and k_{F_λ} were

obtained from the corrected wind tunnel data for the configurations listed above, at equilibrium conditions ($k_F = 0$) for 3 or 4 advance ratios. It should be noted that the accuracy of the derivatives has suffered from the limited number of test points (3 or 4), the accuracy of the test data ($\pm$ 5 to 10%), the moment correction at zero advance ratio, and the corrections applied for the pilot, engines and vanes.

The moment coefficient data from the wind tunnel tests were transferred to the 25% shroud chord position, so the following relations are necessary to obtain the moment coefficients about the center of gravity of the platform:

$$
k_{M_\lambda} = \left(k_{M_\lambda}\right)_{.25\ell_2} + \left(k_{L_\lambda}\right)_{.25\ell_2} \left[\frac{1}{R}\left(.25\ell_2 + \ell_1\right)\right] \sin\gamma
$$

$$
+ \left(k_{F_\lambda}\right)_{.25\ell_2} \left[\frac{1}{R}\left(.25\ell_2 + \ell_1\right)\right] \cos\gamma \tag{22}
$$

21

$$k_{M_Y} = \left(k_{M_Y}\right)_{.25\ell_2} + \left(k_{L_Y}\right)_{.25\ell_2}\left[\frac{1}{R}\left(.25\ell_2 + \ell_1\right)\right]\sin\gamma$$

$$+ \left(k_L\right)_{.25\ell_2}\left[\frac{1}{R}\left(.25\ell_2 + \ell_1\right)\right]\cos\gamma$$

$$+ \left(k_{P_Y}\right)_{.25\ell_2}\left[\frac{1}{R}\left(.25\ell_2 + \ell_1\right)\right]\cos\gamma \tag{23}$$

We now have all the information necessary to obtain the aerodynamic stability coefficients (Eqs. 8, 15 and 21) and to perform the dynamic stability analysis. Table 9 lists all the configurations selected, the flight conditions, and the corresponding numerical values of the coefficients and inputs for the equations of motion, with a case number assigned to each situation investigated.

It was also decided to study Ducts 1 and 3 in more detail by varying the following mass and aerodynamic parameters from their true values. These variations, as noted in Table 9 are:

   1) $\pm$ 20% in gross weight

   2) $\pm$ 50% in pitching moment of inertia

   3) 15.5% decrease (low CG) and 19.5% increase (high CG) in the height of the center of gravity above the duct lip, corresponding to the practical limits of the height of the pilot stand on the platform

   4) $\pm$ 50% in rotary damping coefficient

   5) $\pm$ 50% in speed stability coefficient

   6) $\pm$ 50% in angle-of-attack stability coefficient

Responses to either a pilot control step input in nose-down moment of 25 ft-lbs or a horizontal gust velocity pulse input of 50 ft/sec for 1 second were obtained on an analog computer for the cases described in Table 9, and the results will be discussed in the next section.

6. DISCUSSION OF RESULTS

The equations of motion of the flying platform were solved at
Electronic Associates Computation Center in Los Angeles on their ex-
panded 16-31R analog computer. An X-Y Plotter, 10 x 15 inch, was used
to record the time history of the pitch angle, and a Six-Channel Brush
Recorder was utilized to record the time histories of θ, $\frac{d\theta}{dt}$, $\bar{u}$, $\frac{d\bar{u}}{dt}$ and δ
in the hovering condition and θ, $\frac{d\theta}{dt}$, $\bar{u}$, $\frac{d\bar{u}}{dt}$, $\bar{w}$, and δ in level forward
flight. The time histories as obtained by the X-Y plotter are presented
in Figures 19 through 74 with the characteristics of the most unstable
mode in the time histories given in Figures 75 through 96. These charac-
teristics include the damping factor (defined as the real part of the root
of the most unstable mode, with the sign changed), period of oscillation,
and percent overshoot. The period cannot be given, of course, if the
motion is aperiodic, and the percent overshoot is not given if the motion
is unstable.

Duct 3, simulating the present full-scale ship, has been studied in
most detail. In the hovering condition (Fig. 75), it is seen that a
definite unstable oscillation exists with small increases in the damping
factor and period at the higher pitch settings. Also shown in this figure
are the increase in damping and period with increase in propeller tip
clearance, and the decrease in damping with the two-bladed propeller. As
the advance ratio increases (Fig. 76), the characteristic motion of Duct 3
soon becomes divergent. The effect of increasing the gross weight, with
constant moment of inertia and center of gravity location, is to decrease
the damping in both hovering and forward flight conditions (Fig. 77). An
increase in moment of inertia causes an increase in period of oscillation
in hovering flight and an increase in damping in hovering and at $\lambda = 0.08$
(Fig. 78); raising the center of gravity location produces an increase in
damping factor and period of oscillation in hovering and a decrease in the
damping factor at $\lambda = 0.08$ (Fig. 79). Figure 80 shows the linear increase
in the damping factor with increasing k_{M_θ}. An increase in the speed

stability derivative causes a decrease in damping and period in hovering
and a slight reduction of the divergence in forward flight; an increase in
the positive angle-of-attack stability derivative, i.e., a decrease in static
stability, decreases the damping factor (Figs. 81 and 82).

The gyrobar stabilizer system (Fig. 1) provides considerable damping in
hovering but will not stabilize the divergent motion in forward flight.
Figures 83, 84 and 85 illustrate the stability characteristics for Duct 3
at pitch settings $\beta = 12$, 18, and 24 degrees, respectively. In general, the
damping increases and the percent overshoot decreases with increasing gyrobar
linkage ratio, the period decreasing slightly before sharply increasing. The
discontinuity in period and in the slope of the damping factor, as seen in

23

Figures 83 and 85 is due to the shifting from one mode of oscillation to another, as determined by the definition of damping factor. Much variation in the stability characteristics is attained with the different propeller pitch settings: the smallest overshoot is attained with $\beta = 12^{\circ}$, the maximum damping is obtained for $\beta = 12^{\circ}$ when $K\Omega = 1.25$ and $n = 1.24$, for $\beta = 18^{\circ}$ when $K\Omega = 2.00$ and $n > 1.5$, for $\beta = 24^{\circ}$ when $K\Omega = 0.75$ and $n = 0.97$. In forward flight, the stability characteristics were studied only for Duct 3 at $\beta = 12^{\circ}$ and $\lambda = 0.08$ since the stabilizer will not overcome the divergent motion. It is seen in Figure 86 that the damping factor increases with either an increase in linkage ratio or a decrease in gyrobar specific damping.

Duct 1, of modified NACA 6421 section, has also been studied in some detail for possible improvement in the platform stability characteristics at the expense of a loss in static lifting efficiency. A comparison of Figures 87 and 88 with Figures 75 and 76 shows that an increase in damping is accomplished with Duct 1 in comparison to Duct 3 in hovering and at low advance ratios for the same propeller pitch setting, while a decrease occurs at the higher advance ratios. It is also seen that the improvement occurs over a large range of λ's as the pitch setting increases. Figures 89 and 90 show the same general effects as for Duct 3 (Figs. 77 and 78), in varying the gross weight and moment of inertia. Raising the center of gravity increases the damping factor both in hovering and at $\lambda = 0.08$ over the practical range of CG travel (see Fig. 91). Variations in the rotary damping, speed stability, and angle-of-attack stability derivatives indicate the same general trends for Duct 1 (Figs. 92, 93 and 94) as for Duct 3 (Figs. 80, 81 and 82), with the exception of the damping factor remaining independent of changes in the speed stability derivative at $\lambda = 0.08$. It should be noted, when comparing Ducts 1 and 3 for the effects of W, I, CG, $k_{M_{\dot{\theta}}}$, $k_{M_{\dot{u}}}$ or $k_{M_{\dot{u}}}$, and $k_{M_{\dot{w}}}$, that the magnitude of the damping factor was smaller and the period larger for Duct 1 in hovering. At $\lambda = 0.08$, however, the magnitude of the damping factor was considerably smaller for Duct 3. The gyrobar stabilizer system, studied only at propeller pitch setting of 12° (Fig. 95), provides similar trends in damping and period as a function of gyrobar linkage ratio and damping factor as was obtained with Duct 3 at a pitch setting of 24° (Fig. 85); the overshoot for the two ducts is approximately the same at $\beta = 12^{\circ}$ (see Figs 83 and 95).

The remaining configurations, Duct 2 of NACA 0018 section, Duct 4 of same section as Duct 1 but with 0.6 of the chord, and the open 3-bladed propeller, have been studied briefly. In the hovering condition, the damping factor and the period of oscillation for these three configurations (see Fig. 87) are increased in comparison to Duct 3 (Fig. 75); the order of damping obtained (maximum damping first) is Duct 4, Duct 2, and the open propeller. These configurations all possess decreased damping (or increased divergence) in comparison to Duct 3 at the higher advance ratios (see Figs. 76, 88 and 96).

In order to get a better feeling for the various modes of motion involved and to understand the effect of speed and the gyrobar stabilizer on these modes, the roots of the frequency equation were calculated for selected cases. The results are summarized in the following table, which shows the various modes of motion of the platform without and with gyrobar. The uncoupled, damped vertical motion in hovering has been omitted. For clarification it is stated that

convergence means a negative real root

divergence means a positive real root

damped oscillation means a conjugate complex root with a negative real part

undamped oscillation means a conjugate complex root with a positive real part

Flight Regime	Configuration	
	without gyrobar	with gyrobar
hovering $\lambda = 0$	1) convergence	damped oscillation
	2) undamped oscillation	damped oscillation
forward flight $\lambda = 0.04$	1) small positive real root indicating onset of divergence (not affected by gyrobar)	
	2) convergence	damped oscillation
	3) undamped oscillation	damped oscillation
forward flight $\lambda = 0.08$	1) critical divergence, not affected by gyrobar	
	2) convergence	damped oscillation
	3) damped oscillation	damped oscillation

From this table, which is considered to be typical, the following conclusions can be drawn. The gyrobar has the tendency to change a convergence to a damped oscillation and is quite effective in stabilizing an unstable oscillatory mode. The reason, of course, is that in an oscillatory mode its

25

output signal lags and that, therefore, the maximum automatic control application occurs, timewise, between the maximum of the perturbation angle Θ and the maximum of the pitching velocity $\dot{\Theta}$. This means that in an oscillatory mode the gyrobar applies both a control input in phase with the attitude and in phase with the rate of change of attitude and fulfills a similar function as a combined attitude and rate gyro. However, the gyrobar is not capable of coping with a divergence. As a matter of fact, in the two divergent cases listed in the table, the addition of the gyrobar to the platform had practically no effect whatsoever on the positive real root of the frequency equation. For this reason, the platform with and without gyrobar, develops at higher speed a very critical divergence which is primarily caused by static instability.

6.1 Graphical Representation of Equilibrium of Pitching Moments

The table in section 6. shows that in the lower speed range investigated (λ from 0 to approximately 0.04) the dominant mode of motion is an oscillation which may be either increasing or decreasing. As any convergences or secondary oscillations (the latter happen to be damped) die out after a certain time, there exists in each of these cases one dominant, oscillatory mode which can be conveniently represented by a vector diagram.

There is a separate vector diagram for each equation of motion involved, where each term in the equation is represented by a vector characterized by its length and phase relationship. All vectors rotate with the same angular velocity, namely the frequency of the oscillatory mode. We restrict ourselves here to the vector presentation of the pitching moment equation, the reason being that the moment derivatives are the quantities which have a major effect on the flight characteristics of the platform. For convenience the Θ vector in these vector diagrams has been plotted horizontally, positive to the right (see Figs. 97, 98 and 100).

These figures refer to the dominant oscillatory modes listed in the table mentioned above. They represent the undamped oscillation of the platform without stabilizer at hovering and $\lambda = 0.04$, respectively, and the damped hovering oscillation of the platform with gyrobar. Figures 97 and 98 refer to an increasing oscillation and Figure 100 to a decreasing oscillation. It may be worthwhile mentioning that in the former case the phase angle between a vector and its derivative is $< 90^{\circ}$, in the latter case this angle is $> 90^{\circ}$ (see also Ref. 7).

These vector diagrams show the dominant roll of the M_u term which, for the platform without gyrobar, is more or less in counterphase with the moment of inertia term. The picture changes if the gyrobar is installed (see Fig. 100). In this case the moment of inertia is in counterphase with the vane moment, and the moment due to the pitch damping is in counterphase with the moment due to the perturbation velocity u.

26

If a divergence occurs, the oscillatory mode loses its significance and the presentation of oscillatory forces and moments in a vector diagram becomes meaningless. Therefore, in Figures 99, 101 and 102 the sign and magnitude of the pitching moment components in a divergence have been plotted. These figures refer to the high speed ($\lambda = 0.08$) divergence of the platform without gyrobar, to the onset of the divergence of the platform with gyrobar at $\lambda = 0.04$ and finally, to the high speed ($\lambda = 0.08$) divergence of the platform with gyrobar. All moments shown in the graphs increase, of course, with time. As the exponential function is the same for all quantities involved, this increase can, as in the vector presentation of the oscillatory modes, be disregarded.

For the high speed flight conditions at $\lambda = 0.08$ (Figs. 99 and 102), more or less all quantities are of the same order of magnitude and there is no dominant term. The picture changes, however, at the onset of the divergence presented in Figure 101. There, the moment of inertia, the pitch damping and the control moment due to automatic vane deflection become less important and the dominant opposing quantities are the aerodynamic pitching moments due to changes in angle of attack and speed.

6.2 Stability Boundaries

In the following section Routh's stability cirteria have been used to show the effect of the principal stability derivatives on the dynamic stability. Stability boundaries as functions of speed stability and static (angle-of-attack) stability are presented in Figures 103 through 105. These figures refer to the configurations previously described. Similar curves showing the effect of static stability and damping in pitch are shown in Figures 106 through 108. In each figure two curves are plotted. The solid lines refer to the platform without gyrobar and the broken lines to the platform with gyrobar stabilizer. Also shown as two distinctive points in each figure are the actual stability derivatives of the present platform, again with and without gyrobar. It should be noted that the difference in the speed stability derivative of these two configurations is caused by the slipstream control vanes which are assumed not to be present in the configuration without gyrobar. These vanes result in a negative contribution to the speed stability derivative k_{M_u} or k_{M_u}, respectively. As this effect of the vanes increases with the flight velocity, it is least pronounced in hovering, Figure 103, where the actual platform configurations have zero attitude stability. The attitude stability derivative k_{M_θ} used in hovering,

Figure 103, is defined as

$$k_{M_\theta} = \frac{\partial M/\partial \theta}{\pi R^2 (\Omega R)^2 \rho}$$

27

where $\partial M/\partial \theta$ is the rate of change of the pitching moment with the platform attitude in pitch. A positive k_{M_θ} value means static instability and vice versa. It should be realized that such an attitude stability cannot be obtained by aerodynamic means but requires some type of attitude gyro. As can be seen from Figure 103, the gyrobar has the tendency to shift the stability boundaries towards attitude instability, i.e., to positive k_{M_θ} values.

With increasing speed, Figures 104 and 105, the actual platform becomes more and more statically unstable and at an advance ratio of $\lambda = 0.08$ both versions (with and without gyrobar) lie in the unstable range. Dynamic stability generally requires a high degree of static stability with the exception of a hypothetical platform equipped with gyrobar which at high advance ratios also has a certain stable range for a small static instability combined with relatively large positive speed stability derivatives, Figure 105.

With regard to the curves in Figures 106 through 108, it can be stated that in all cases a proper combination of attitude or static stability (k_{M_θ}, $k_{M_W} < 0$) and effective pitch damping ($k_{M_\theta} < 0$) results in a stable condition. It appears therefore, that dynamic stability primarily depends on appropriate attitude stability (hovering) or angle-of-attack stability (forward flight) which, unfortunately, is difficult to obtain without "black boxes".

7. CONCLUSIONS

The analysis carried out in this report indicates the effects of possible configuration changes upon the dynamic stability characteristics of the present 7-foot flying platform. The following conclusions are subject to the limitations on the quantity and accuracy of wind tunnel test data available:

1) The stability characteristics of the unstabilized platform with the present duct shape (Duct 3) are undesirable; the motion is described by an unstable oscillation in hovering flight condition, and by divergence in forward flight. While the maximum damping factor occurs at different pitch settings as the advance ratio varies, a pitch setting of roughly 18° appears to give the best overall damping characteristics over the investigated speed range.

2) The gyrobar stabilizer system provides sufficient damping in hovering. In forward flight, the system will not stabilize the divergent motion due to the positive angle-of-attack stability derivative (static instability).

3) Duct 1, of modified NACA 6421 section, was selected for a detailed comparison with Duct 3. While some improvement in damping in hovering and at low advance ratios is noted, the characteristic instability remains and the static lifting efficiency is considerably less.

4) Duct 2, of NACA 0018 section, Duct 4 of same section as Duct 1 but with 0.6 of the chord, and the unshrouded propeller configurations are all accompanied by stability characteristics similar to those of Duct 1.

8. REFERENCES

1. Zimmerman, C. H., Hill, Paul R., and Kennedy, T. T.:

   Preliminary Experimental Investigations of the Flight of a Person Supported by a Jet Thrust Device Attached to His Feet; NACA RM L52D10, dated January, 1953.

2. Sissingh, G. J.:

   Some Remarks On The Control and Stability Characteristics of the Flying Platform (Low Speed Flight Regime); Advanced Research Division of Hiller Aircraft Corporation Report No. ARD-111, dated April 26, 1956.

3. Gill, W. J.:

   Wind Tunnel Tests of Several Ducted Propellers in Non-Axial Flow; Advanced Research Division of Hiller Aircraft Corporation Report No. ARD-224, dated April 20, 1959.

4. Albachten, H. T.:

   Stability Analyses of Flying Platform In Hovering and Forward Flight; Advanced Research Division of Hiller Aircraft Corporation Report No. ARD-112, dated October 12, 1956.

5. Sissingh, G. J.:

   The Frequency Response of the Ordinary Rotor Blade, The Hiller Servo Blade, and the Young-Bell Stabilizer; Royal Aeronautical Establishment Report No. Aero 2367, dated May, 1950.

6. Greenman, R. Newman, R., and Sissingh, G. J.:

   Flying Crane Transportation Systems--Ducted Propeller Technical Study; Advanced Research Division of Hiller Aircraft Corporation Report No. ARD-124, dated December, 1956.

7. Sissingh, G. J.:

   Investigations on Automatic Stabilization of the Helicopter, Part I; Royal Aeronautical Establishment Report No. Aero 2277, dated July, 1948.

TABLE 1

DUCT 1 ORDINATES AND ORIENTATION
MODIFIED NACA 6421 SECTION

Chord Line

Y_O

4° (Ref.)

Y_I

X

0

Parallel to
Propeller Axis

24.00 Dia. (Ref.)

6.00
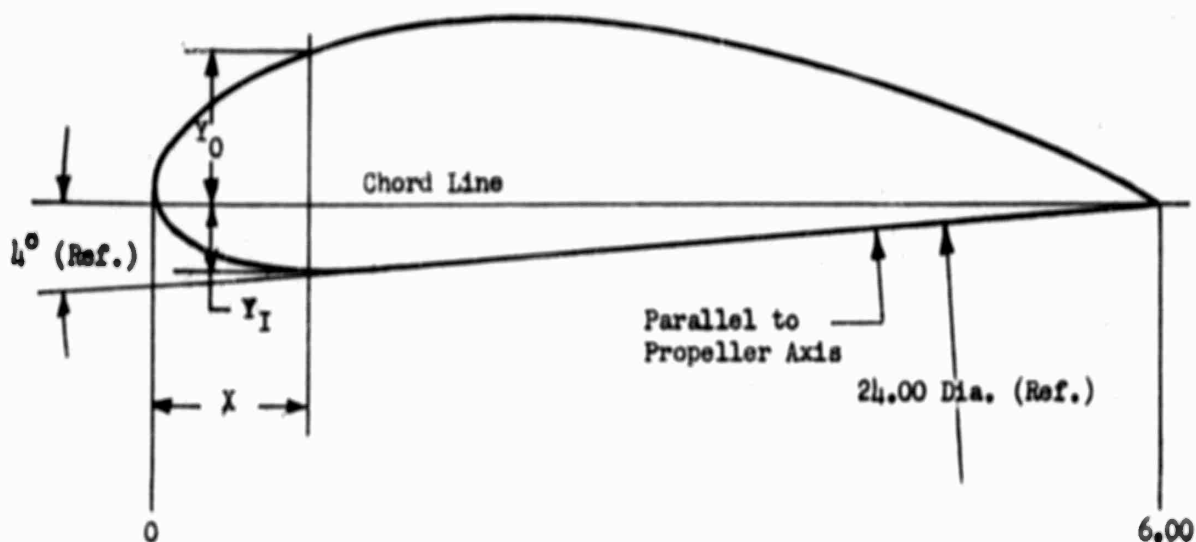
TABLE OF ORDINATES

L.E. Radius = .291
Slope of Radius Thru
End of Chord = 3/10

CHORD	OUTER ORDINATE	INNER ORDINATE
X (in.)	Y_O (in.)	Y_I (in.)
0		0
.075	.308	-.125
.15	.396	-.182
.30	.518	-.250
.45	.615	-.289
.60	.692	-.311
.90	.806	-.331
1.20	.886	-.329
1.50	.938	-.314
1.80	.970	
2.40	.970	
3.00	.910	
3.60	.806	
4.20	.664	
4.80	.485	
5.40	.272	
5.70	.148	
6.00		0

Straight Line
Between these Points

TABLE 2

DUCT 2 ORDINATES AND ORIENTATION
NACA 0018 SECTION
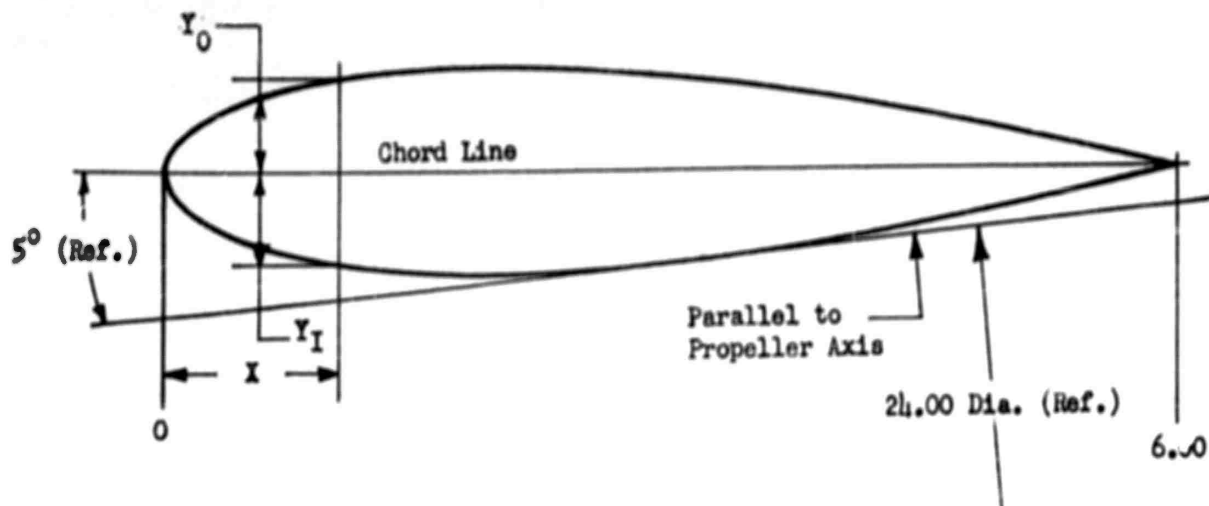
TABLE OF ORDINATES

L.E. Radius = .214

CHORD X (in.)	OUTER ORDINATE Y_O (in.)	INNER ORDINATE Y_I (in.)
0	0	0
.075	.170	-.170
.15	.237	-.237
.30	.320	-.320
.45	.378	-.378
.60	.422	-.422
.90	.481	-.481
1.20	.516	-.516
1.50	.535	-.535
1.80	.540	-.540
2.40	.523	-.523
3.00	.477	-.477
3.60	.411	-.411
4.20	.330	-.330
4.80	.236	-.236
5.40	.132	-.132
5.70	.073	-.073
6.00	0	0

TABLE 3

DUCT 3 ORDINATES AND ORIENTATION
MODIFIED LEMNISCATE CURVE

TABLE OF ORDINATES

θ DEGREES	r INCHES
0	3.39
3	3.38
6	3.36
10	3.27
15	3.16
20	2.99
25	2.72
30	2.40
33	2.16
36	1.89
38	1.67
40	1.41
41	1.27
42	1.10
43	0.90
43.5	0.78
44	0.63
44.5	0.45
44.75	0.31
45	0

The radii between θ of 0° and 10°
modified by an arc of a circle whose
radius is 0.50 as shown above.

TABLE 4

DUCT 4 ORDINATES AND ORIENTATION
MODIFIED NACA 6421 SECTION
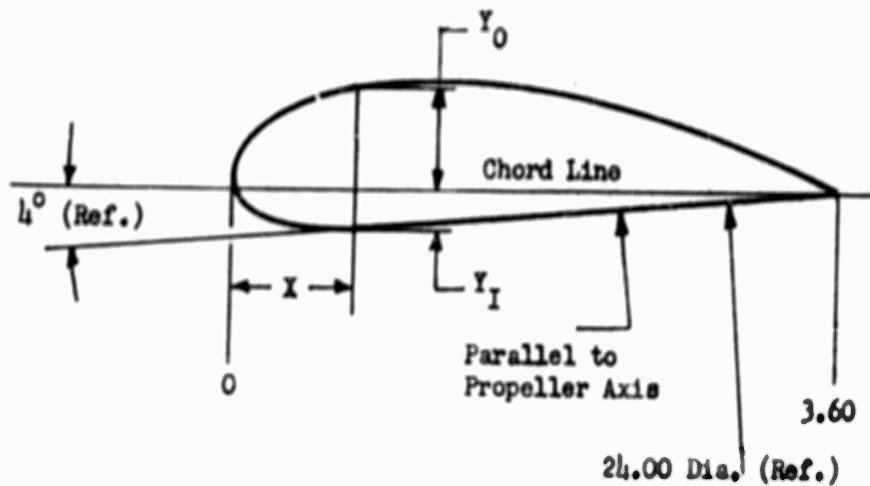
TABLE OF ORDINATES

L.E. Radius = .175
Slope of Radius Thru
End of Chord = 3/10

CHORD X (in.)	OUTER ORDINATE Y_0 (in.)	INNER ORDINATE Y_I (in.)
0		0
.045	.185	-.075
.090	.238	-.109
.180	.311	-.150
.270	.369	-.173
.360	.415	-.186
.540	.484	-.199
.720	.532	-.198
.900	.563	-.188
1.080	.581	
1.437	.582	
1.800	.545	
2.156	.484	
2.520	.398	
2.875	.291	
3.240	.162	
3.420	.089	
3.600		0

Straight Line Between these Points

TABLE 5

PHYSICAL CHARACTERISTICS OF MODEL

DUCT	1	2	3	4
Minimum Inside Radius, ft.	1.00	1.00	1.00	1.00
Minimum Inside Area, sq. ft.	3.14	3.14	3.14	3.14
Chord Length, ft.	.50	.50	.50	.30
Airfoil Section	NACA 6421 (Mod.)	NACA 0018	Lemniscate (Mod.)	NACA 6421 (Mod.)
Propeller Position, in.	5.13*	5.13*	2.59; 4.08; 5.13*	3.08*
Propeller Tip Clearance, in.	.040	.037 Fore Prop. .076 Aft Prop.	.046; .088	.039

*Normal location of rear propeller reference line (see Table 6) from duct leading edge.

EXIT VANE

Number of vanes	2
Chord, ft.	.20
Span, ft.	1.29
Total Area, sq. ft.	.52
Airfoil Section	Symmetrical 15% Thickness Ratio

4

TABLE 5 (cont.)

PHYSICAL CHARACTERISTICS OF MODEL

CENTERBODY

Diameter, ft.

Electric Motor Housing and Dummy	.43
Transmission	.40
Hubs and Spinner	.33

Total Length for Basic Model, ft.	2.83
Total Length with Dummy of Electric Motor Housing, ft.	4.66
Dummy Engines	(See Figure 3C)

PROPELLERS (Contra-Rotating)

No. of Blades/Propeller	2 Twisted	3 Twisted	3 Untwisted
Section	RAF-6	RAF-6	RAF-6
t/c at .7R	.12	.12	.12
$c_{.7R}$, in.	1.11	1.11	1.46
Taper ($c_{1.0R}$ to $c_{.2R}$)	.55	.55	.55
Maximum Radius, ft.	.998	.998	.998
Solidity	.118	.177	.232
Blade Pitch Angle, deg.	Variable	Variable	Variable
Distance between Propeller Planes, in.	1.50	1.50	1.50

TABLE 6

PROPELLER BLADE CHARACTERISTICS

PLAN VIEW

SIDE VIEW
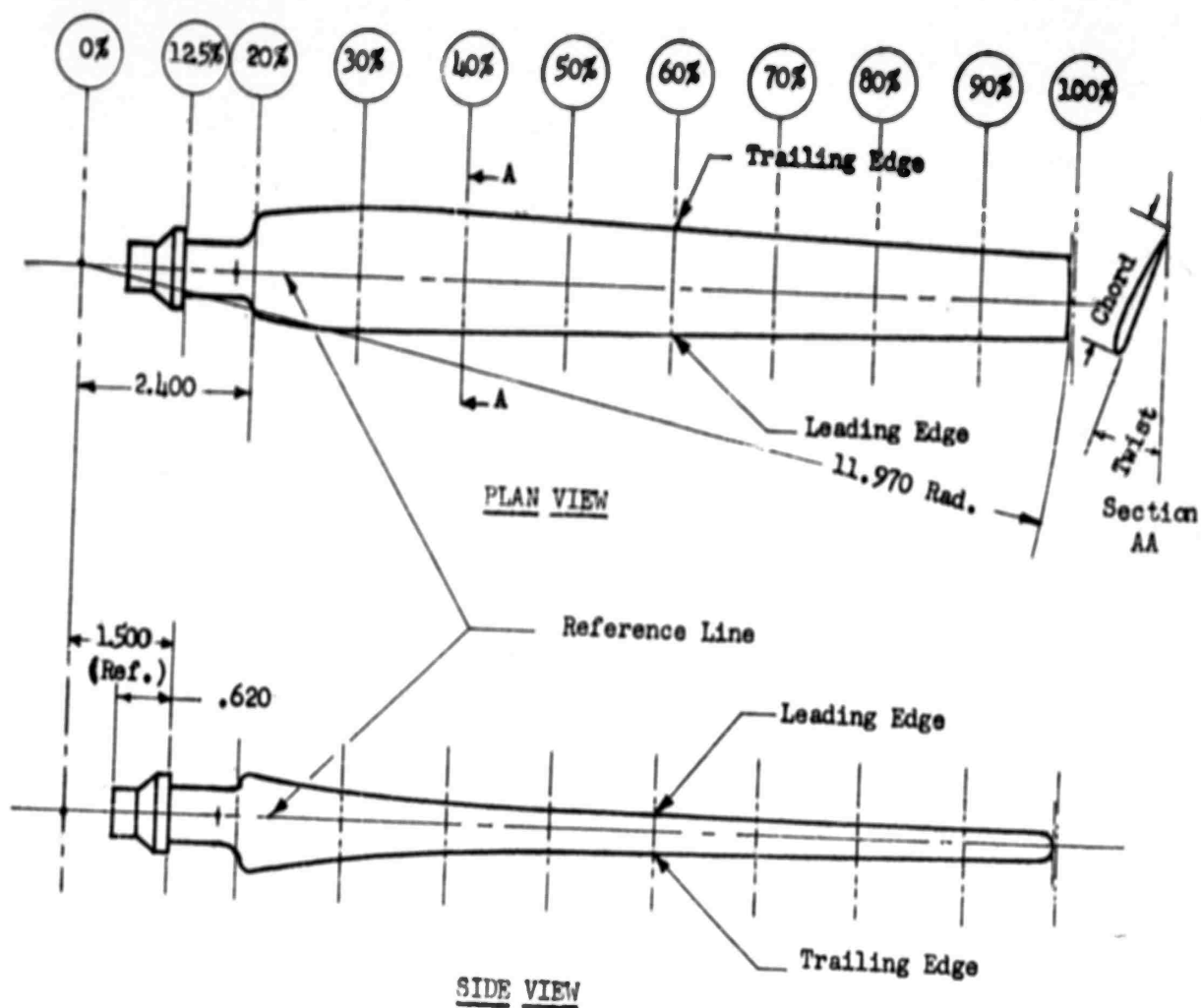
Blade sections from 20% station to 100% station inclusive are RAF-6 airfoils of 12% thickness ratio.

Blade Station, %R	20	30	40	50	60	70	80	90	100
Blade Chord, in.	1.54	1.46	1.37	1.29	1.20	1.11	1.03	.94	.86
Blade Twist, deg.	42.50	28.30	21.20	17.00	14.18	12.13	10.61	9.45	8.50

Untwisted, constant chord blade fabricated using the blade chord and twist at the 30 percent radius station of the twisted blade.

TABLE 7

HOVERING EFFICIENCIES

Configuration	β°	Figure of Merit, $\frac{W}{P}\sqrt{\frac{W}{2\rho\pi R^2}}$
D_3P_3HB	12	0.96
	18	1.03
	24	1.05
$D_3P_3HB\ V_O$	12	0.93
	18	1.00
	24	1.02
$D_3P_3HB\ \Delta R$	12	1.00
	18	0.98
D_3P_2HB	12	0.95
	18	0.88
D_1P_3HB	12	0.65
	18	0.71
$D_1P_3HB\ V_O$	12	0.62
	18	0.68
D_2P_3HB	12	0.65
	18	0.75
D_4P_3HB	12	0.64
	18	0.63
P_3HB	12	0.66
	18	0.62

TABLE 8

PHYSICAL CHARACTERISTICS OF 7-FOOT PLATFORM

a_p = 5.16 per rad

a_v = 4.3 per rad

A_v = 3.19 ft^2

g = 32.2 ft/sec^2

I = 177 $slug-ft^2$ for D_1, D_2, D_3, D_4 and 146 $slug-ft^2$ for P_3S

ℓ_0 = 3.03 ft

ℓ_1 = 1.28 ft for D_1, D_2, D_3 and 1.98 ft for D_4

ℓ_2 = 1.75 ft for D_1, D_2, D_3 and 1.05 ft for D_4

ℓ_3 = 0.25 ft

R = 3.50 ft

W = 565 lbs for D_1, D_2, D_3, D_4 and 509 lbs for P_3S, open propeller

(Pilot weight is 180 lbs for all configurations)

σ = 0.177 for P_3, 0.129 for P_2

EXPLANATIONS TO TABLE 9

1) a and b are the coefficients of the $\dot{\theta}$ and $\ddot{\theta}$ terms in the gyrobar equation of motion and are either both equal to 1 or both equal to 0, indicating presence or absence of the gyrobar stabilizer.

2) I_1 and I_2 are the respective inputs to the first and second equations of equation groups (4) and (6), I_3 is the input to the third equation of equations (6). The input to the gyrobar equation is 0 in all cases. The letter g after the magnitude of I denotes a rectangular pulse input beginning at $t = 0$ and ending at $t = 1$; while, in the absence of g, a step input is denoted.

3) The notes refer to the variations in the following mass and aerodynamic parameters from their true values.

   1.) $\pm$ 20% in gross weight

   2.) $\pm$ 50% in pitching moment of inertia

   3.) 15.5% decrease (low CG) and 19.5% increase (high CG) in the height of the center of gravity above the duct lip, corresponding to the practical limits of the height of the pilot stand on the platform.

   4.) $\pm$ 50% in rotary damping coefficient

   5.) $\pm$ 50% in speed stability coefficient

   6.) $\pm$ 50% in angle of attack stability coefficient

TABLE 9

COEFFICIENTS AND INPUTS USED IN EQUATIONS OF MOTION
PART A - HOVERING FLIGHT

CASE NO.	CONFIG.	p	g	X_{δ_0}	τ	...	...	...	...	...	...	...	...	...	...	NOTES

TABLE 9 (cont.)

COEFFICIENTS AND INPUTS USED IN EQUATIONS OF MOTION
PART A — HOVERING FLIGHT

TABLE 9 (cont.)

COEFFICIENTS AND INPUTS USED IN EQUATIONS OF MOTION
PART A - HOVERING FLIGHT

TABLE 9 (cont.)

COEFFICIENTS AND INPUTS USED IN EQUATIONS OF MOTION

PART B – FORWARD FLIGHT

TABLE 9 (cont.)

COEFFICIENTS AND INPUTS USED IN EQUATIONS OF MOTION

PART B - FORWARD FLIGHT

COEFFICIENTS AND INPUTS USED IN EQUATIONS OF MOTION
PART R - FORWARD FLIGHT

TABLE 9 (cont.)

FWD

ROTATION

LOWER PROPELLER

GYRO BAR

GYRO BAR

ROLL VANE

PITCH VANE

(A)

FWD

(B)

FIGURE 1: GYROBAR STABILIZER

FIGURE 2: SEVEN FOOT PLATFORM WITH RAISED CG CONFIGURATION
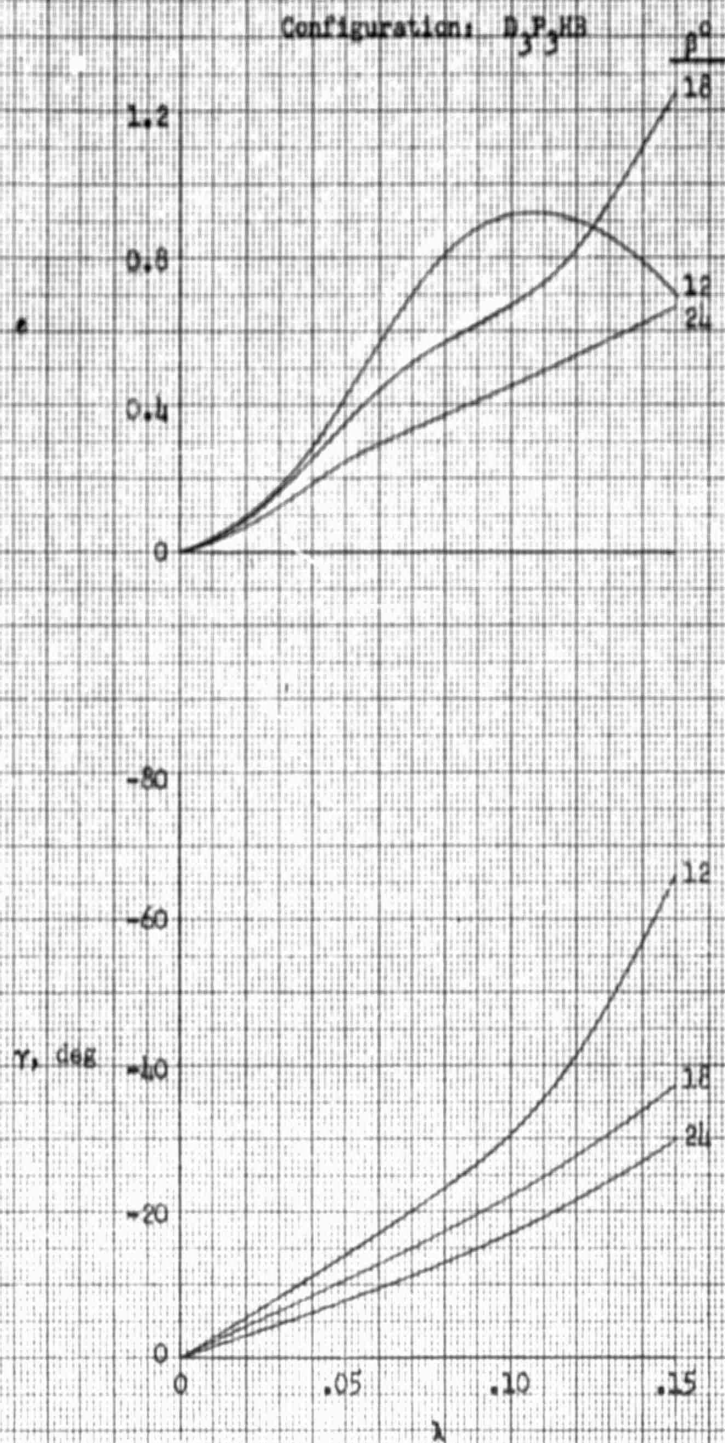
FIGURE 3: FORWARD FLIGHT EFFICIENCY AND EQUILIBRIUM TILT ANGLE VS ADVANCE RATIO
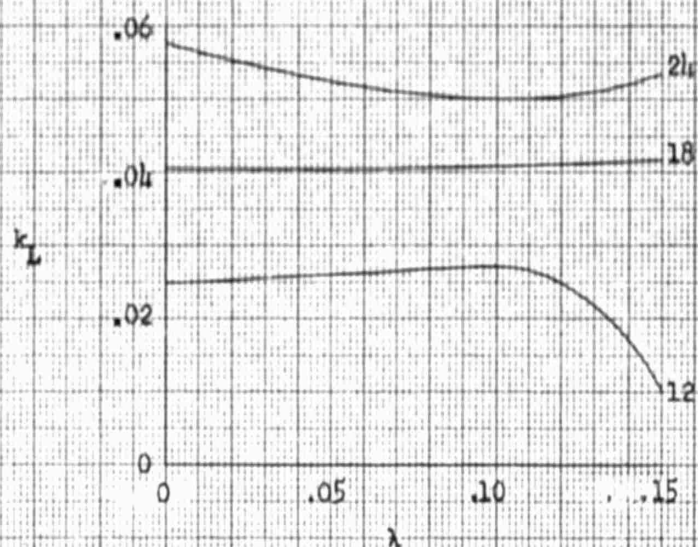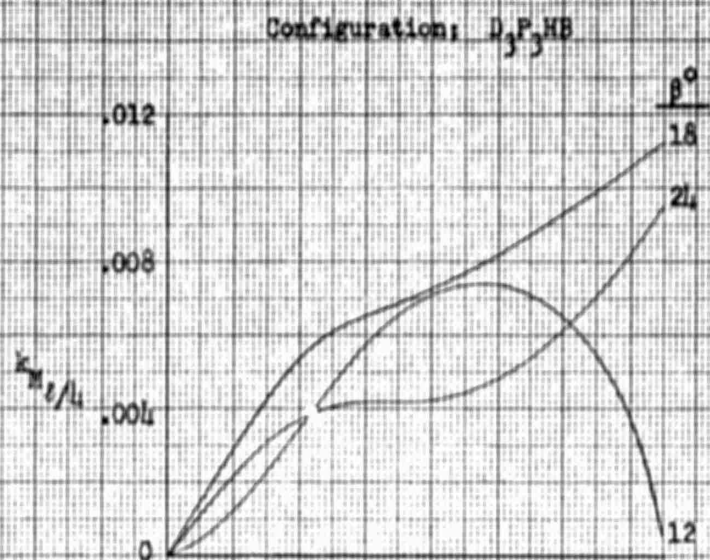
FIGURE 4: EQUILIBRIUM LIFT AND MOMENT COEFFICIENTS VS ADVANCE RATIO

FIGURE 5: FORWARD FLIGHT EFFICIENCY AND EQUILIBRIUM TILT ANGLE VS ADVANCE RATIO
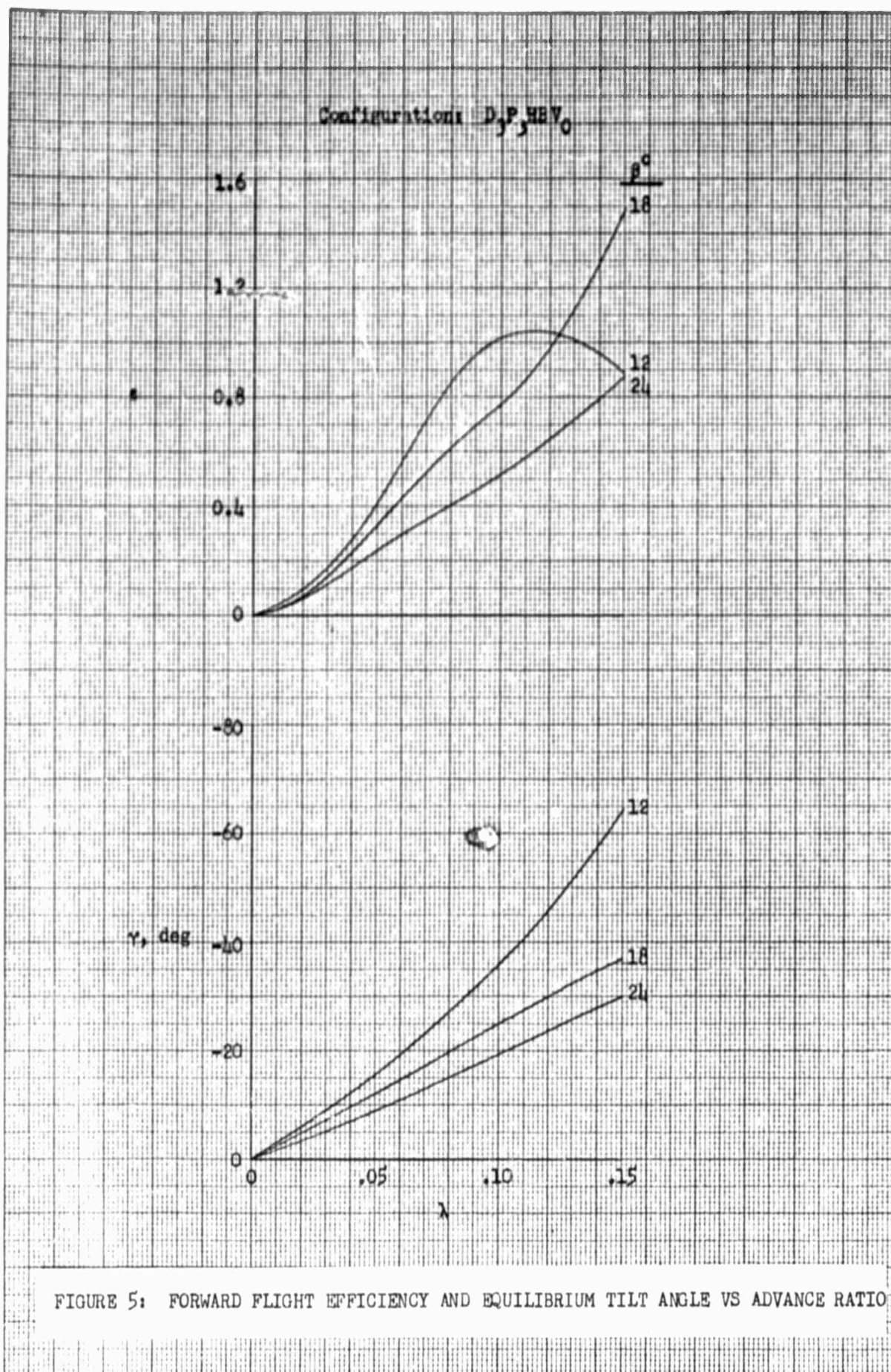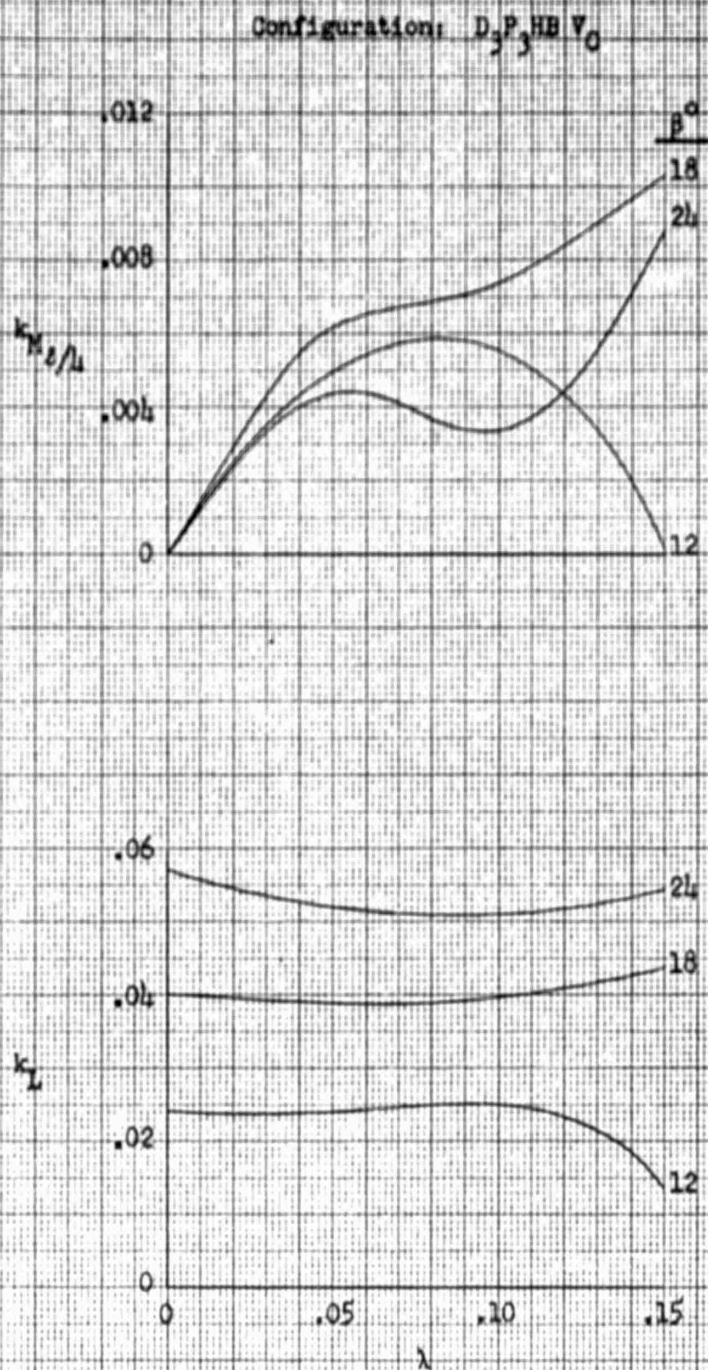
FIGURE 6: EQUILIBRIUM LIFT AND MOMENT COEFFICIENTS VS ADVANCE RATIO

FIGURE 7: FORWARD FLIGHT EFFICIENCY AND EQUILIBRIUM TILT ANGLE VS ADVANCE RATIO

FIGURE 8: EQUILIBRIUM LIFT AND MOMENT COEFFICIENTS VS ADVANCE RATIO

FIGURE 9: FORWARD FLIGHT EFFICIENCY AND EQUILIBRIUM TILT ANGLE VS ADVANCE RATIO

FIGURE 10: EQUILIBRIUM LIFT AND MOMENT COEFFICIENTS VS ADVANCE RATIO

FIGURE 11:   FORWARD FLIGHT EFFICIENCY AND EQUILIBRIUM TILT ANGLE VS ADVANCE RATIO

Configuration: D_1P_3HB
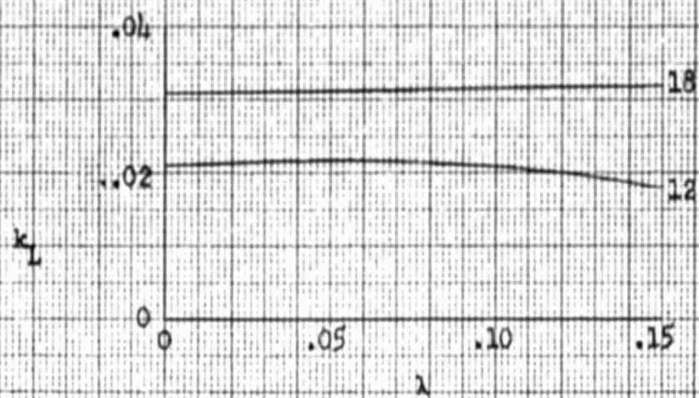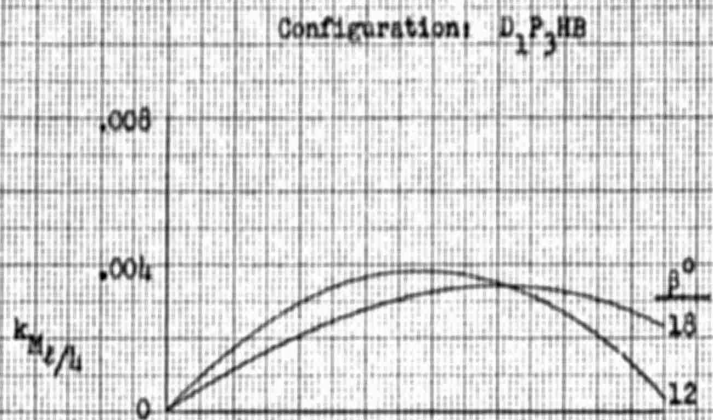
FIGURE 12: EQUILIBRIUM LIFT AND MOMENT COEFFICIENTS VS ADVANCE RATIO
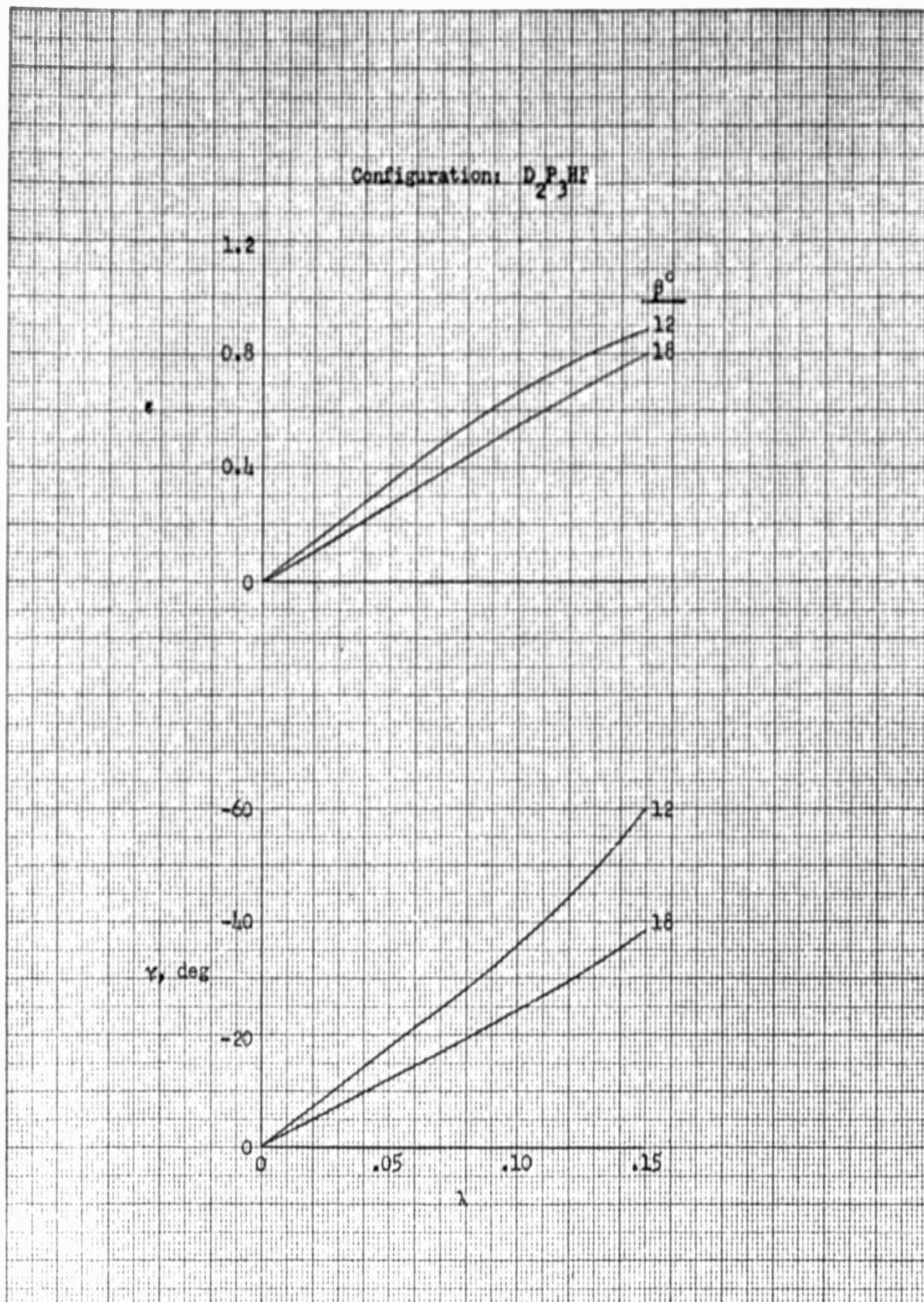
FIGURE 13: FORWARD FLIGHT EFFICIENCY AND EQUILIBRIUM TILT ANGLE VS ADVANCE RATIO
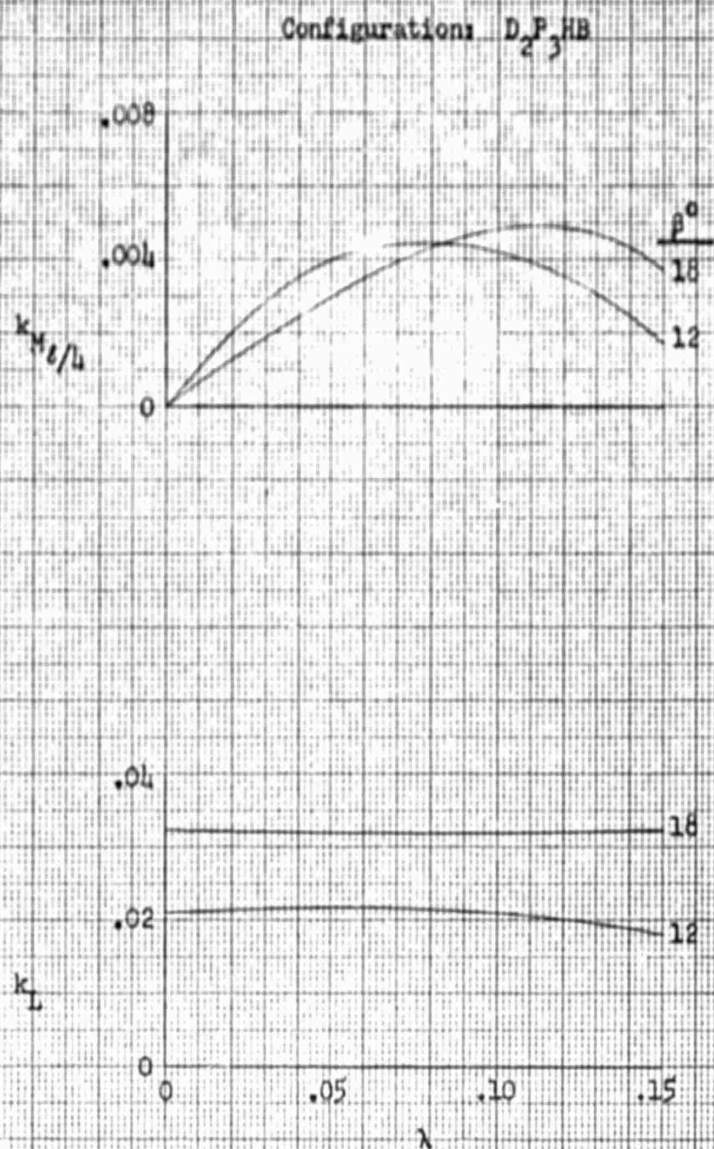
FIGURE 14: EQUILIBRIUM LIFT AND MOMENT COEFFICIENTS VS ADVANCE RATIO

FIGURE 15: FORWARD FLIGHT EFFICIENCY AND EQUILIBRIUM TILT ANGLE VS ADVANCE RATIO

FIGURE 16: EQUILIBRIUM LIFT AND MOMENT COEFFICIENTS VS ADVANCE RATIO
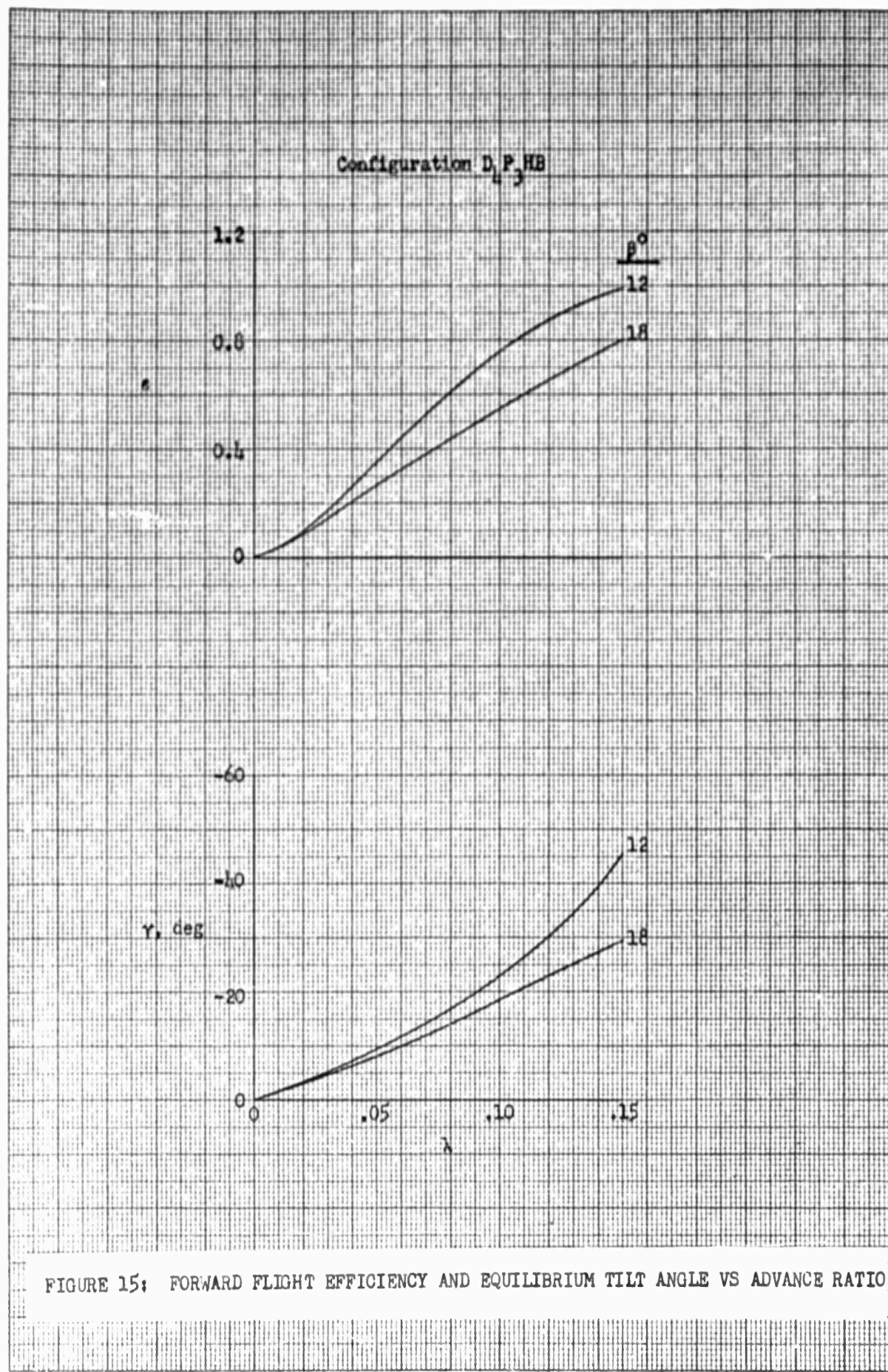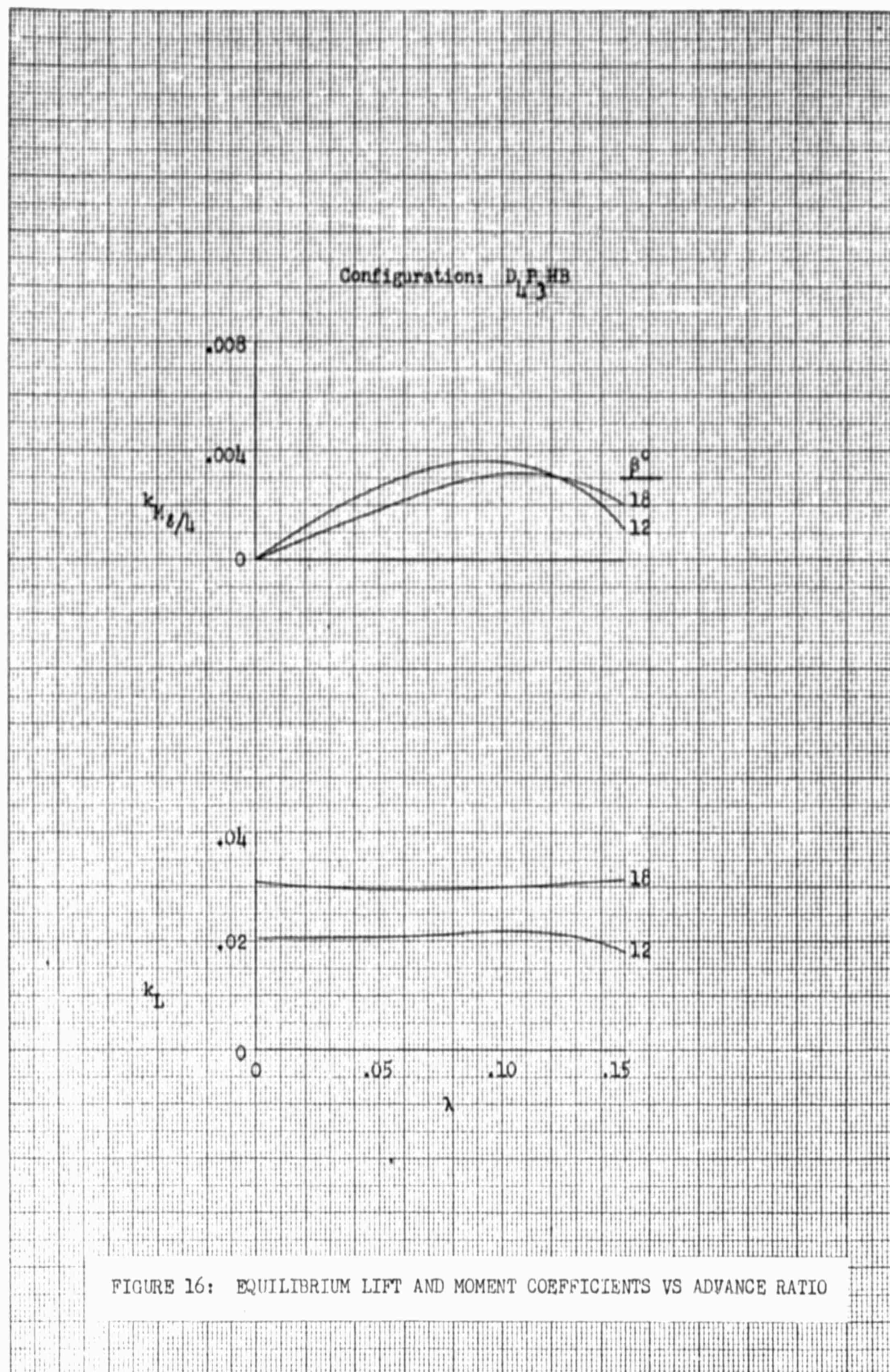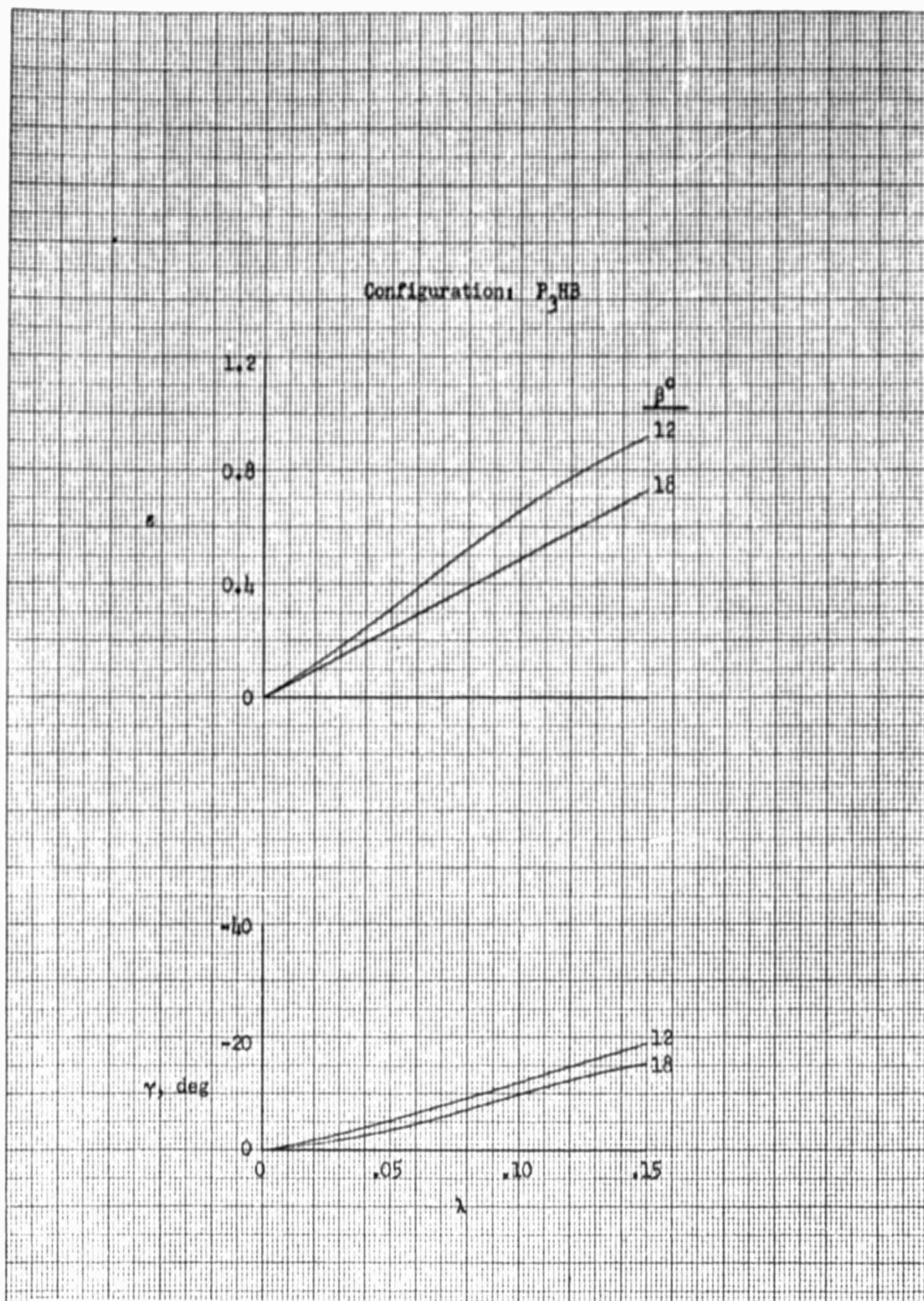
FIGURE 17: FORWARD FLIGHT EFFICIENCY AND EQUILIBRIUM TILT ANGLE VS ADVANCE RATIO
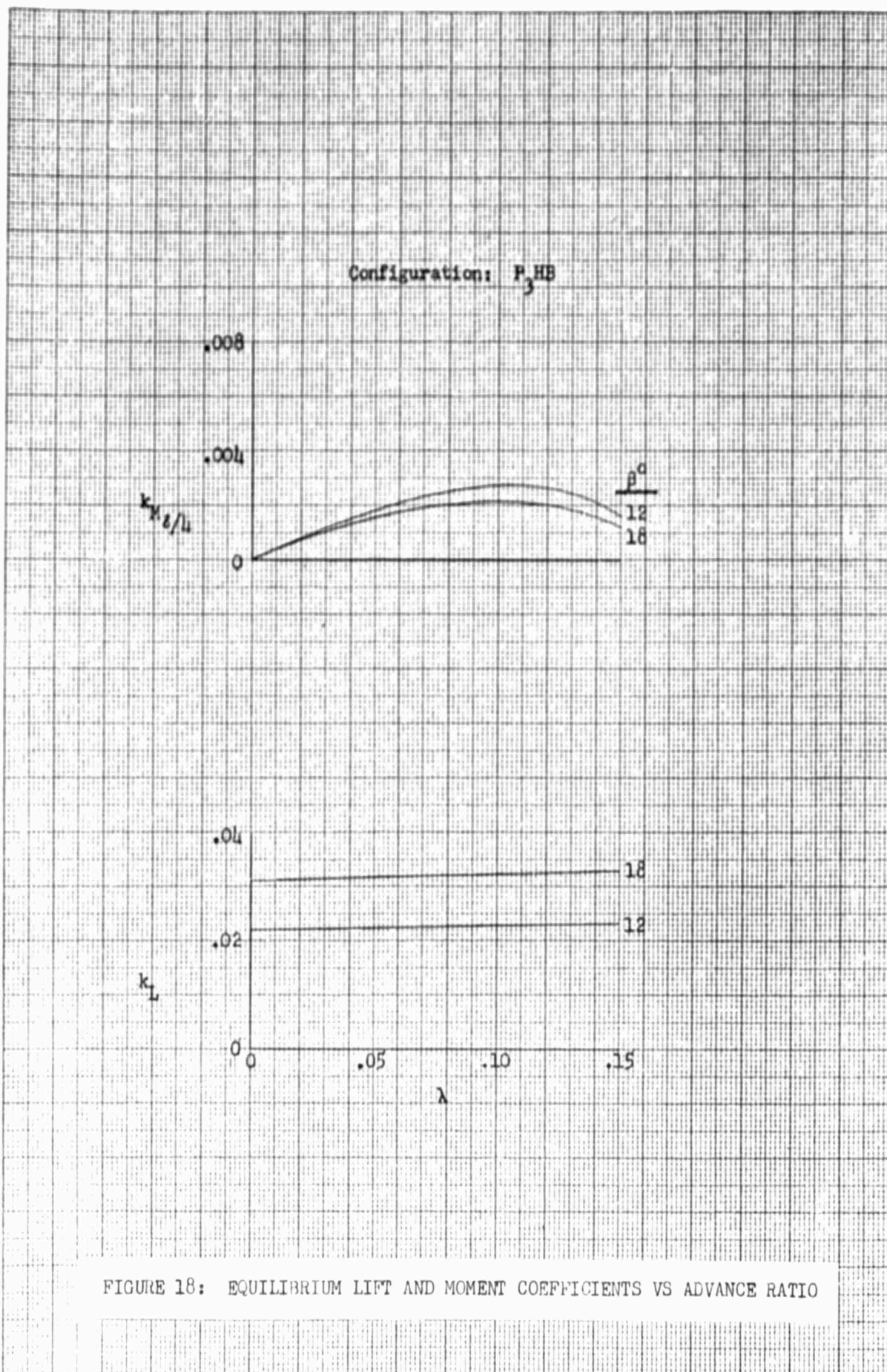
FIGURE 18: EQUILIBRIUM LIFT AND MOMENT COEFFICIENTS VS ADVANCE RATIO

FIGURES 19 TO 74

These figures are copies of the original time histories of pitch
angle for the cases listed in Table 9, obtained with the 16-31R Analog
Computer and X-Y Plotter. It should be noted that the letters X and R
after a case number denote, respectively, an incorrect solution and a
rerun solution. Extraneous curves and marks, due to plotter operation,
should be ignored.
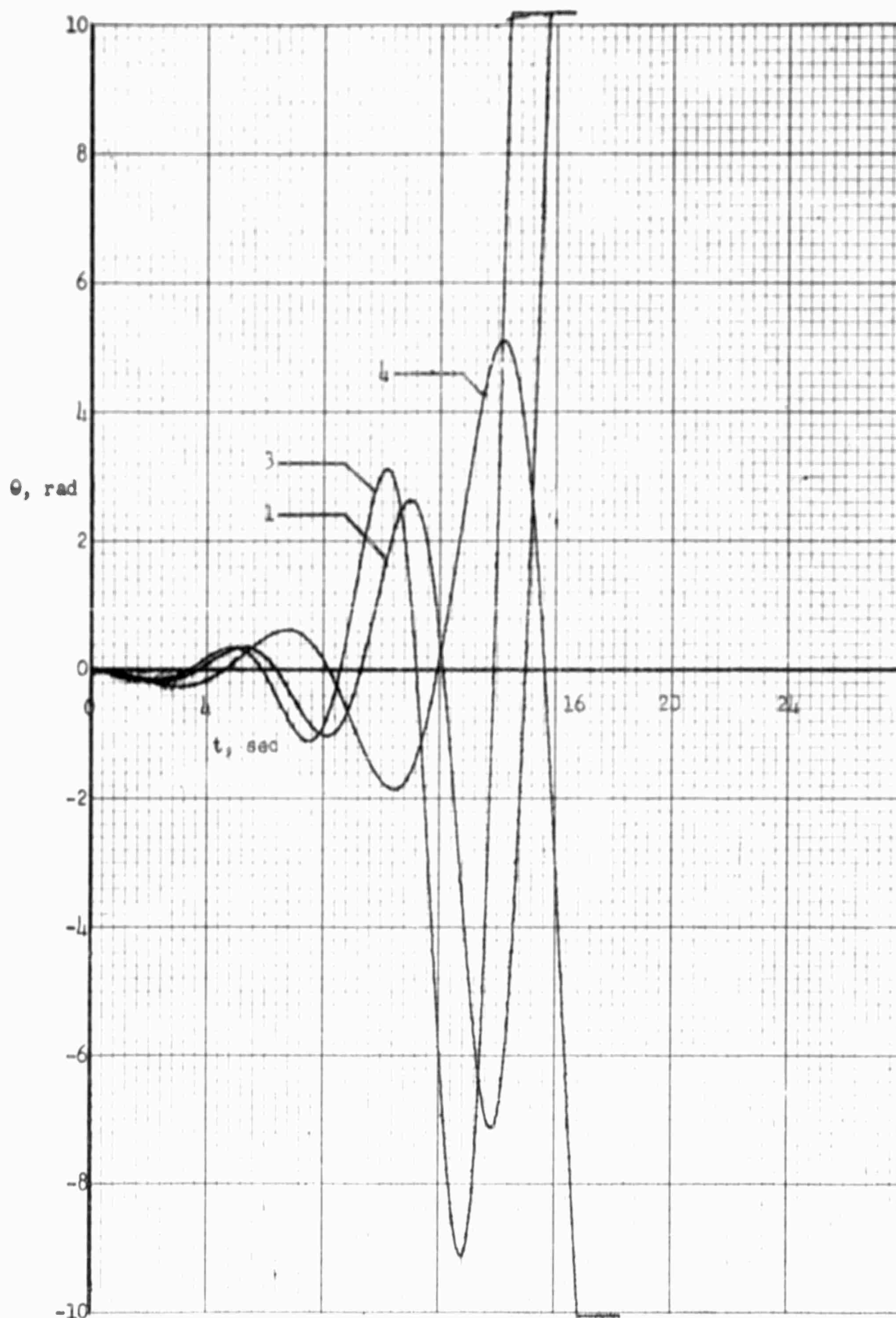
FIGURE 19: PITCH ANGLE RESPONSE TO CONTROL MOMENT STEP INPUT
FOR CASE NOS. 1, 3, 4
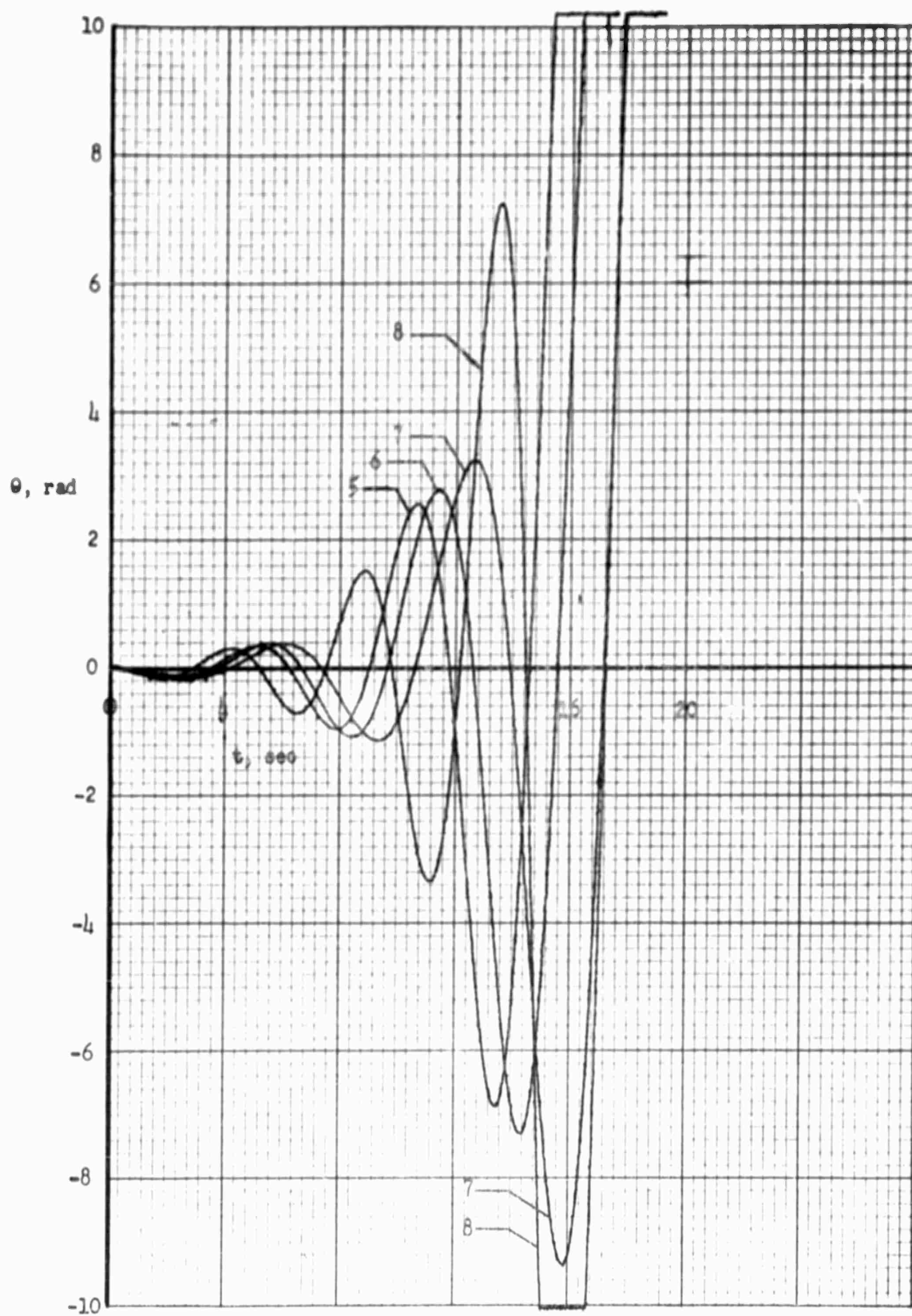
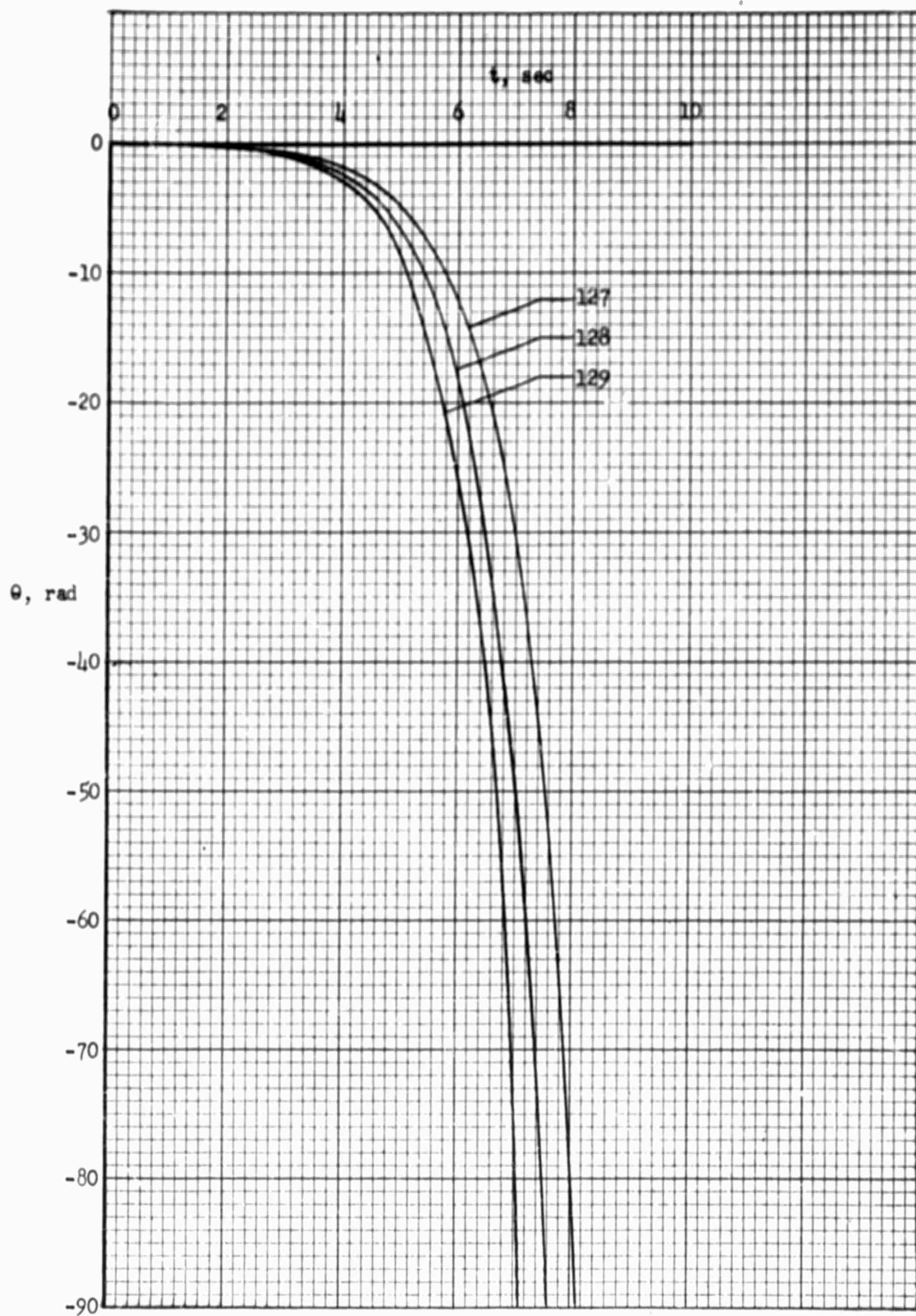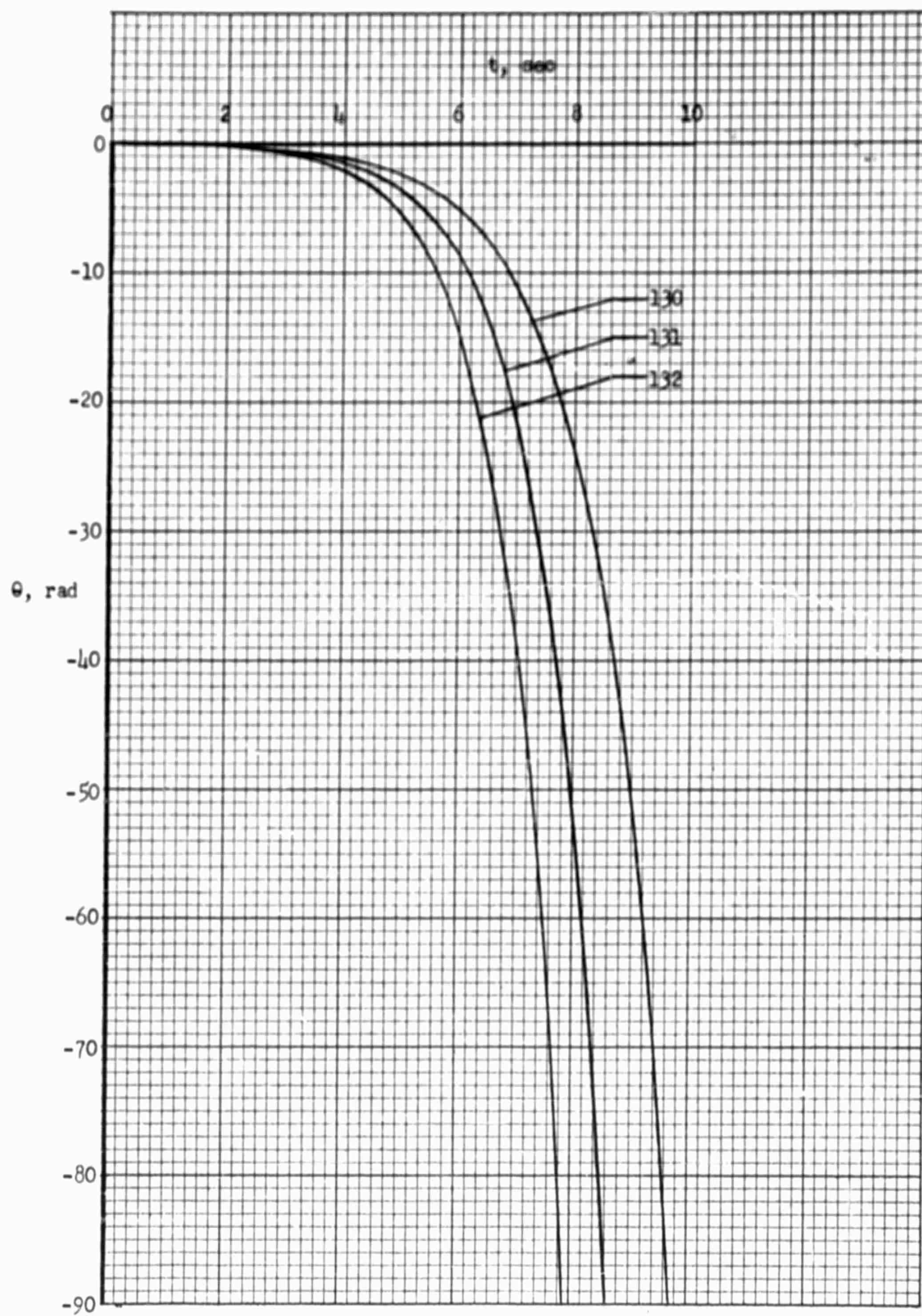FIGURE 20: PITCH ANGLE RESPONSE TO CONTROL MOMENT STEP INPUT
FOR CASE NOS. 5, 6, 7, 8
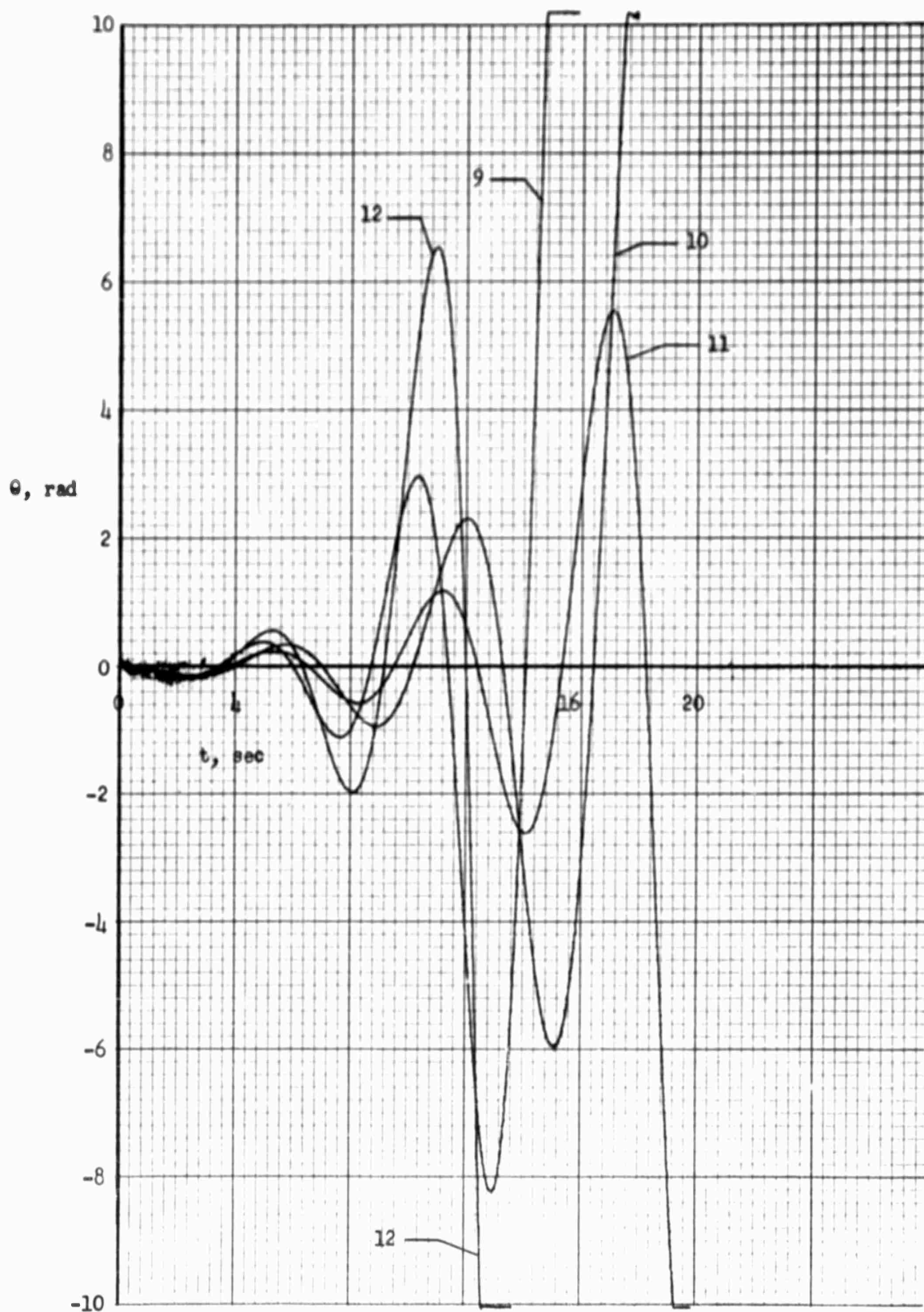
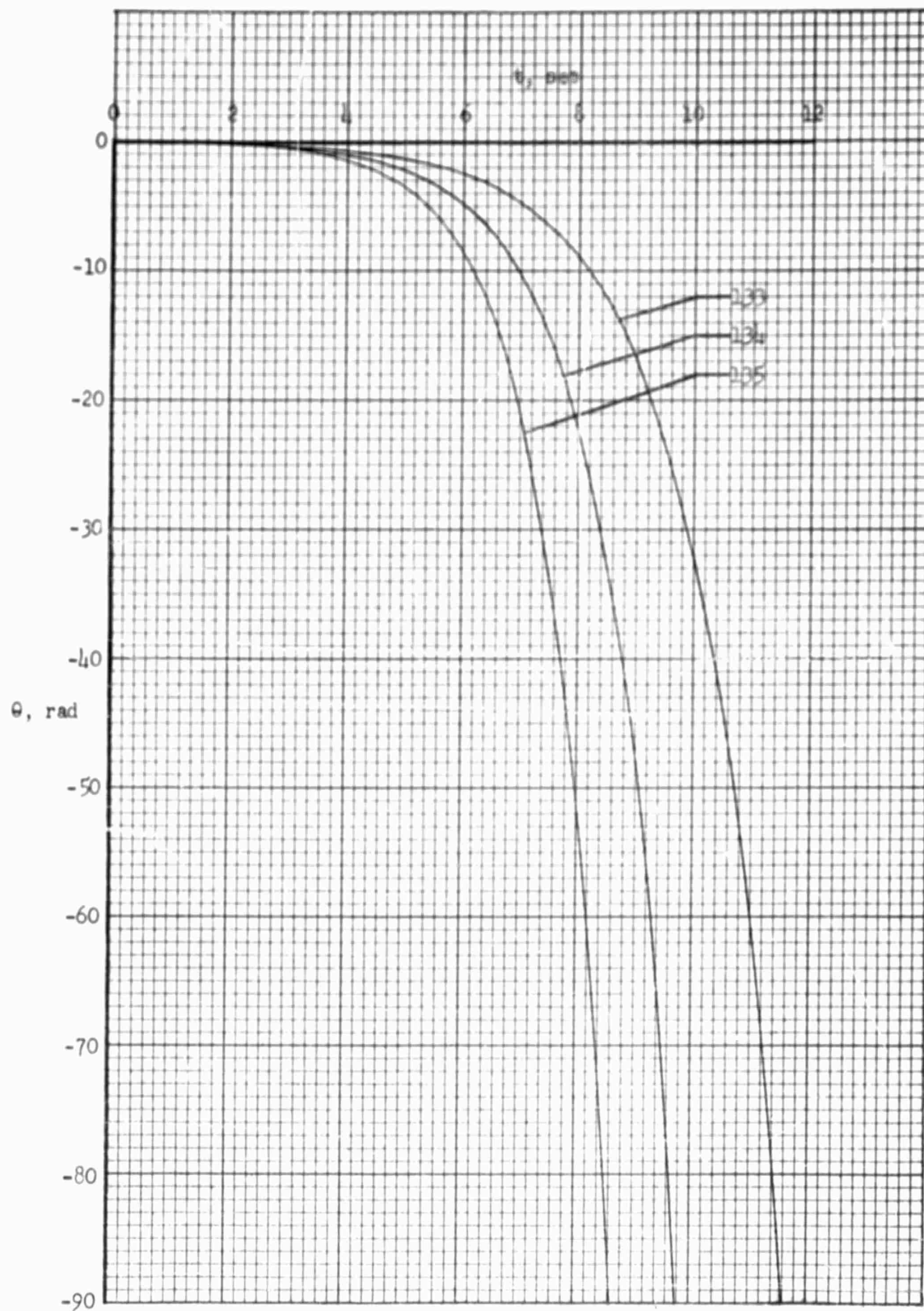FIGURE 21: PITCH ANGLE RESPONSE TO CONTROL MOMENT STEP INPUT FOR CASE NOS. 9, 10, 11, 12
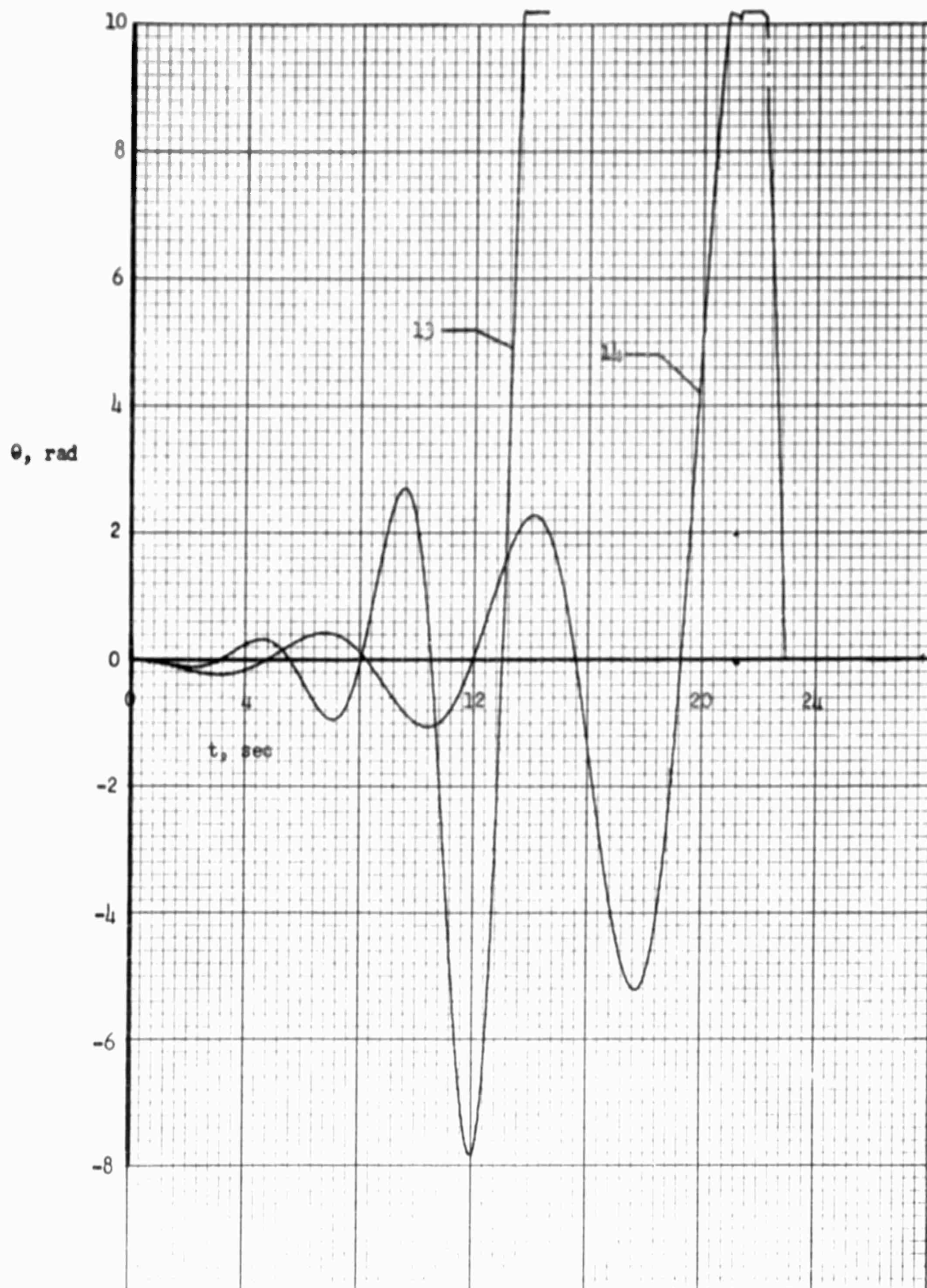
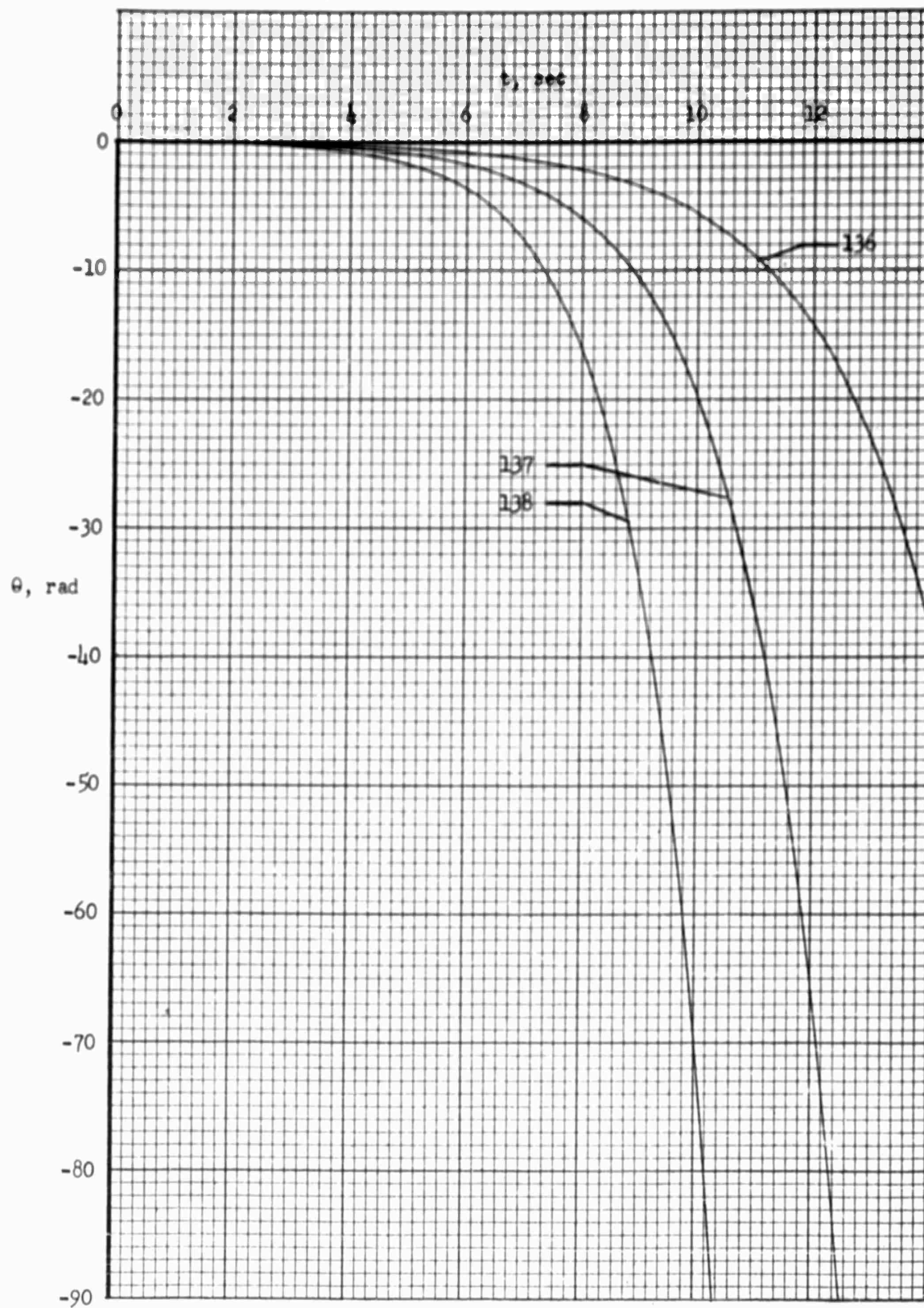FIGURE 22: PITCH ANGLE RESPONSE TO CONTROL MOMENT STEP INPUT
FOR CASE NOS. 13, 14
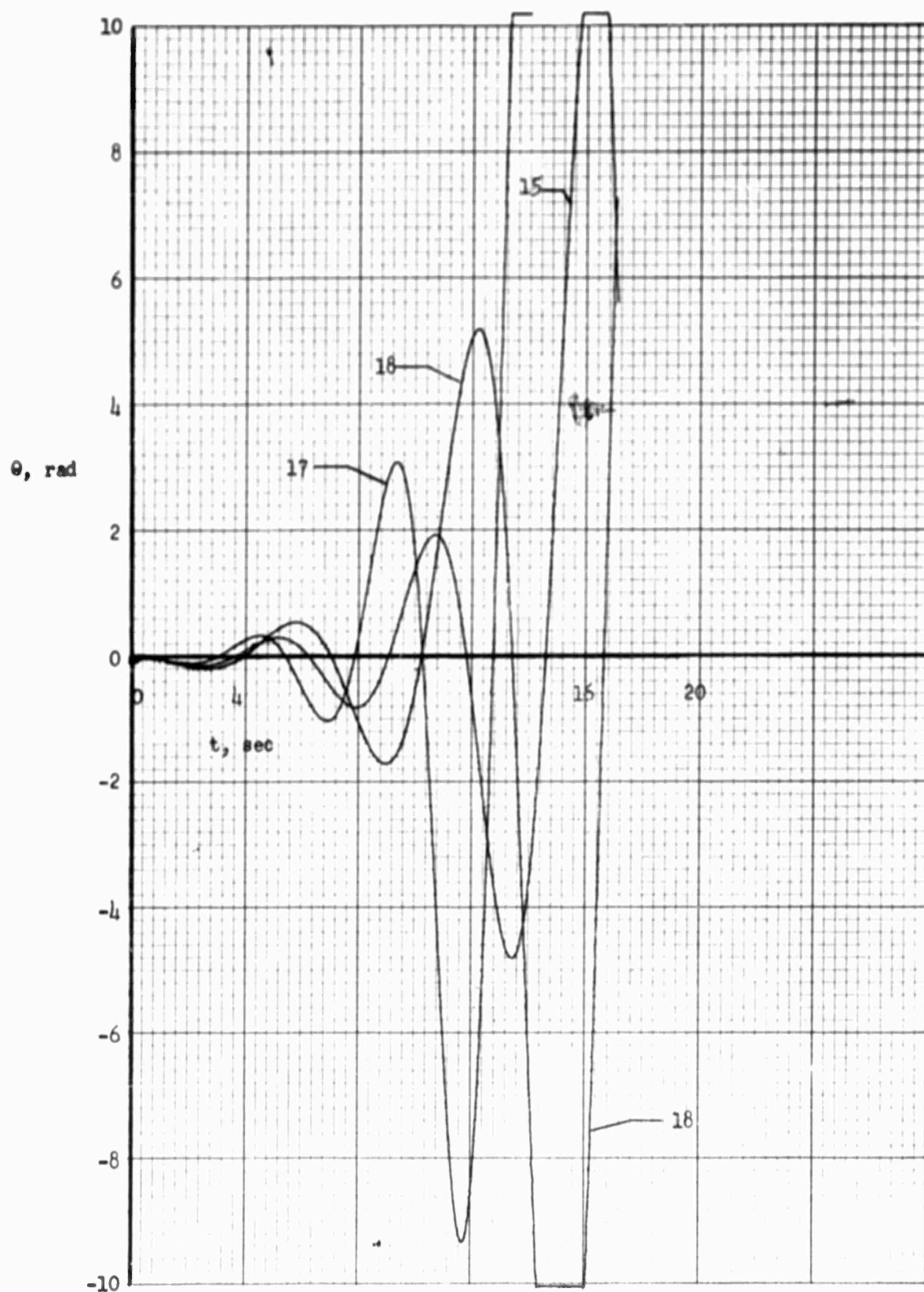
FIGURE 23: PITCH ANGLE RESPONSE TO CONTROL MOMENT STEP INPUT
FOR CASE NOS. 15, 17, 18
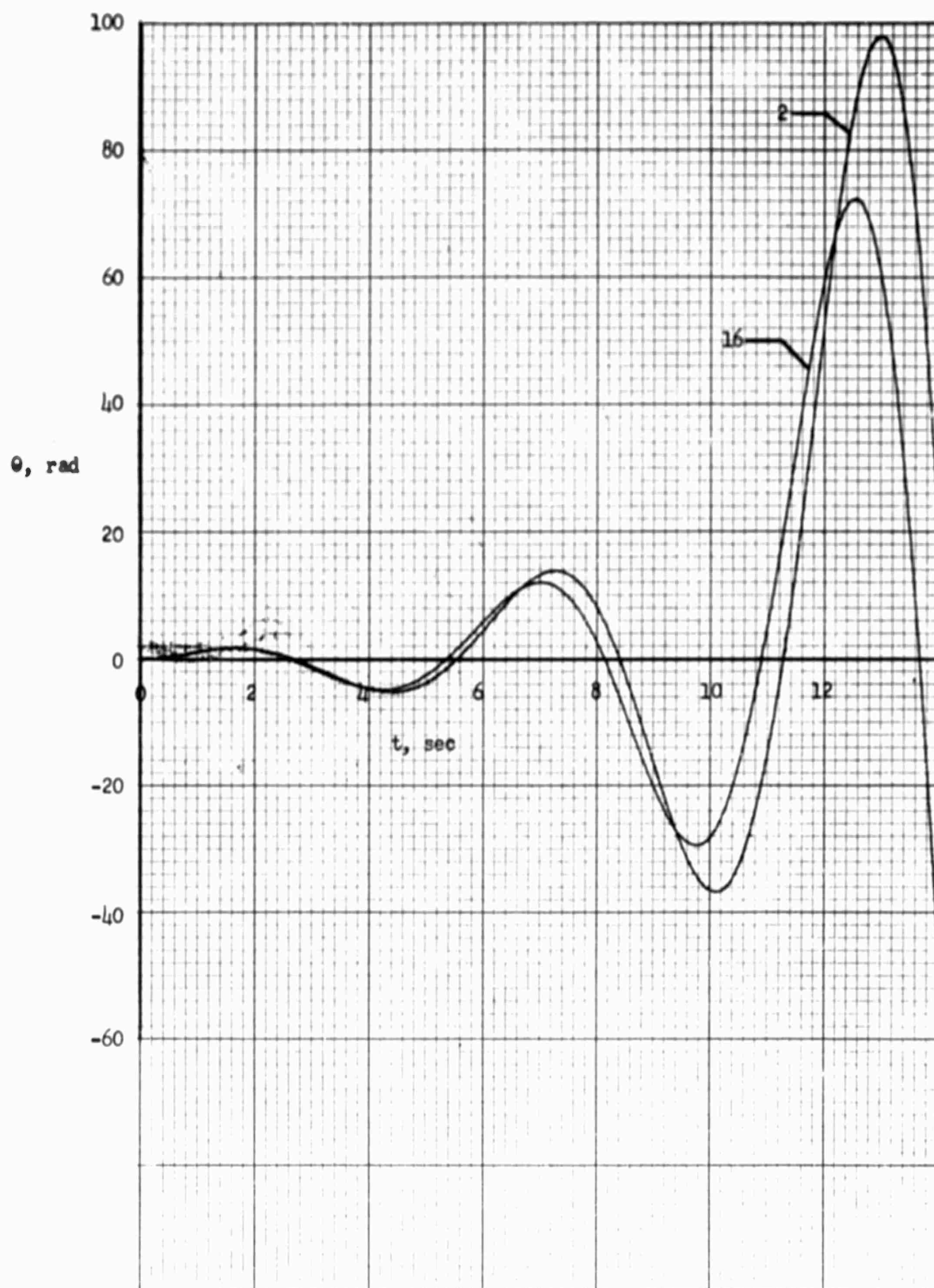
FIGURE 24: PITCH ANGLE RESPONSE TO HORISONTAL GUST PULSE INPUT
FOR CASE NOS. 2, 16
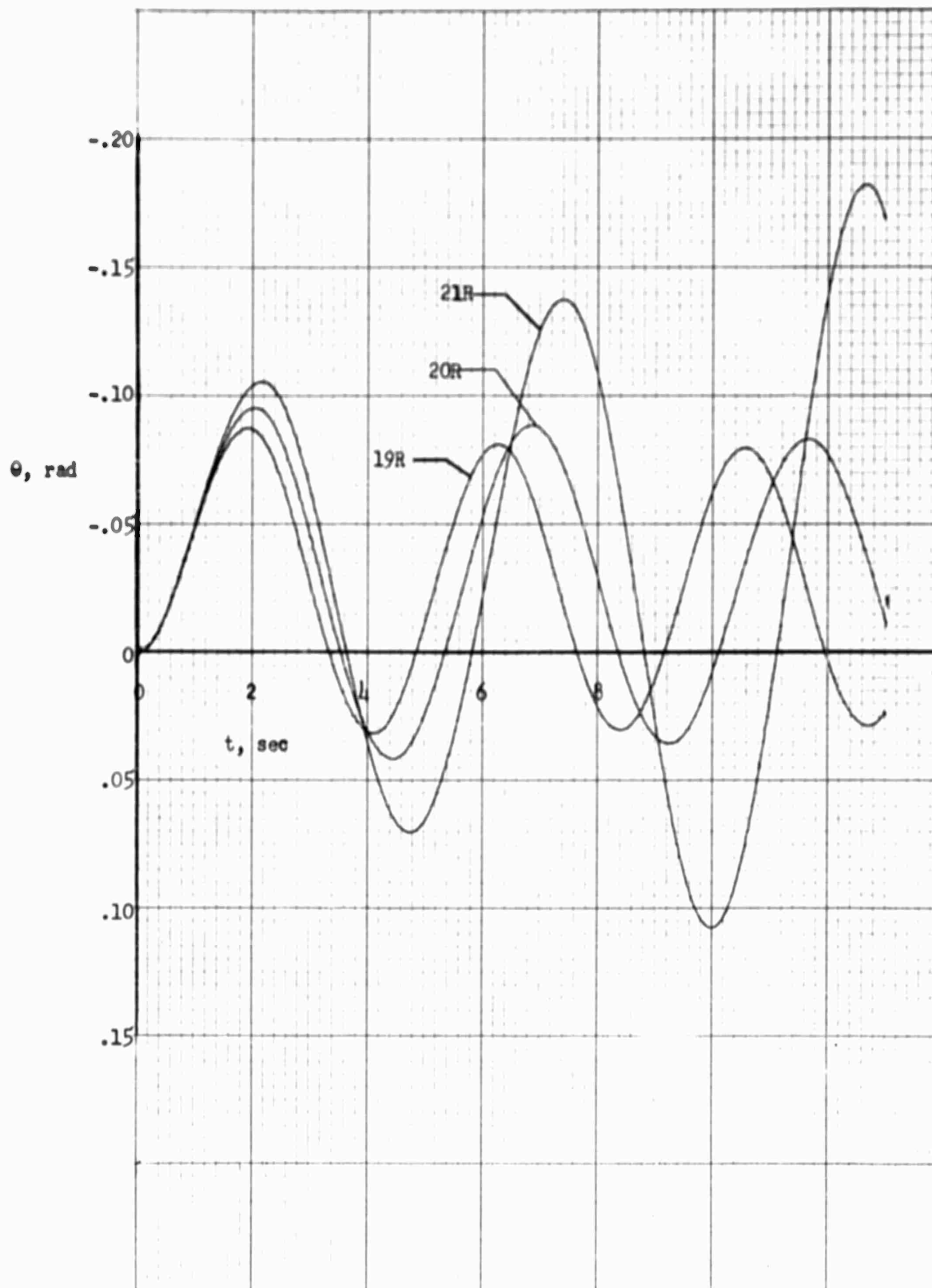
FIGURE 25: PITCH ANGLE RESPONSE TO CONTROL MOMENT STEP INPUT
FOR CASE NOS. 19R, 20R, 21R
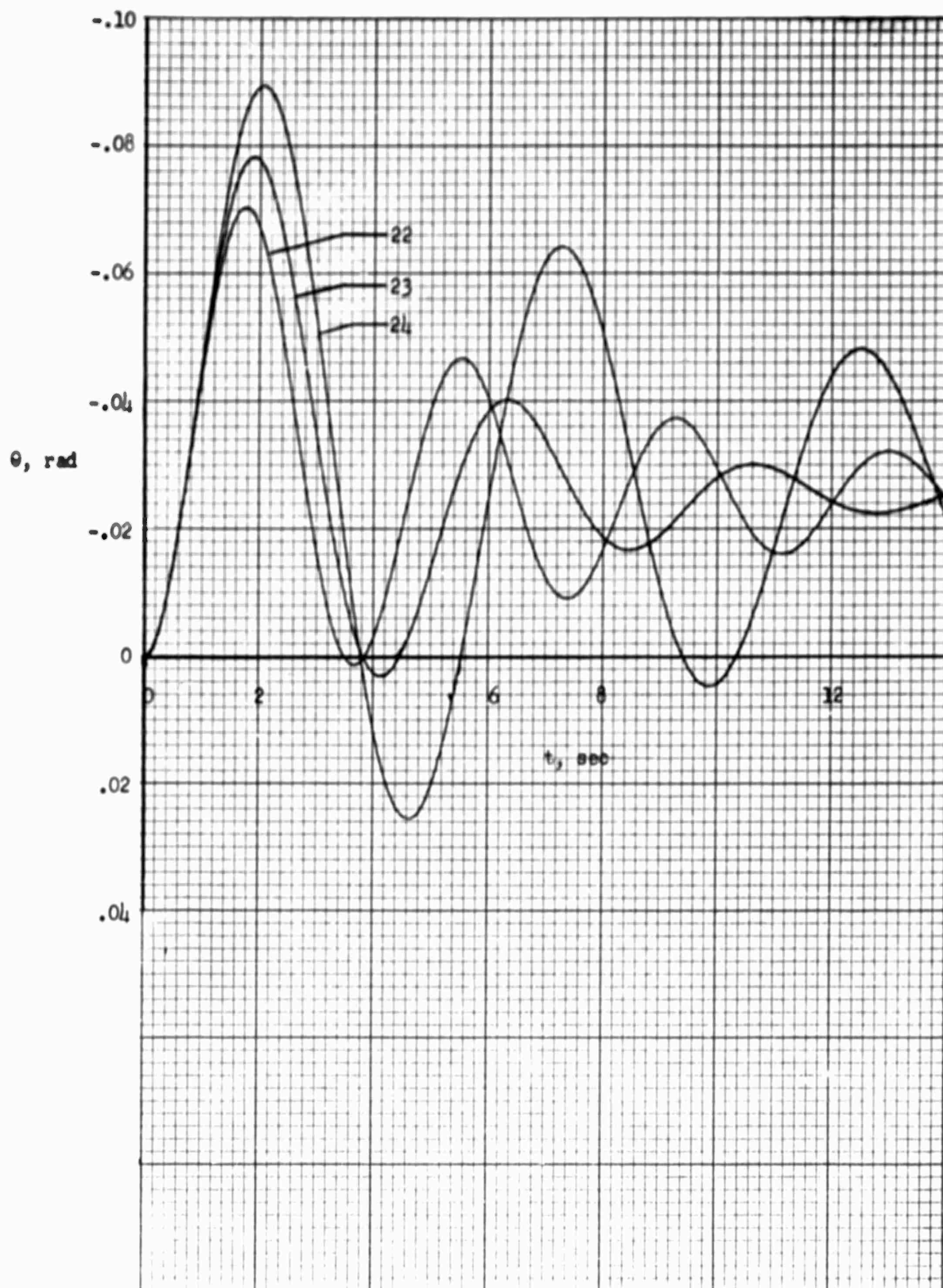
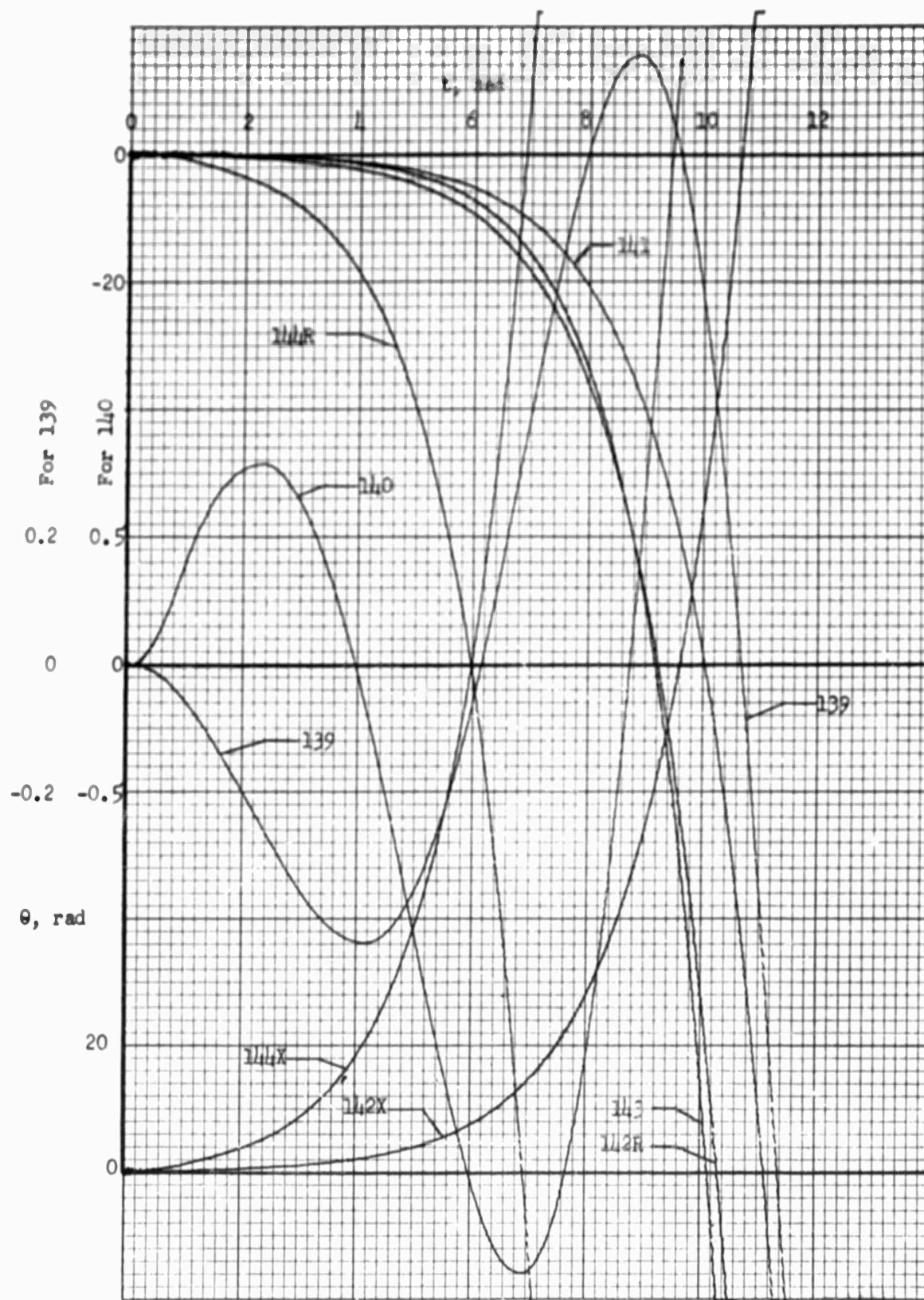FIGURE 26: PITCH ANGLE RESPONSE TO CONTROL MOMENT STEP INPUT
FOR CASE NOS. 22, 23, 24
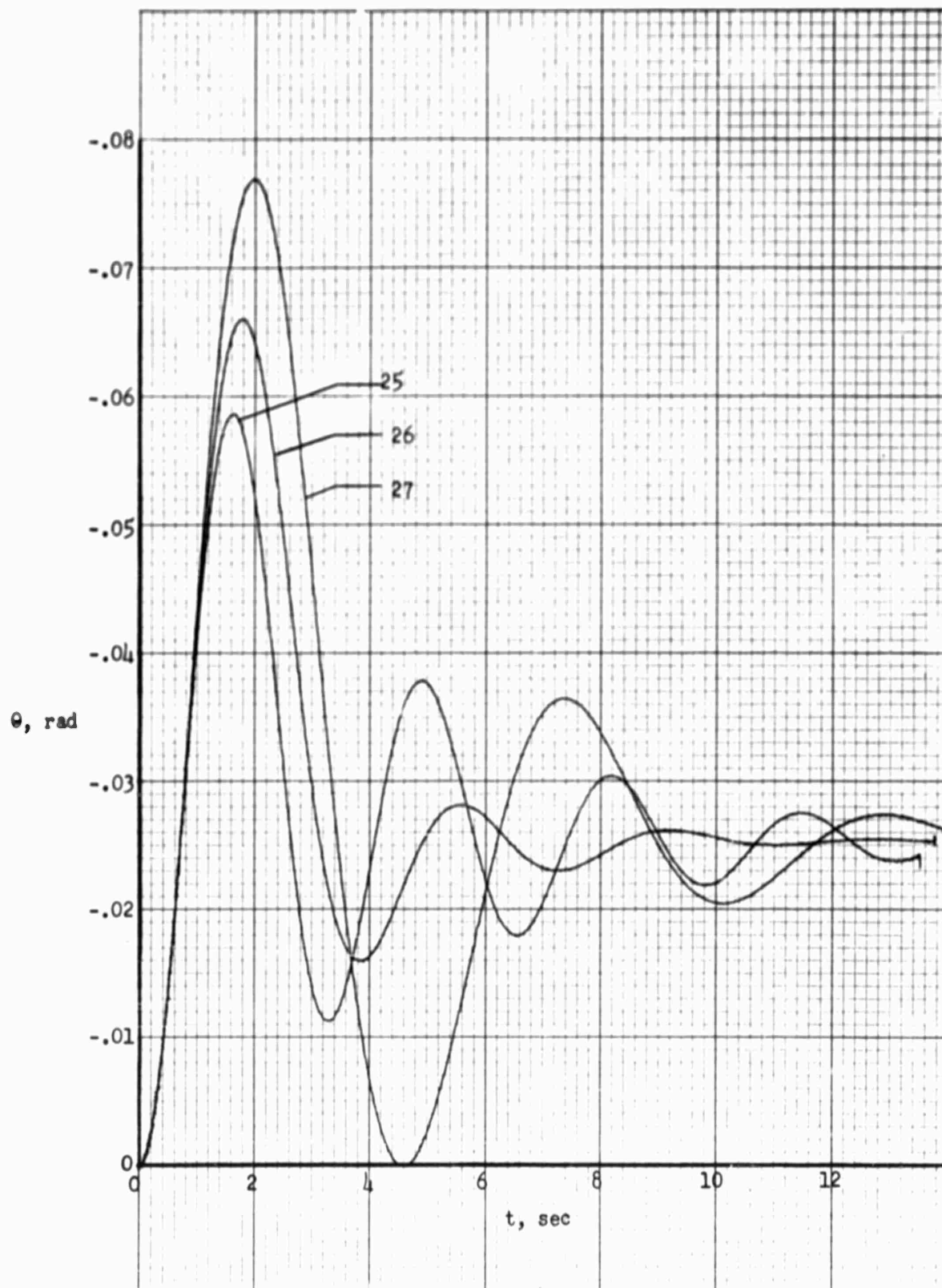
FIGURE 27: PITCH ANGLE RESPONSE TO CONTROL MOMENT STEP INPUT
FOR CASE NOS. 25, 26, 27
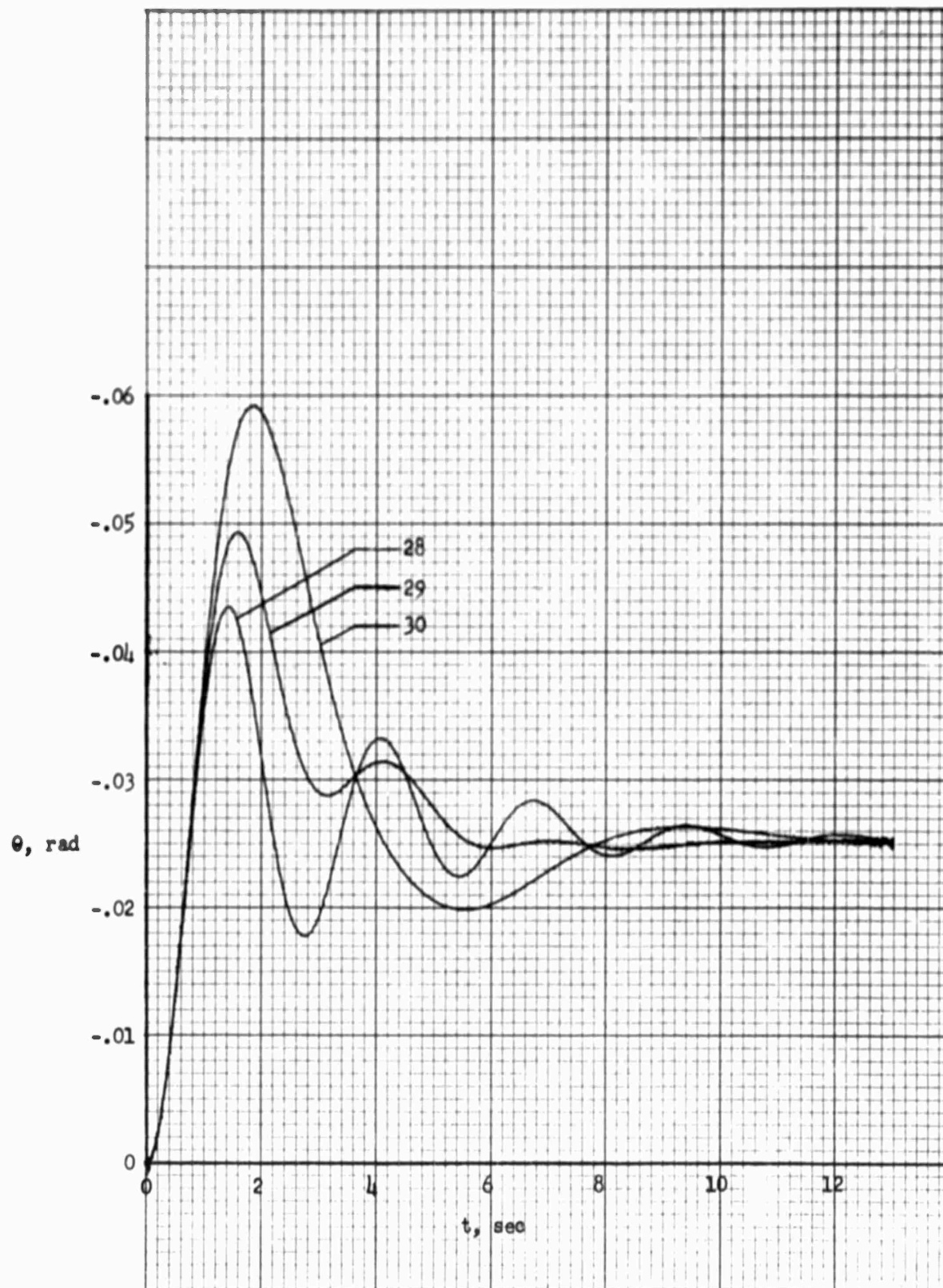
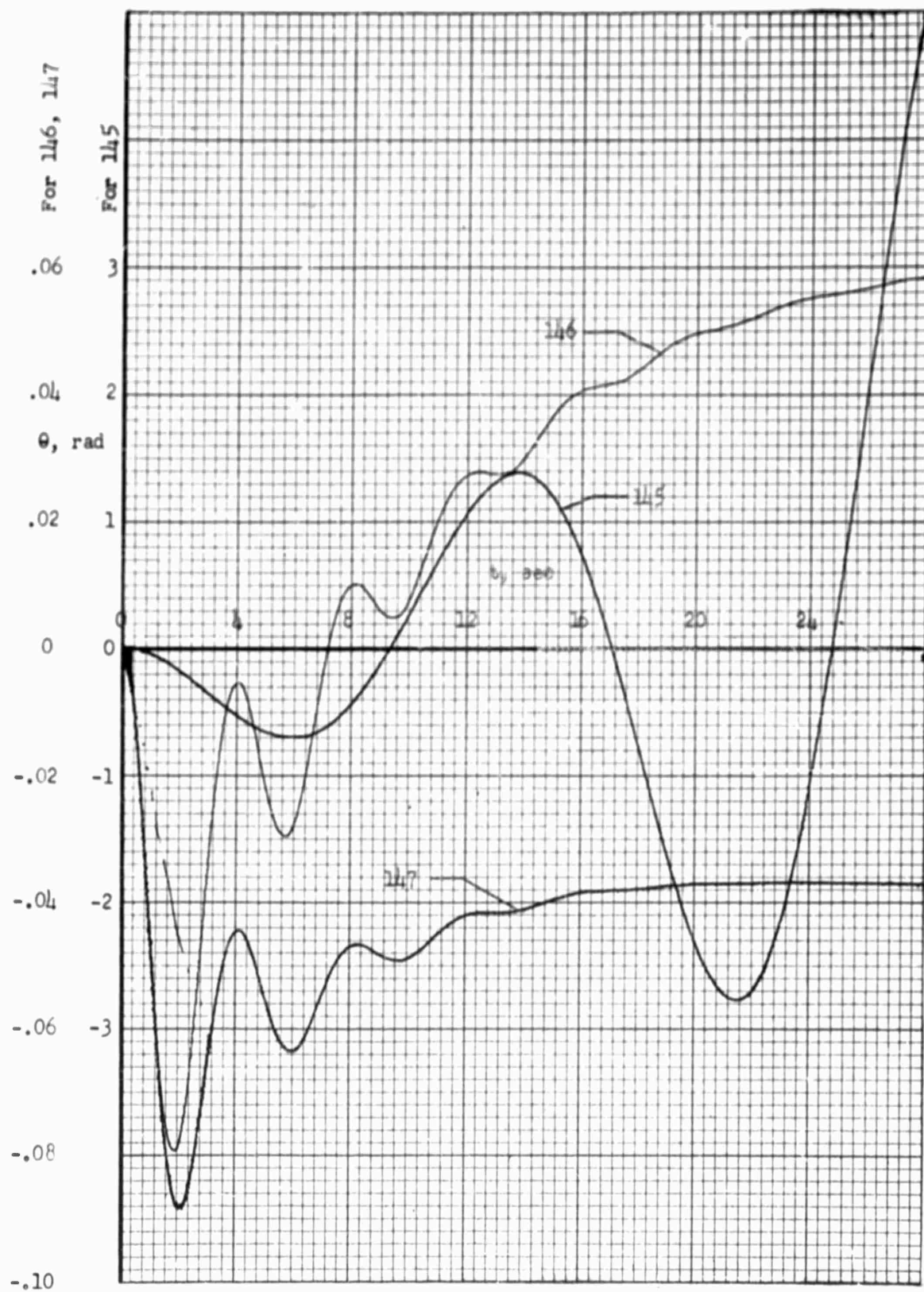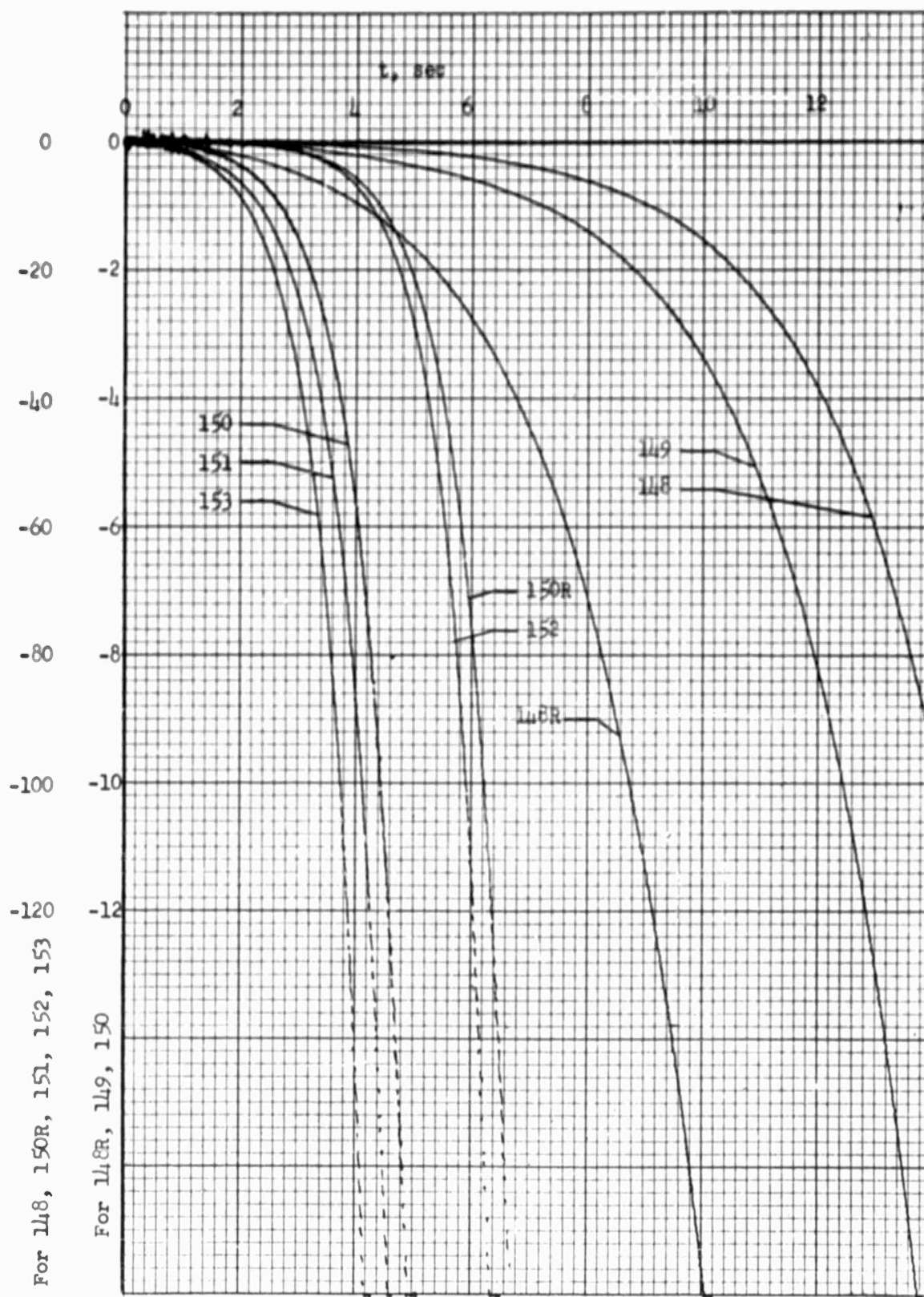FIGURE 28: PITCH ANGLE RESPONSE TO CONTROL MOMENT STEP INPUT
FOR CASE NOS. 28, 29, 30
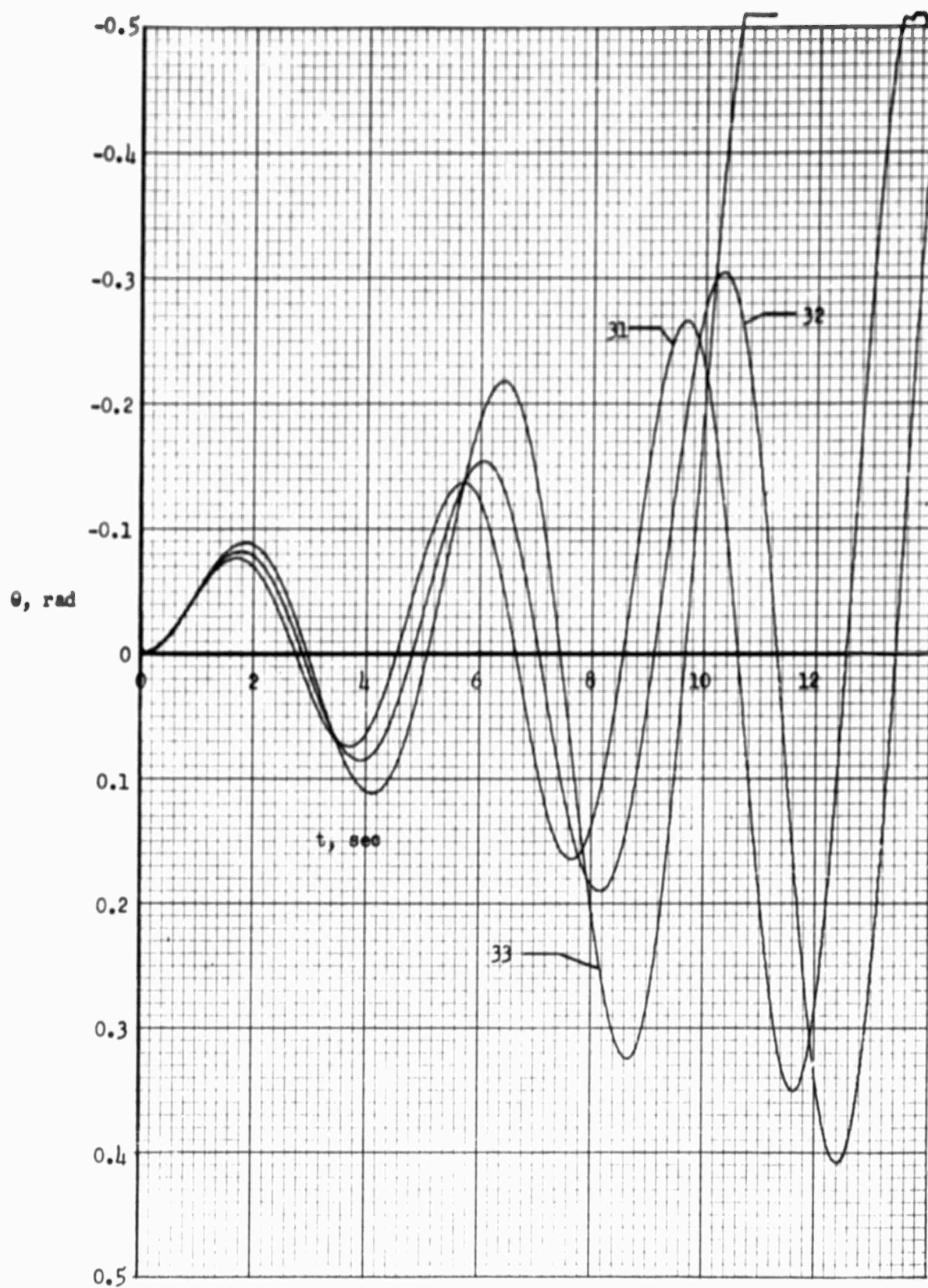
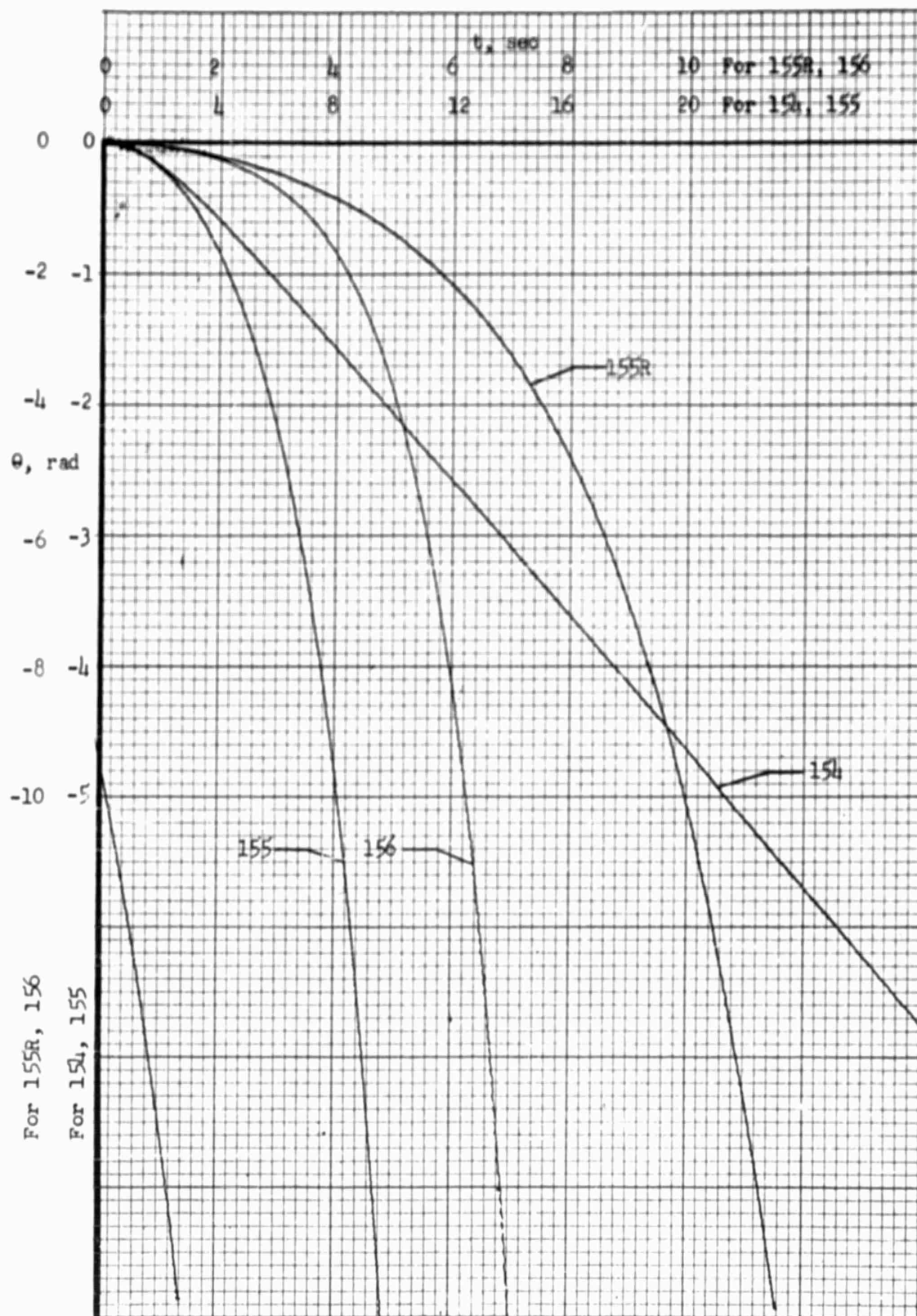FIGURE 29: PITCH ANGLE RESPONSE TO CONTROL MOMENT STEP INPUT
FOR CASE NOS. 31, 32, 33
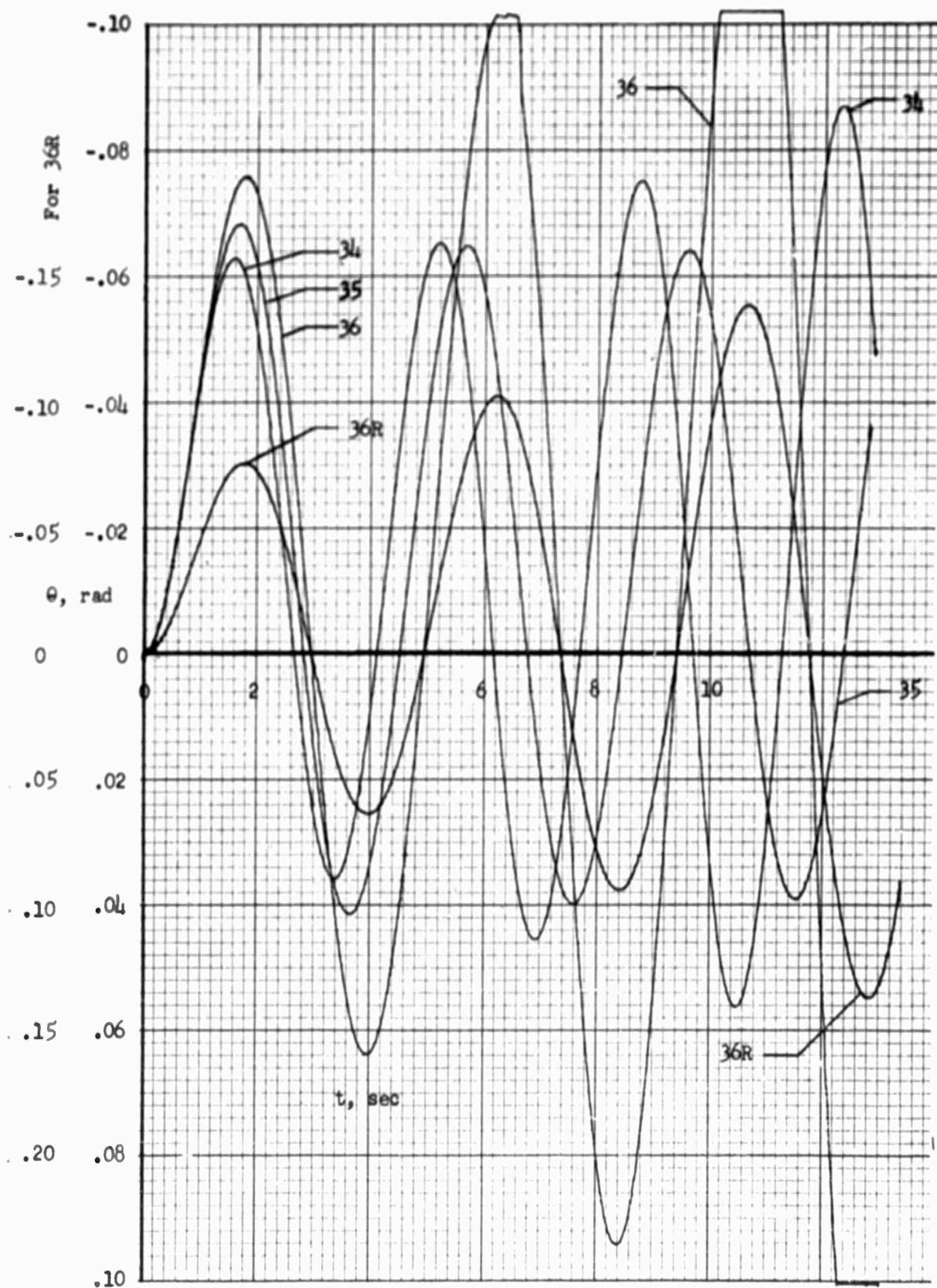
FIGURE 30: PITCH ANGLE RESPONSE TO CONTROL MOMENT STEP INPUT
FOR CASE NOS. 34, 35, 36R
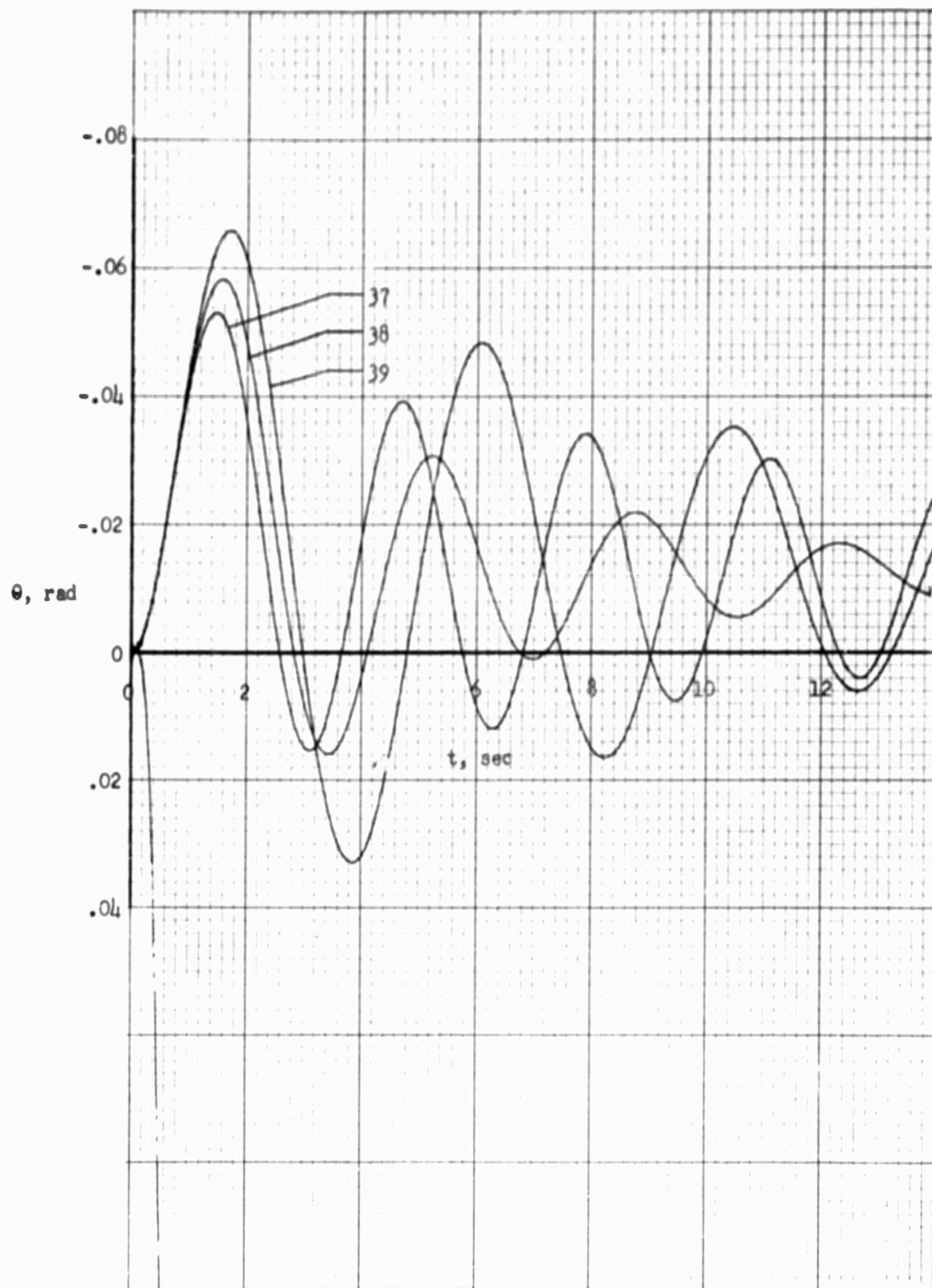
FIGURE 31: PITCH ANGLE RESPONSE TO CONTROL MOMENT STEP INPUT
FOR CASE NOS. 37, 38, 39
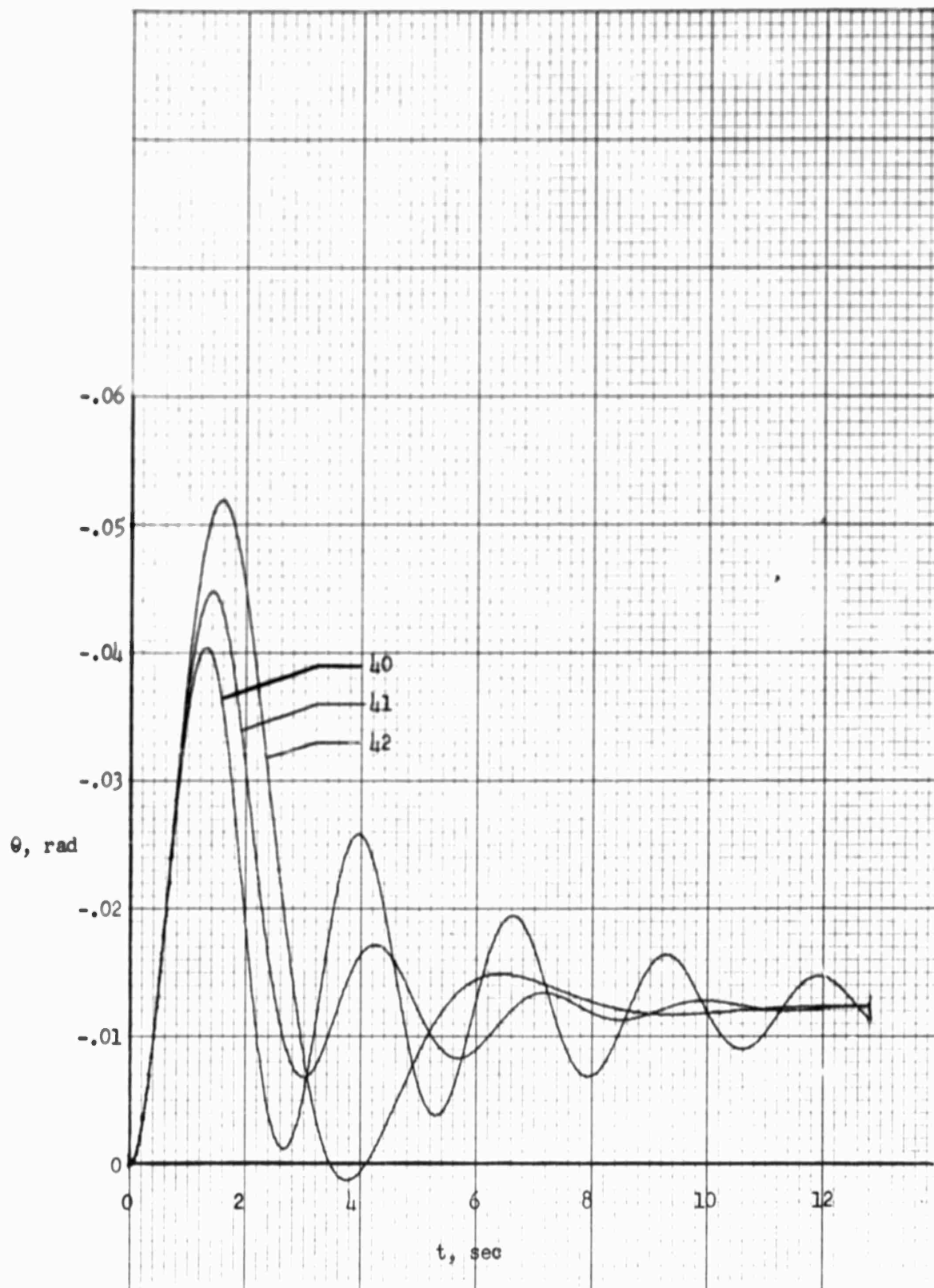
FIGURE 32: PITCH ANGLE RESPONSE TO CONTROL MOMENT STEP INPUT
FOR CASE NOS. 40, 41, 42
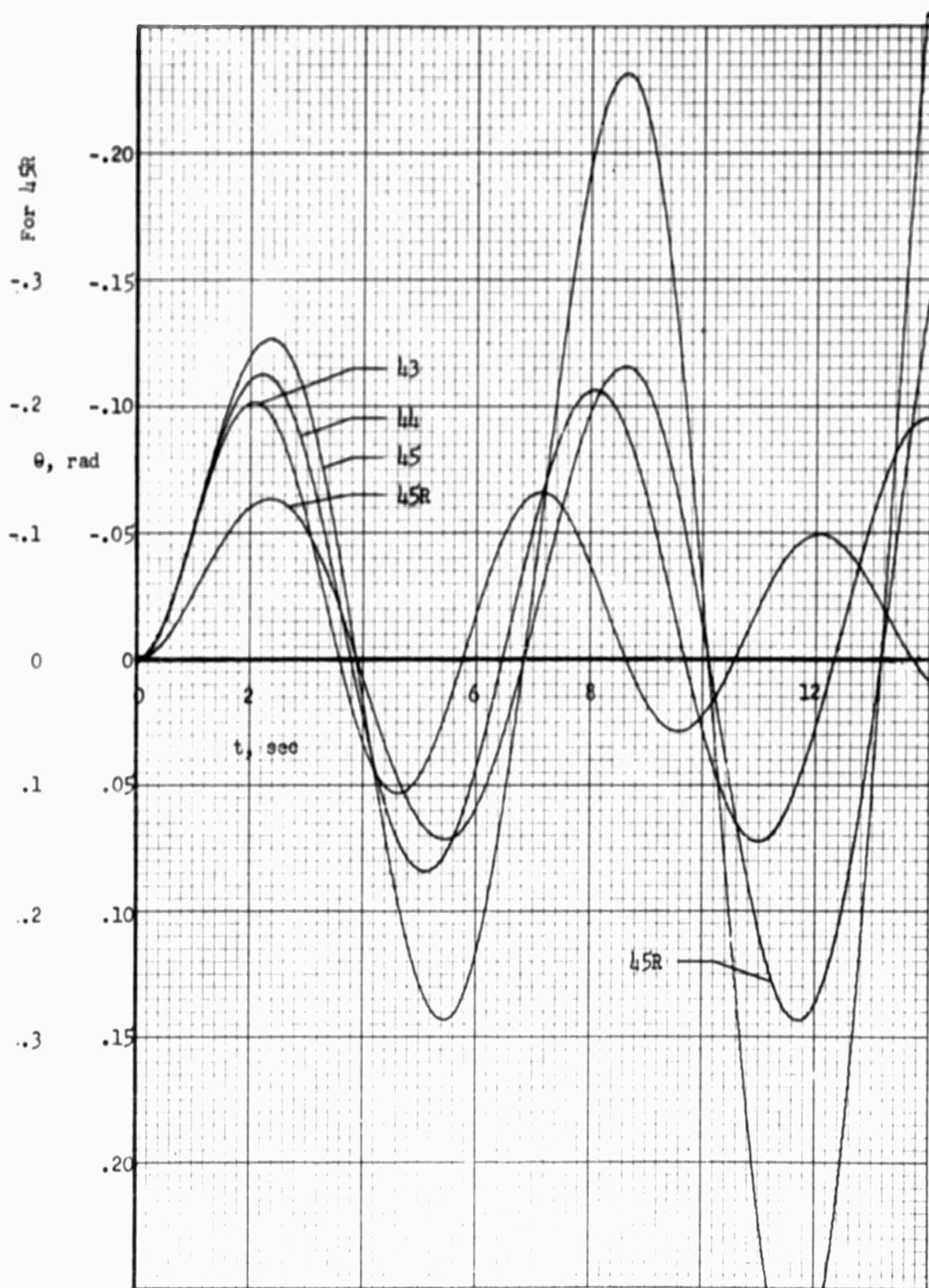
FIGURE 33: PITCH ANGLE RESPONSE TO CONTROL MOMENT STEP INPUT
FOR CASE NOS. 43, 44, 45R
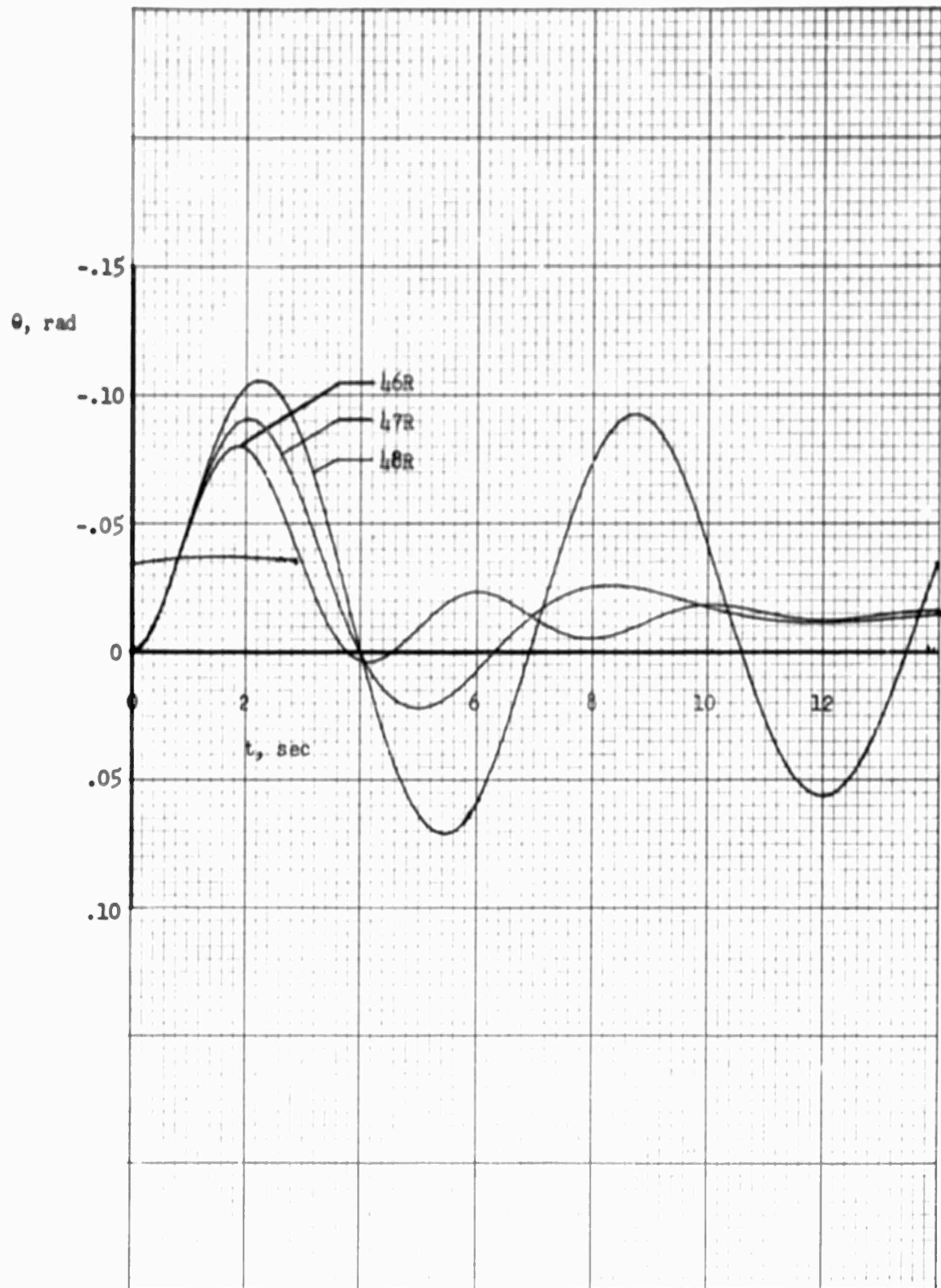
FIGURE 34: PITCH ANGLE RESPONSE TO CONTROL MOMENT STEP INPUT
FOR CASE NOS. 46R, 47R, 48R
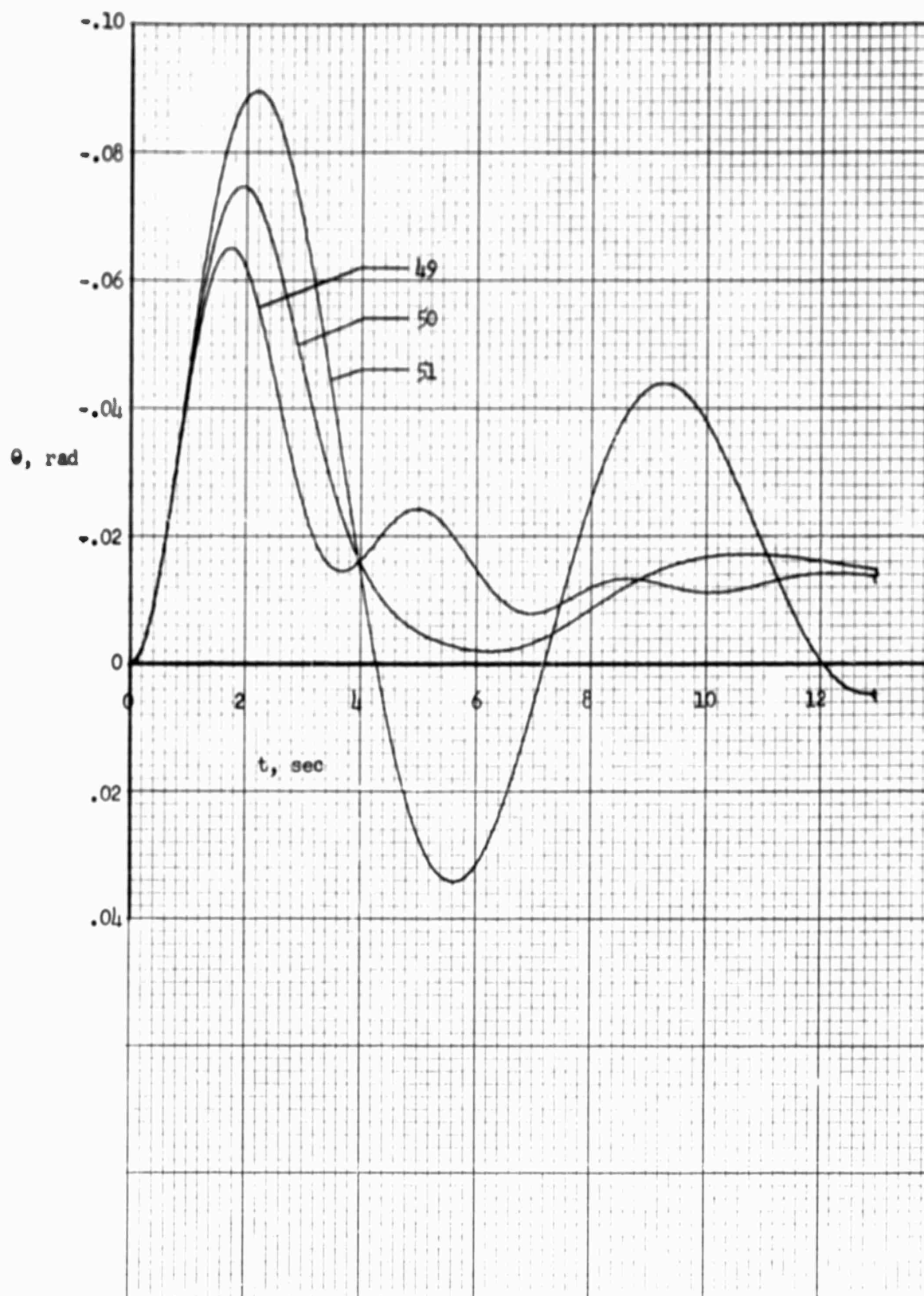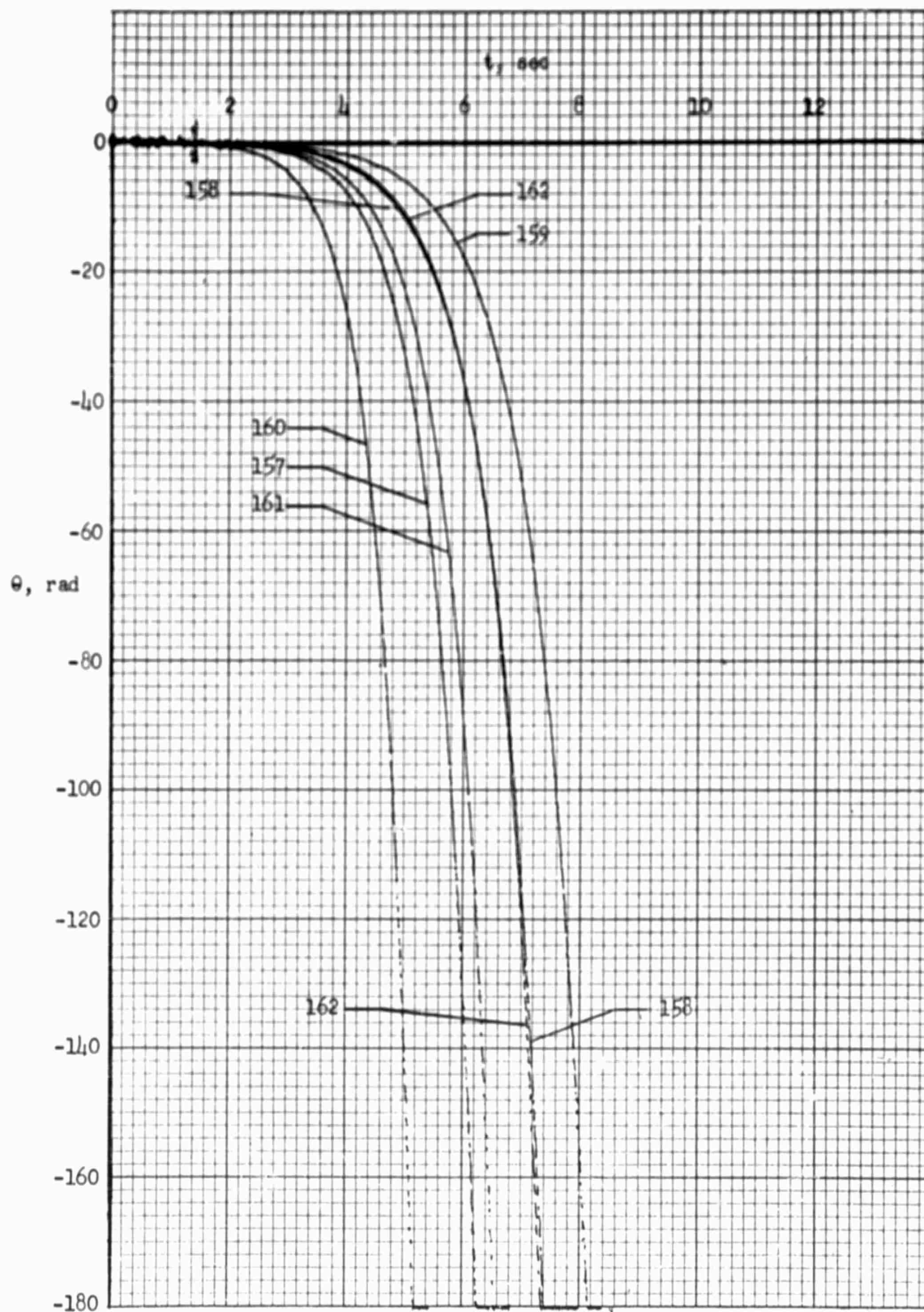
FIGURE 35: PITCH ANGLE RESPONSE TO CONTROL MOMENT SETP INPUT
FOR CASE NOS. 49, 50, 51
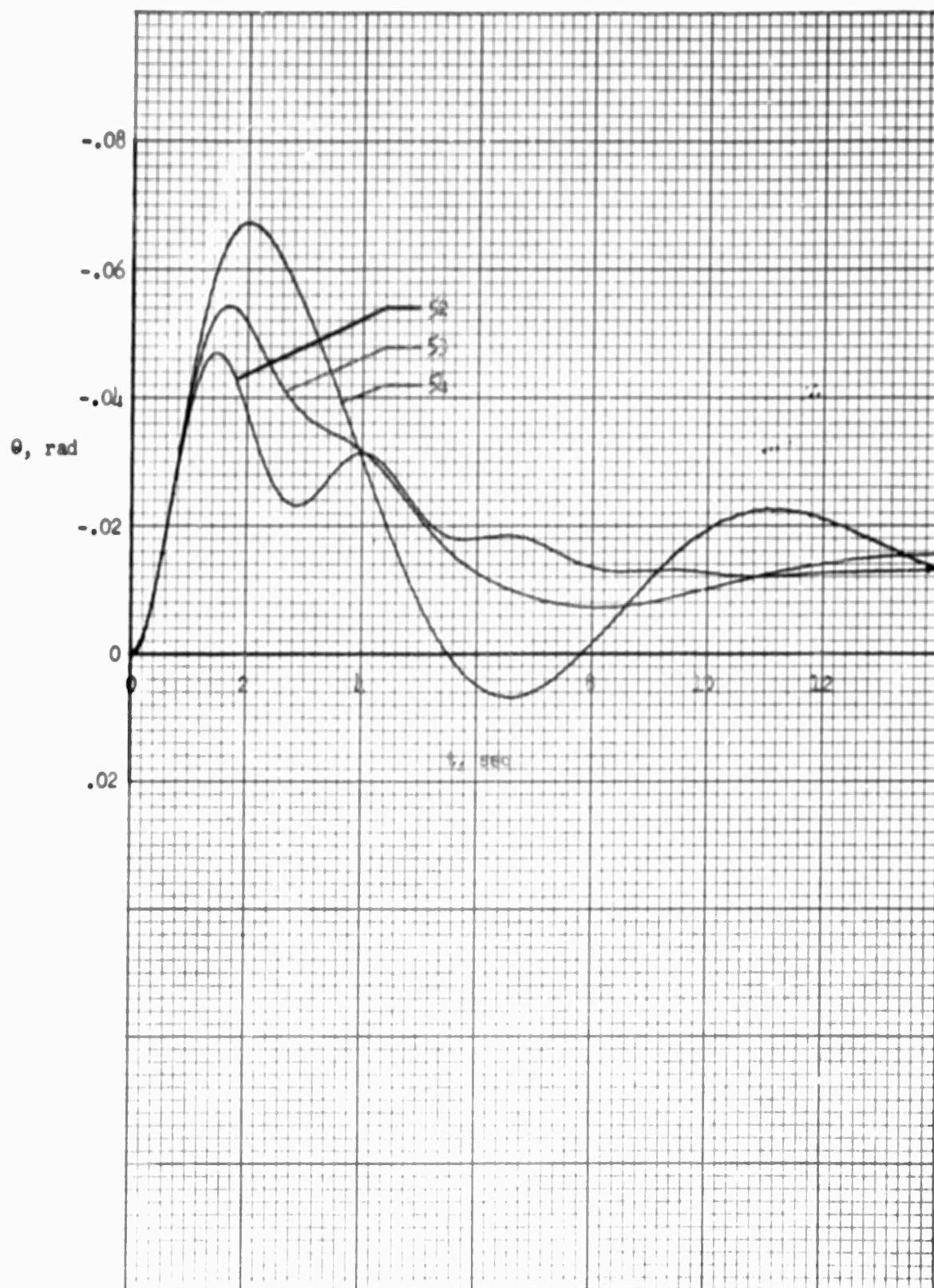
FIGURE 36: PITCH ANGLE RESPONSE TO CONTROL MOMENT STEP INPUT
FOR CASE NOS. 52, 53, 54

FIGURE 37: PITCH ANGLE RESPONSE TO CONTROL MOMENT STEP INPUT
FOR CASE NOS. 55, 57
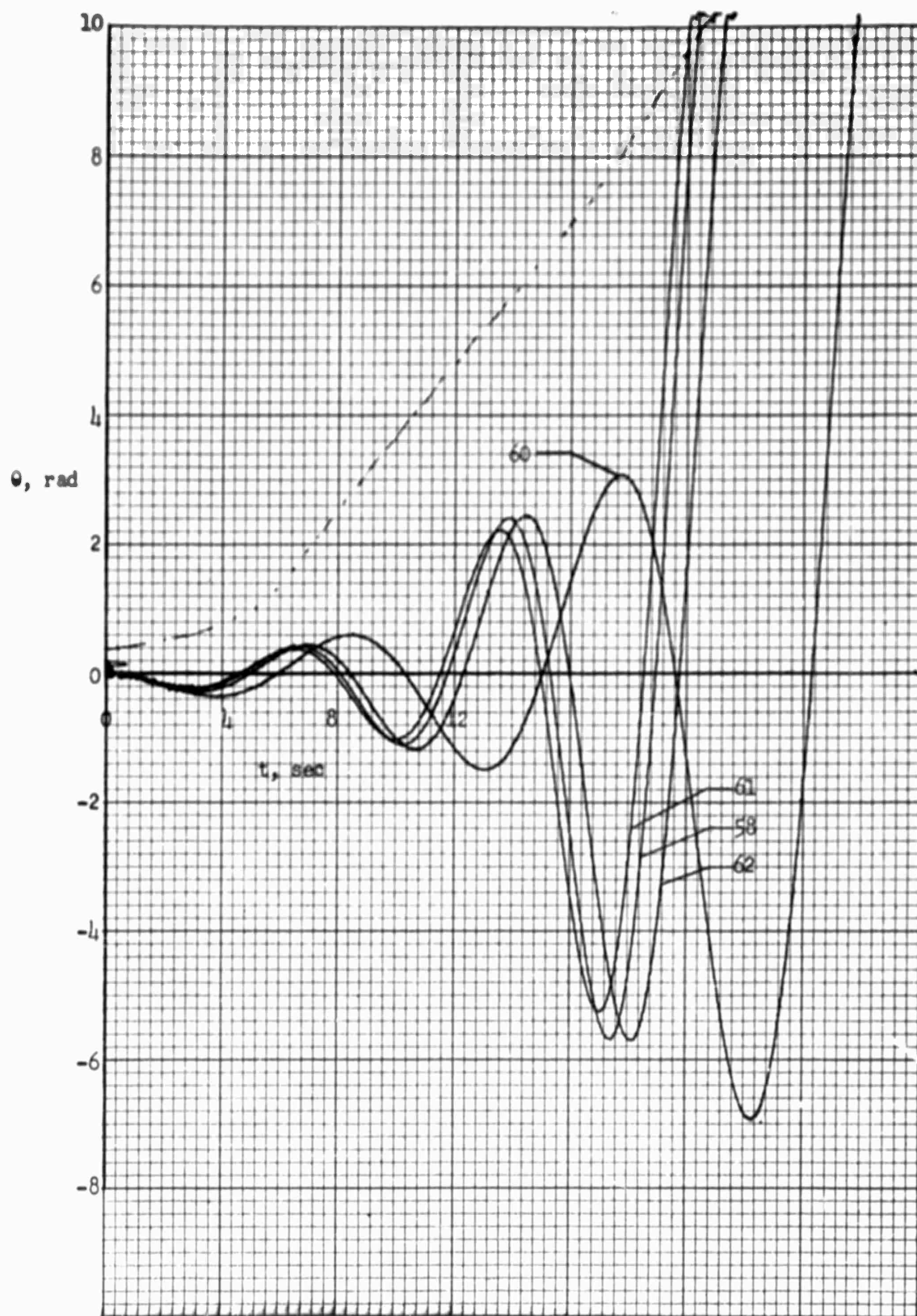
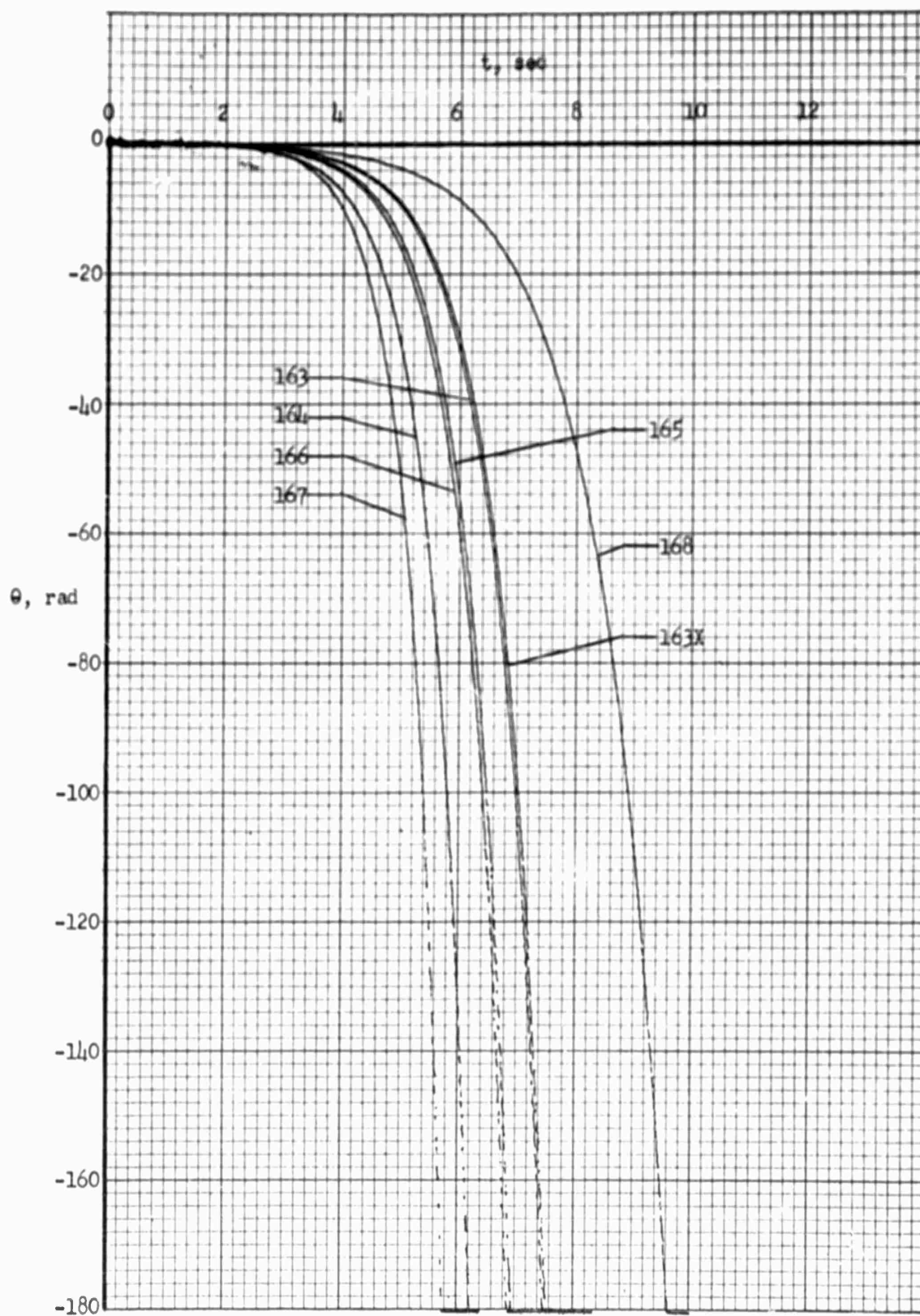FIGURE 38: PITCH ANGLE RESPONSE TO CONTROL MOMENT STEP INPUT
FOR CASE NOS. 58, 60, 61, 62
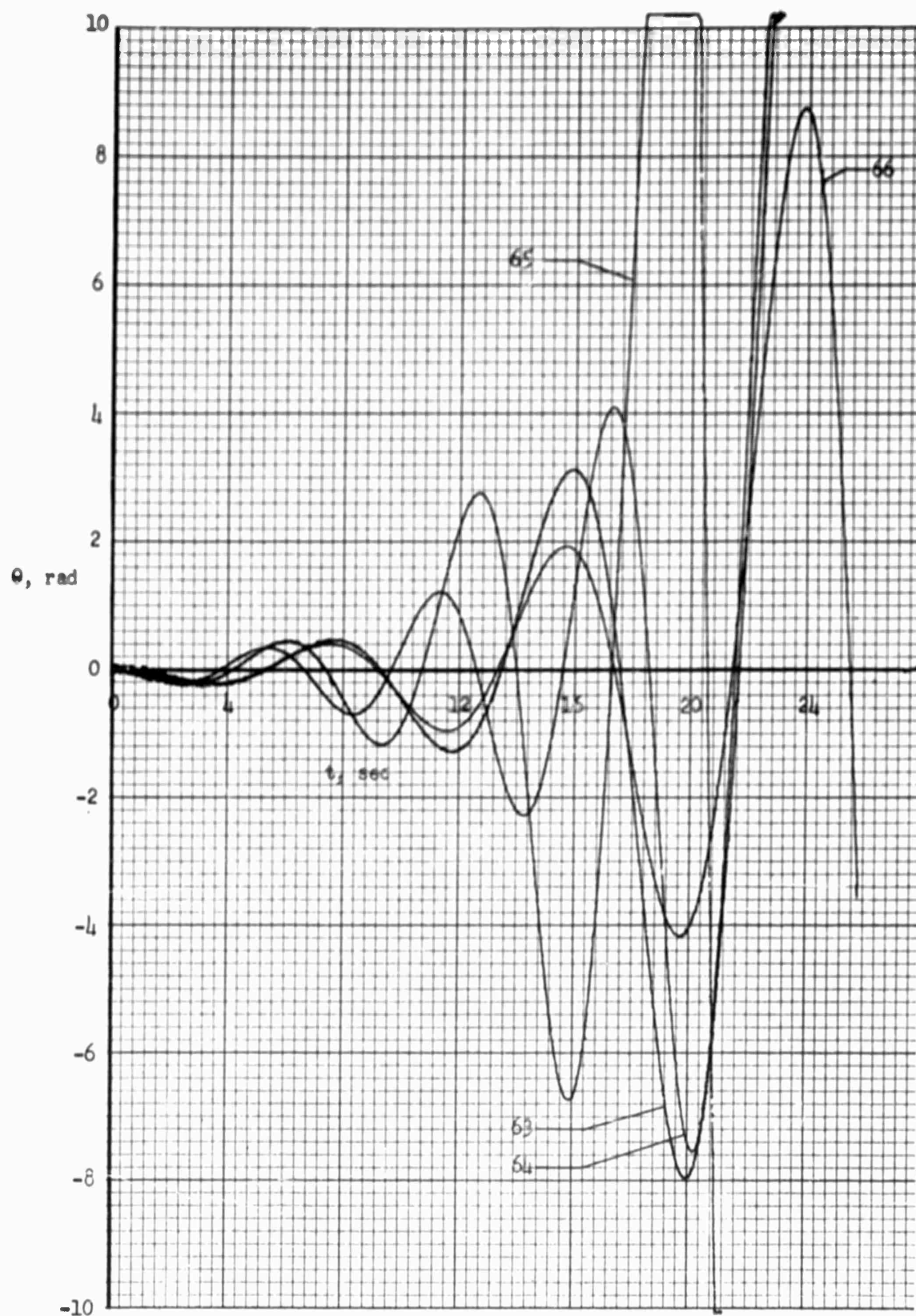
FIGURE 39:   PITCH ANGLE RESPONSE TO CONTROL MOMENT STEP INPUT
FOR CASE NOS. 63, 64, 65, 66
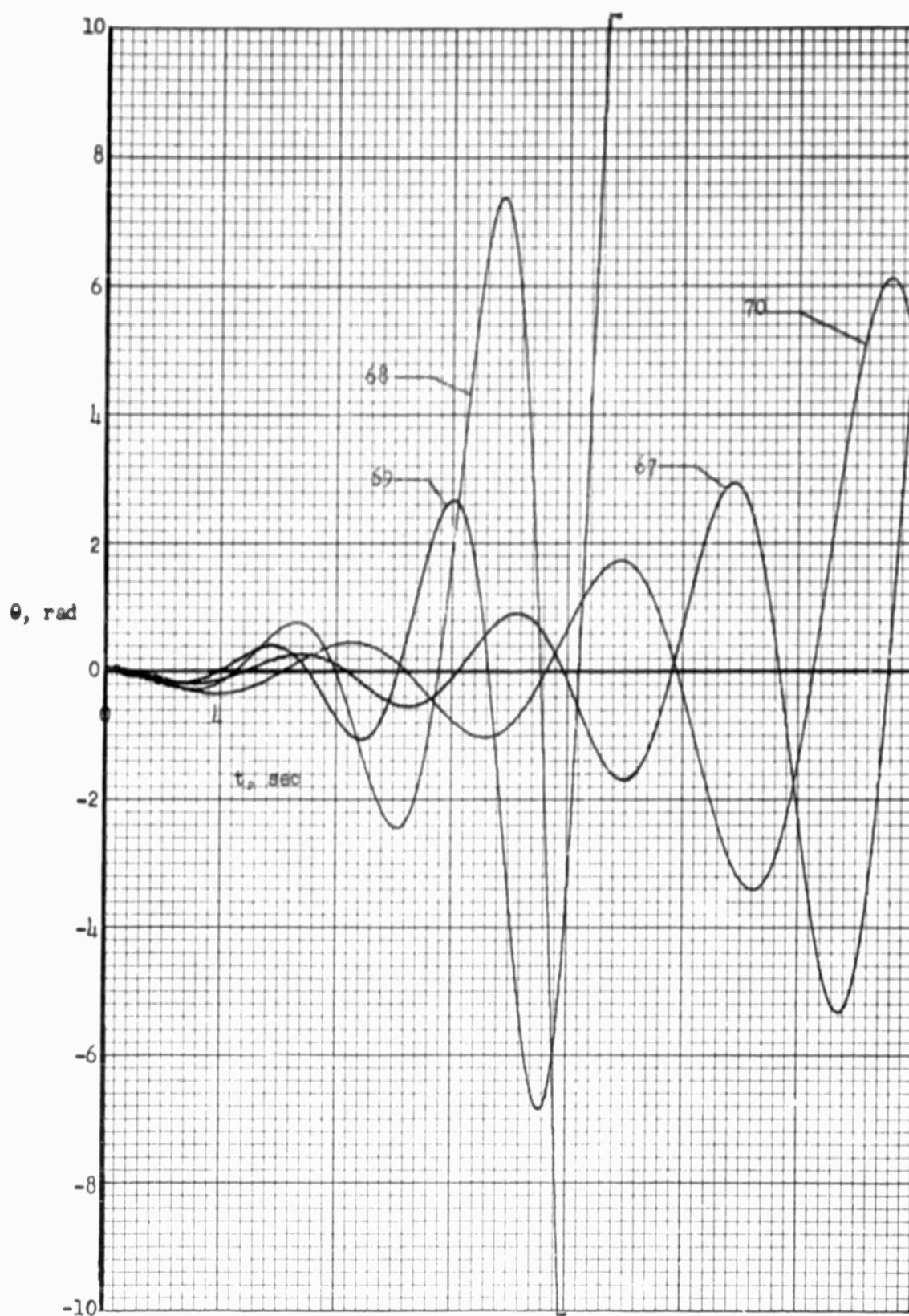
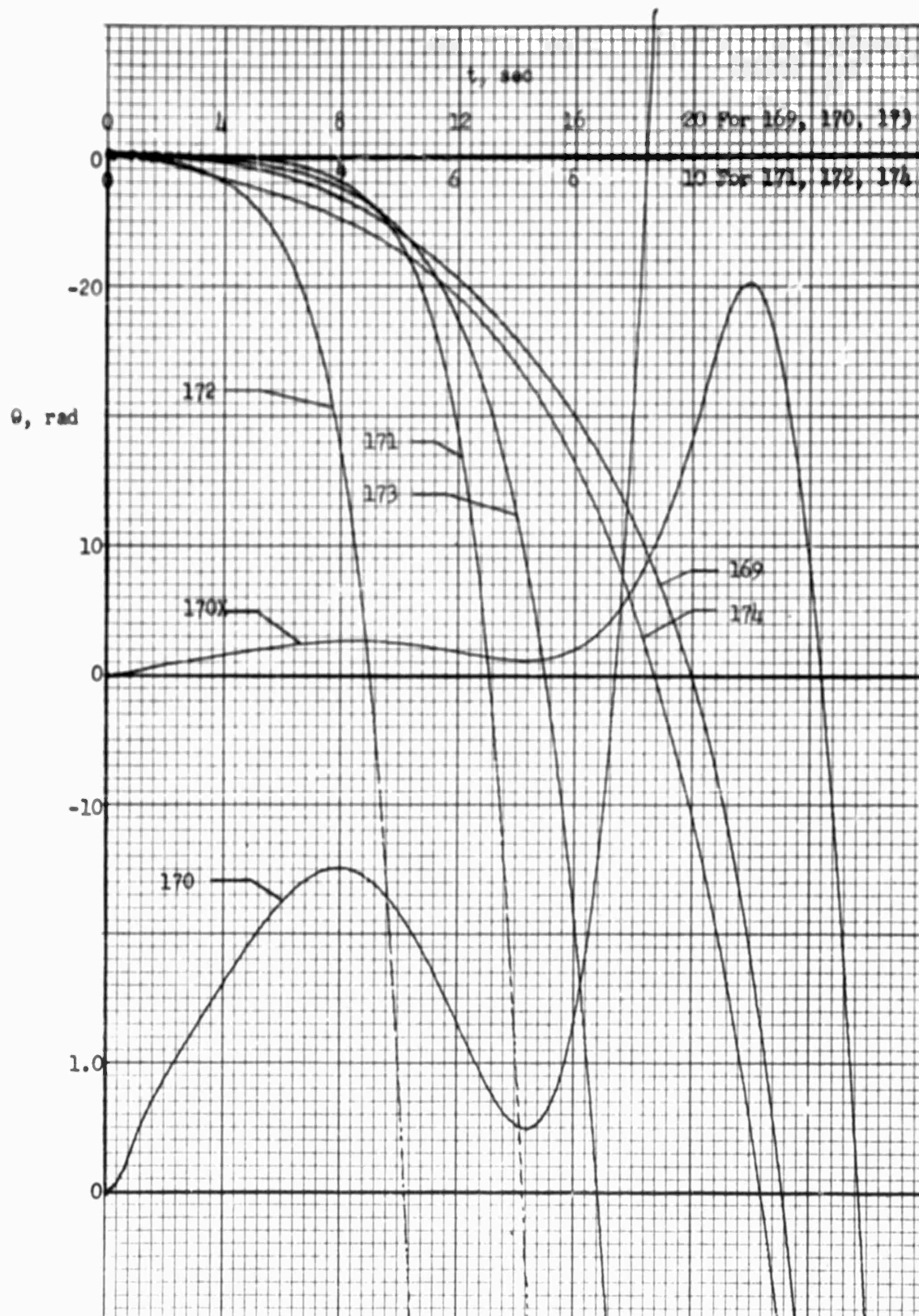FIGURE 40: PITCH ANGLE RESPONSE TO CONTROL MOMENT STEP INPUT
FOR CASE NOS. 67, 68, 69, 70
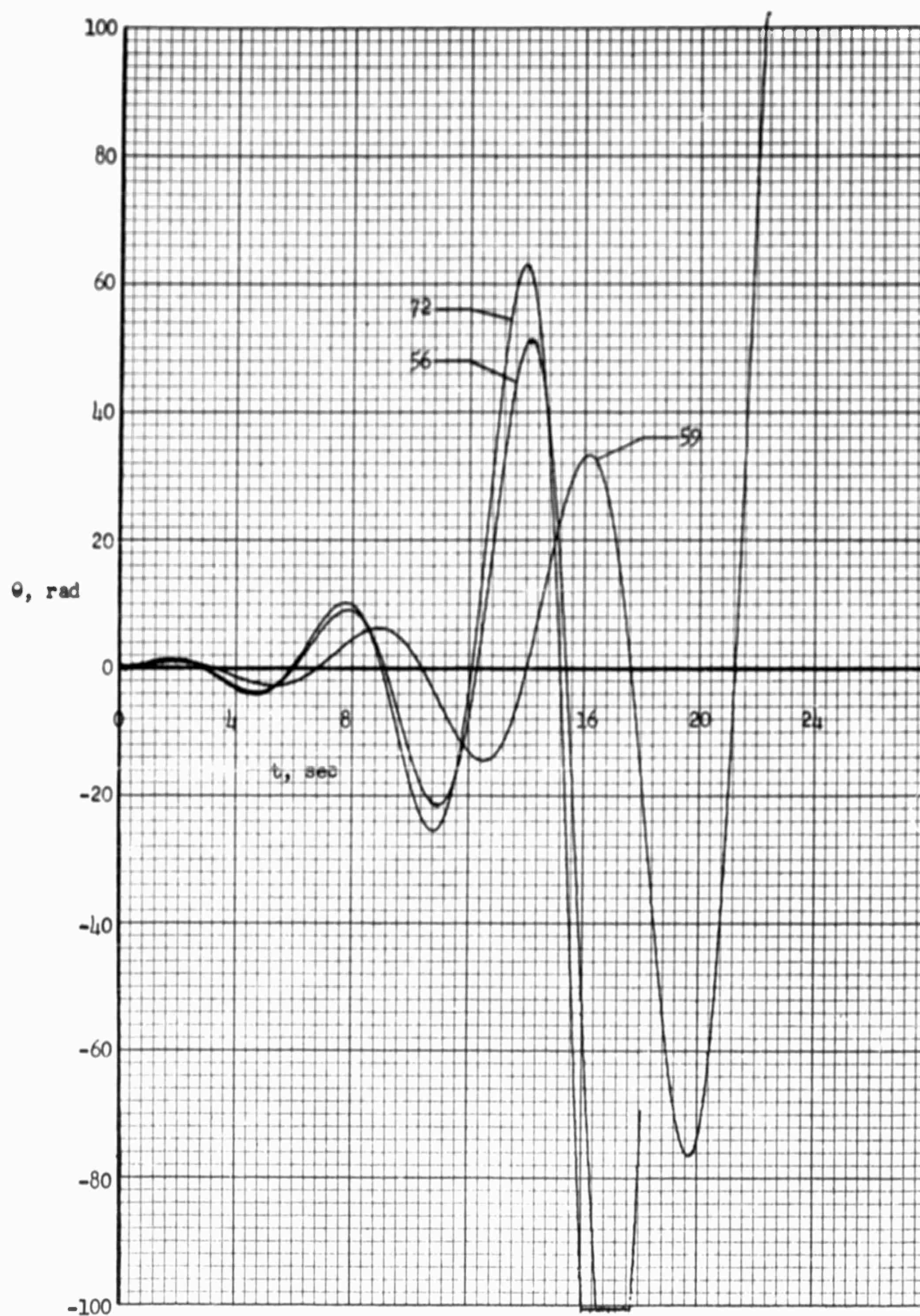
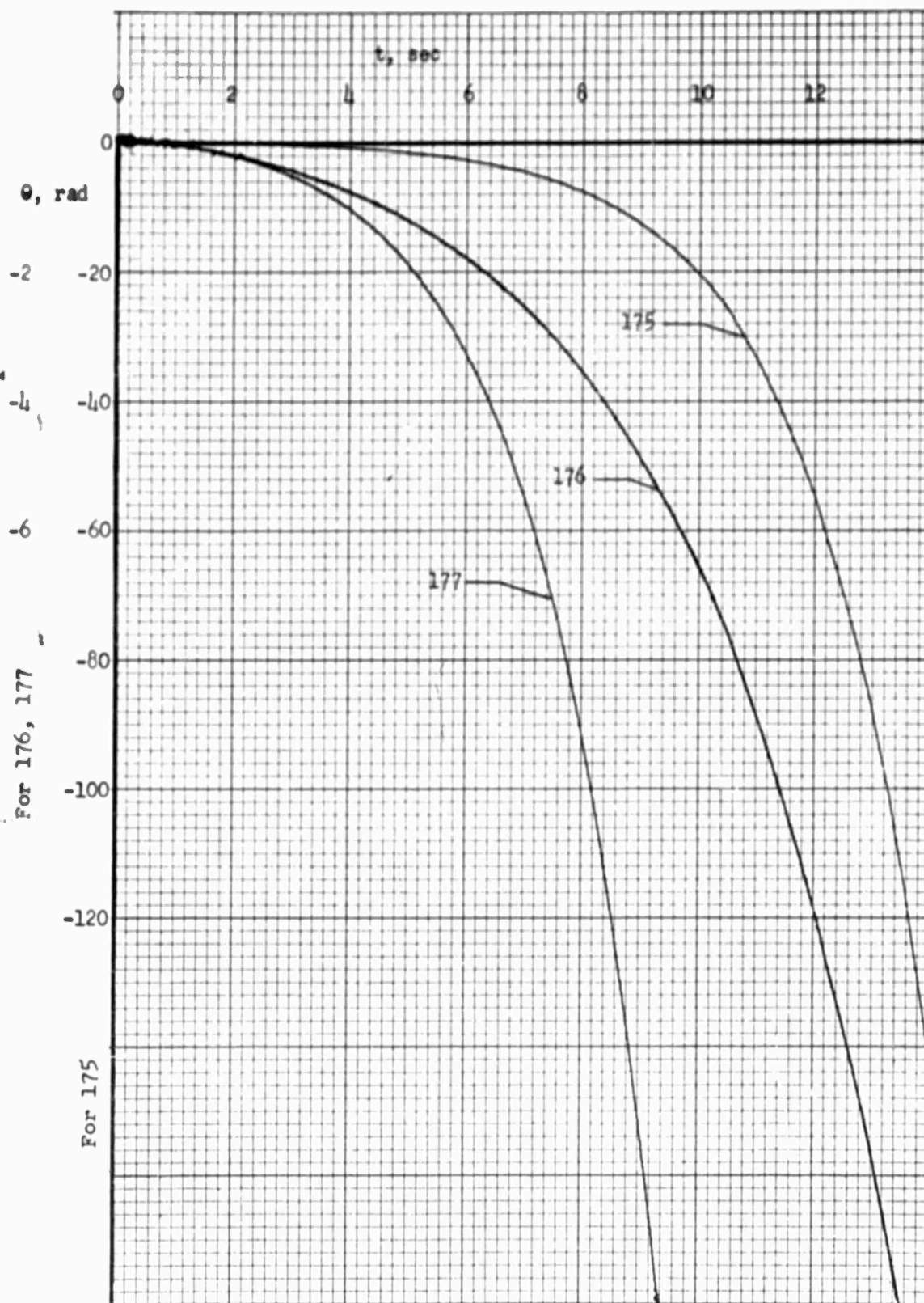FIGURE 41: PITCH ANGLE RESPONSE TO HORIZONTAL GUST PULSE INPUT
FOR CASE NOS. 56, 59, 72
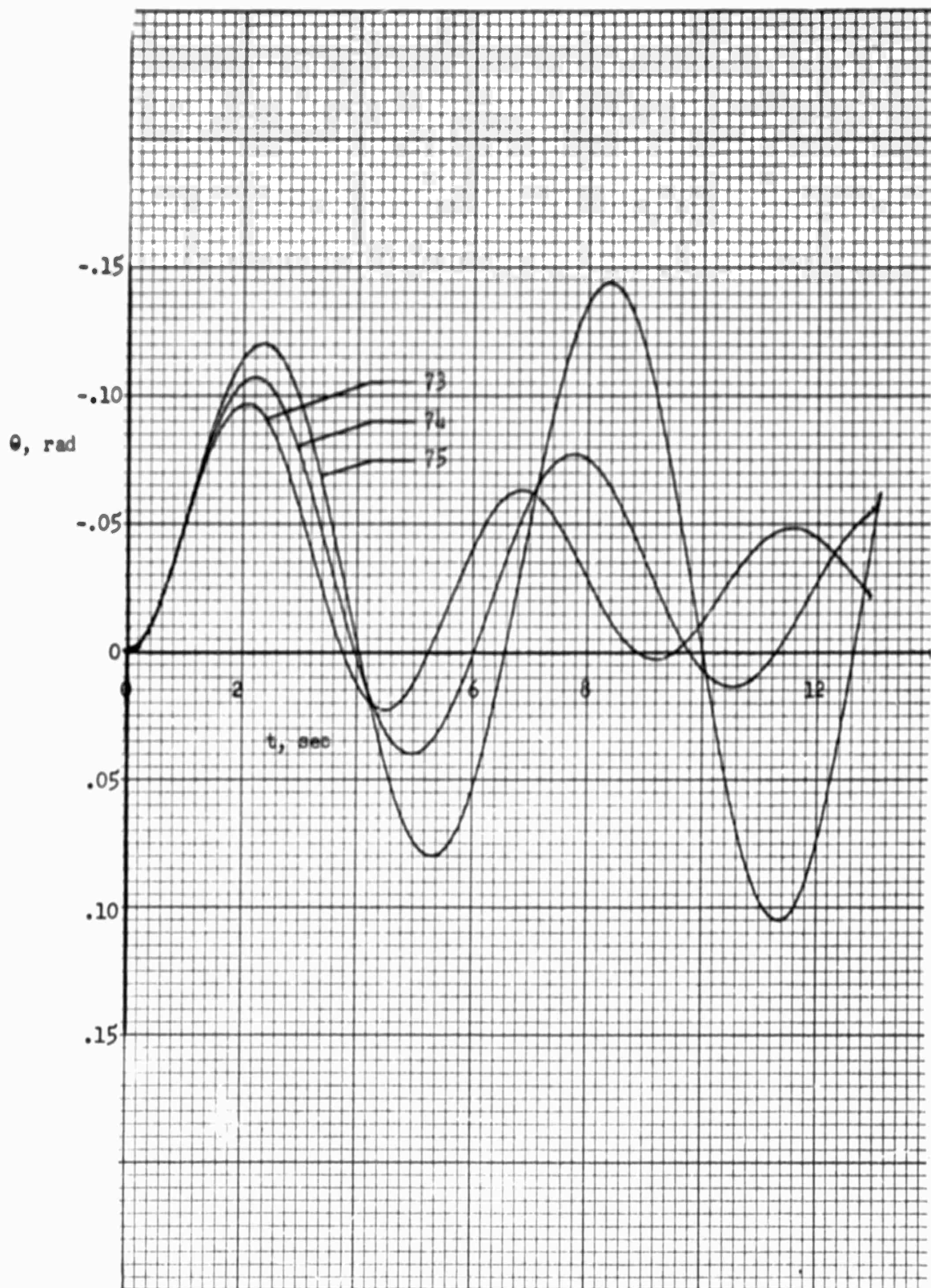
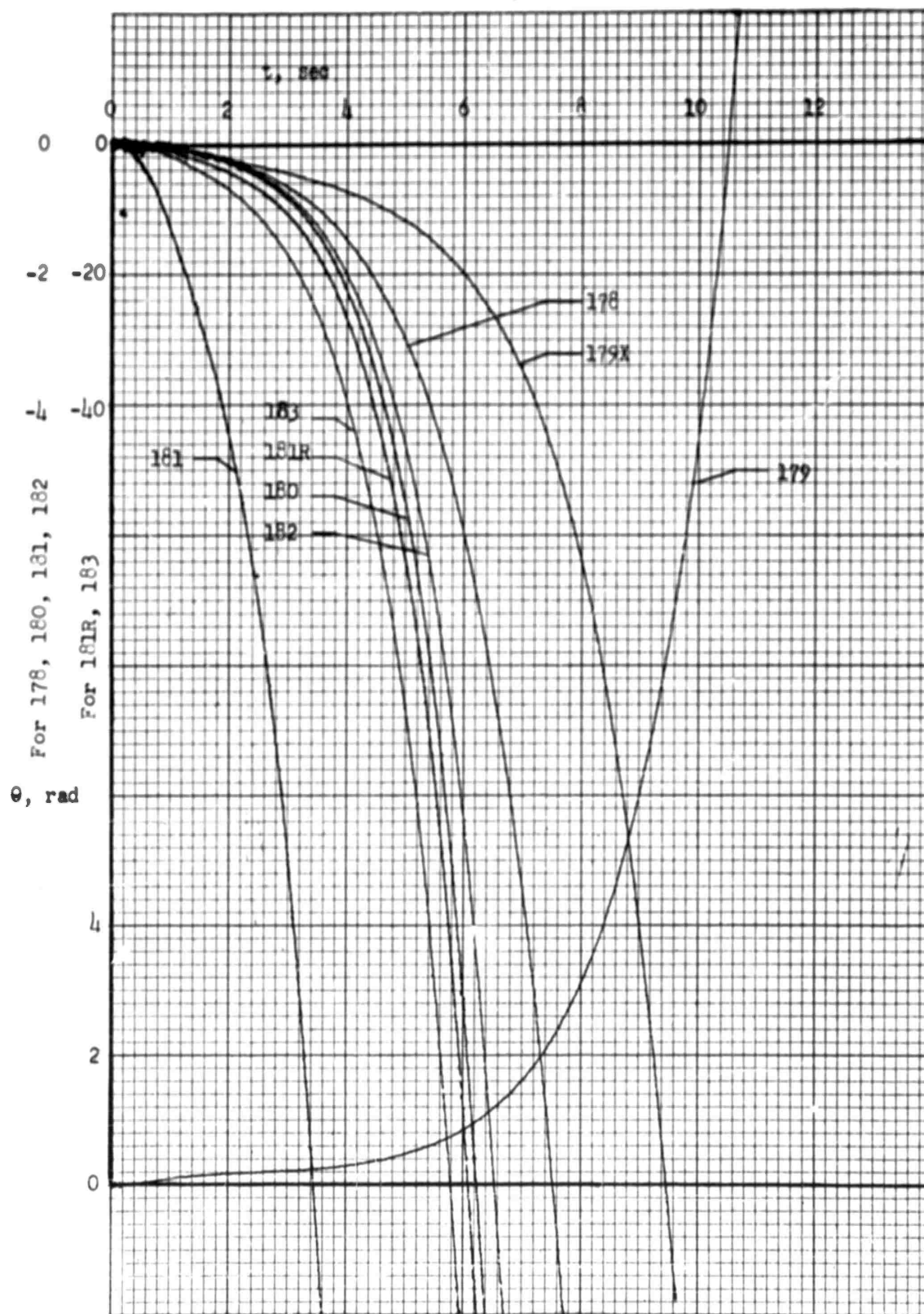FIGURE 42: PITCH ANGLE RESPONSE TO CONTROL MOMENT STEP INPUT
FOR CASE NOS. 73, 74, 75
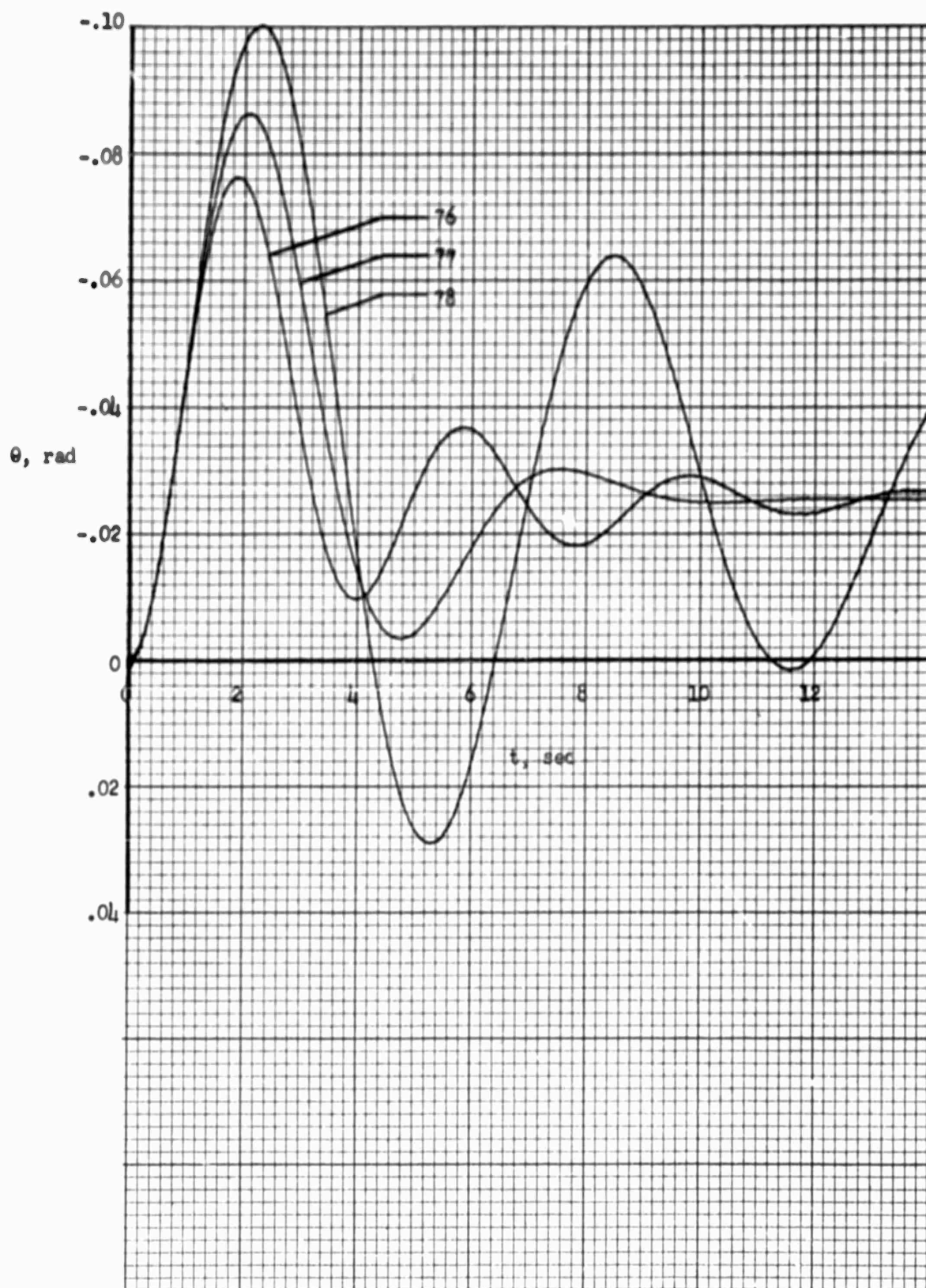
FIGURE 43: PITCH ANGLE RESPONSE TO CONTROL MOMENT STEP INPUT
FOR CASE NOS. 76, 77, 78
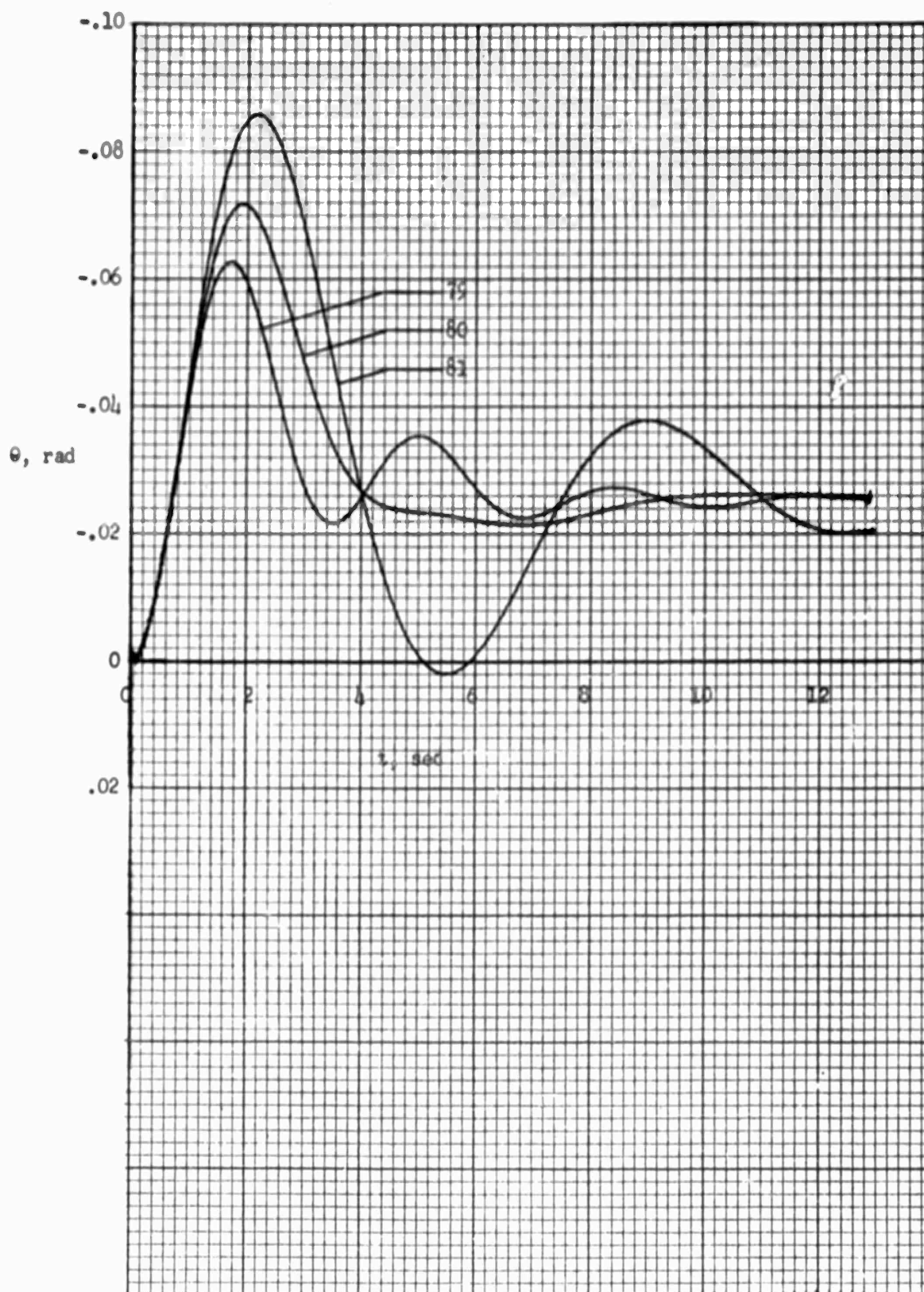
FIGURE 44: PITCH ANGLE RESPONSE TO CONTROL MOMENT STEP INPUT
FOR CASE NOS. 79, 80, 81
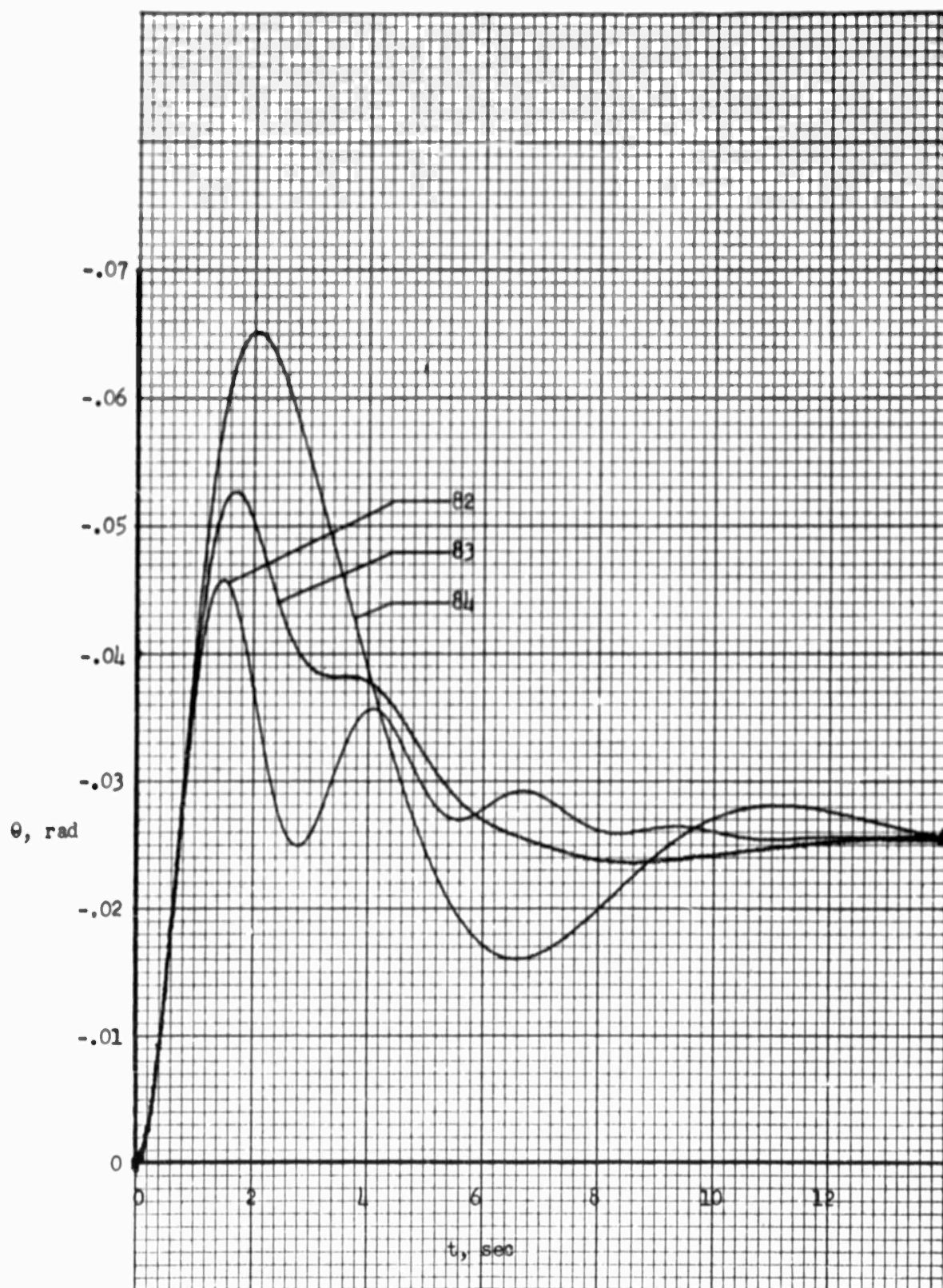
FIGURE 45: PITCH ANGLE RESPONSE TO CONTROL MOMENT STEP INPUT
FOR CASE NOS. 82, 83, 84
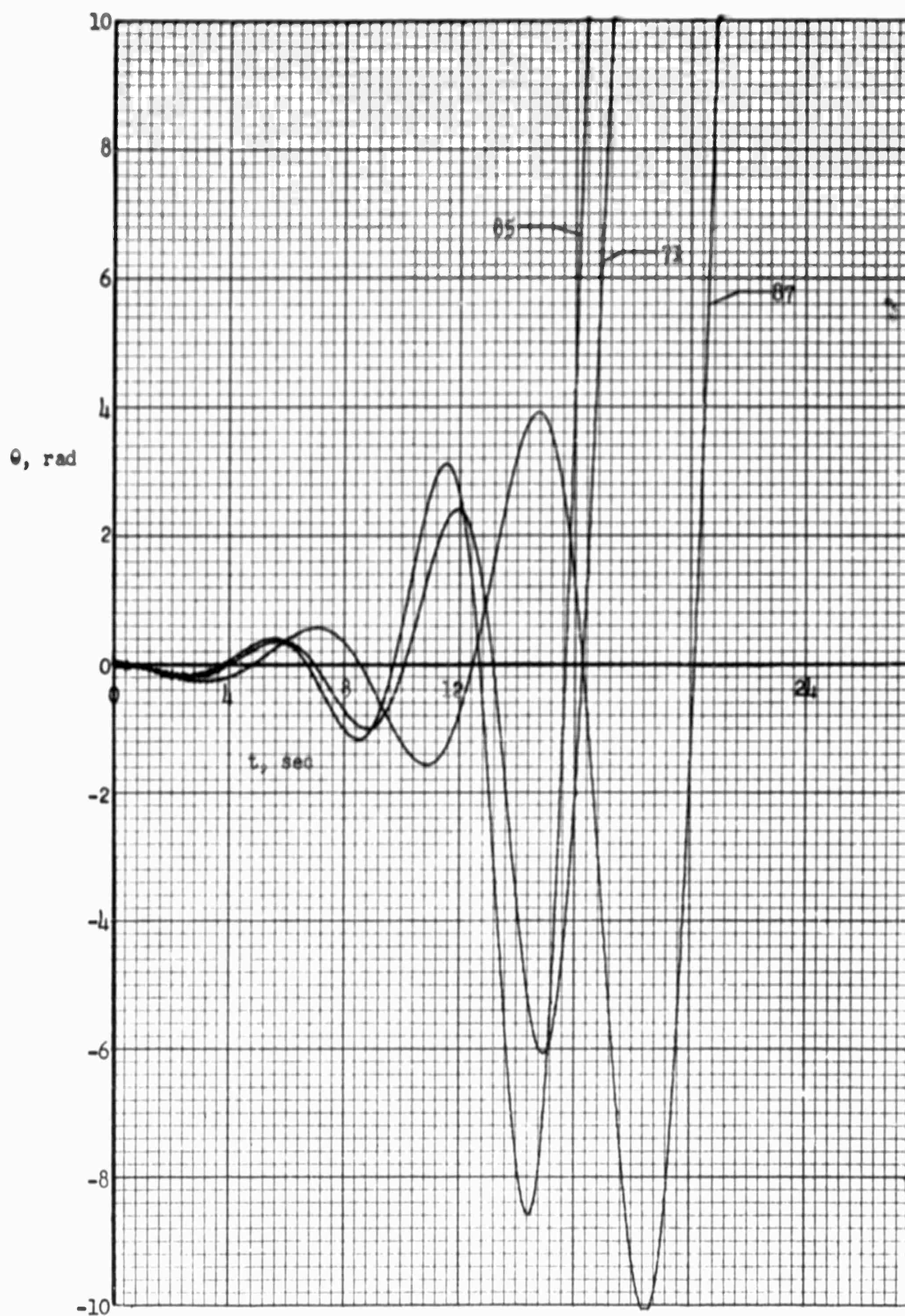
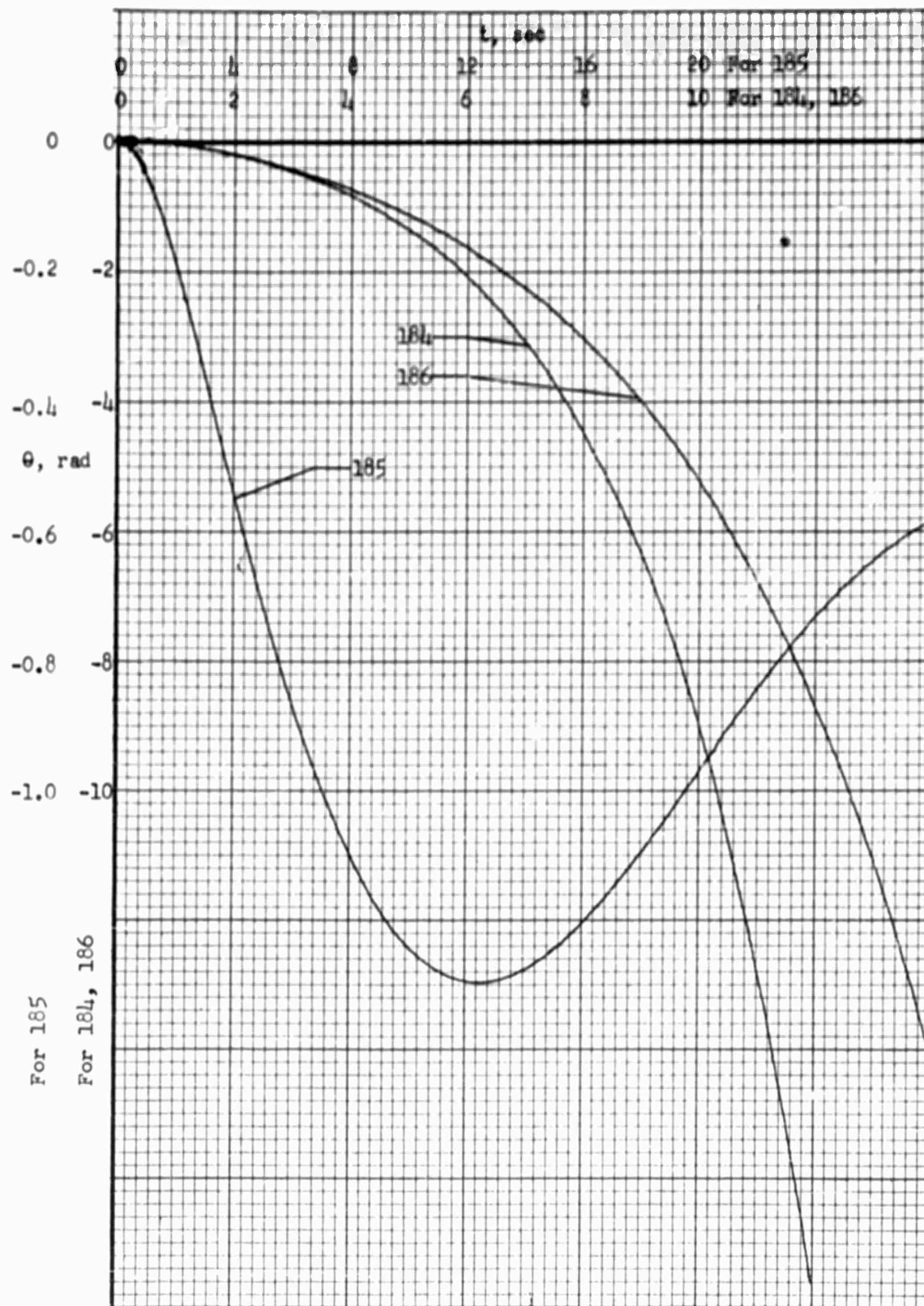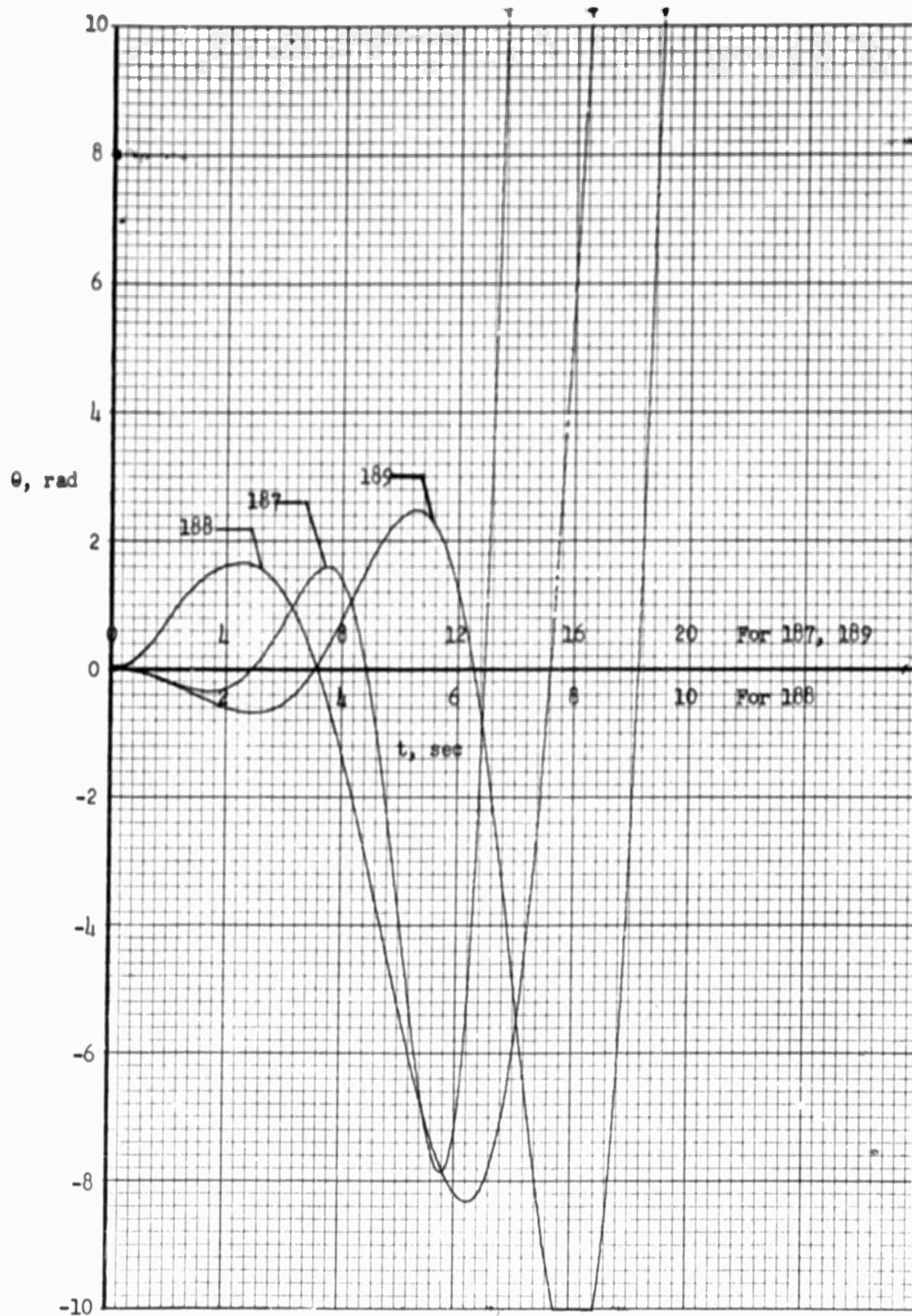FIGURE 46: PITCH ANGLE RESPONSE TO CONTROL MOMENT STEP INPUT
FOR CASE NOS. 71, 85, 87
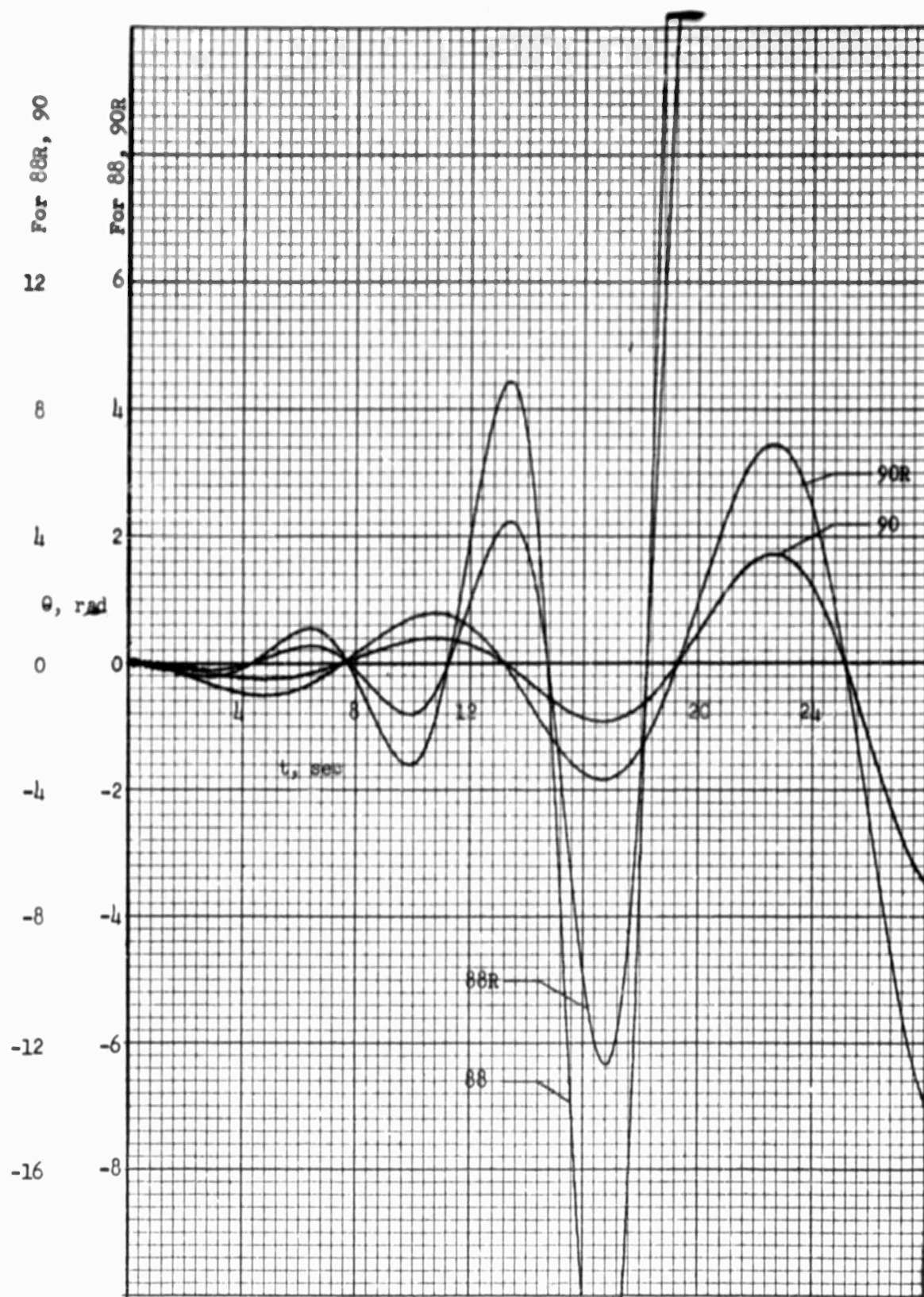
FIGURE 47: PITCH ANGLE RESPONSE TO CONTROL MOMENT STEP INPUT
FOR CASE NOS. 88R, 90R
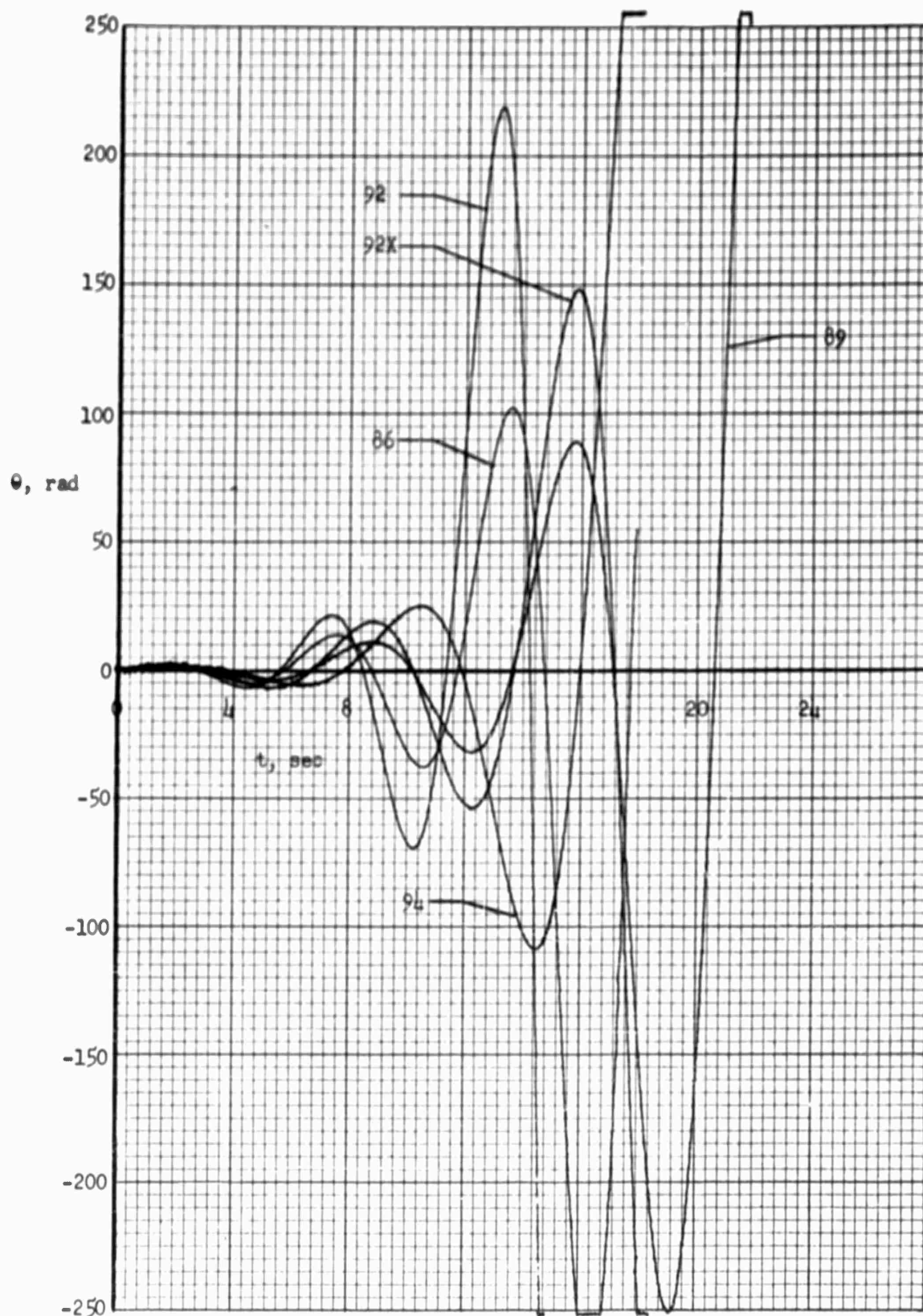
FIGURE 48: PITCH ANGLE RESPONSE TO HORIZONTAL GUST PULSE INPUT
FOR CASE NOS. 86, 89, 92, 94
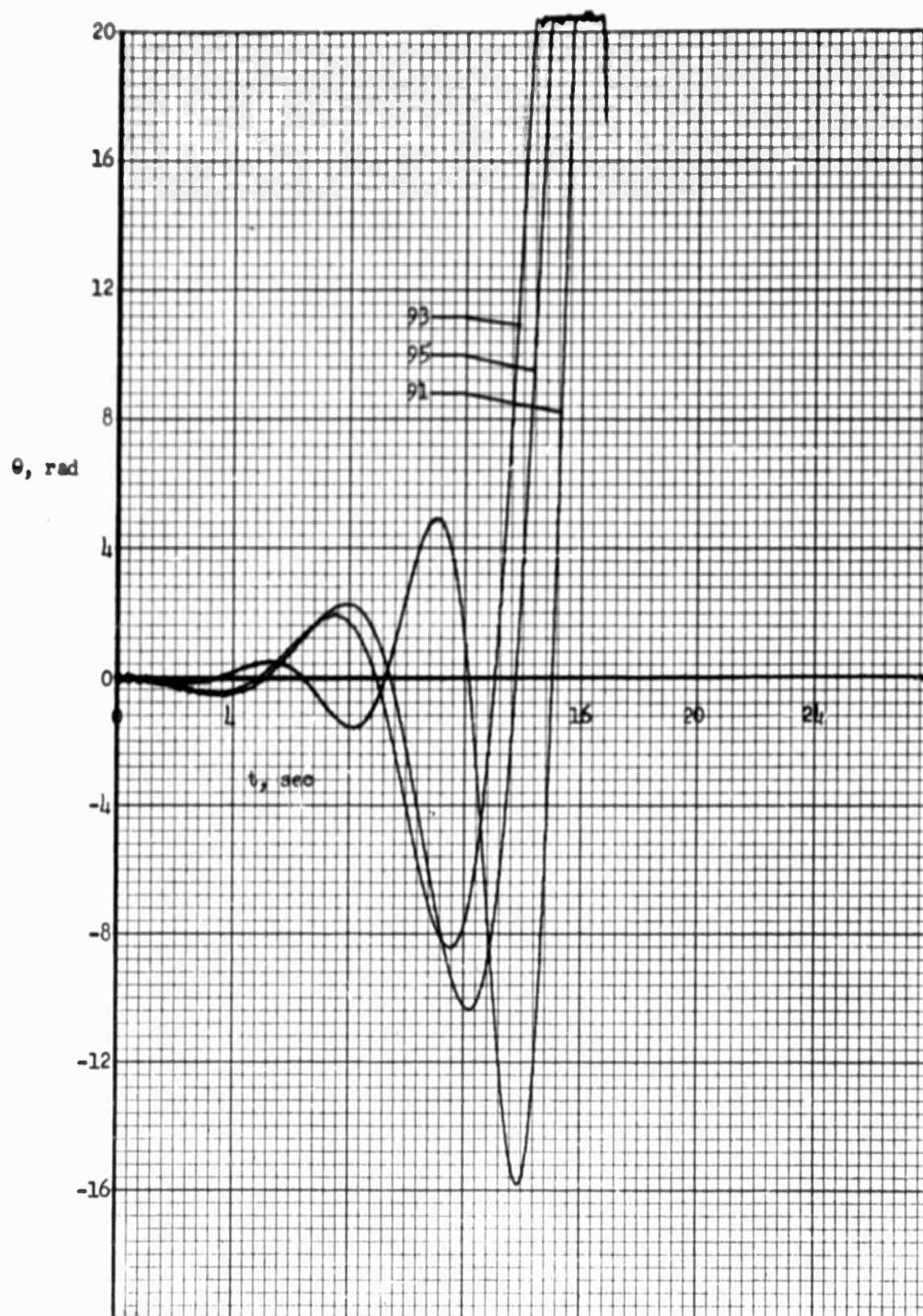
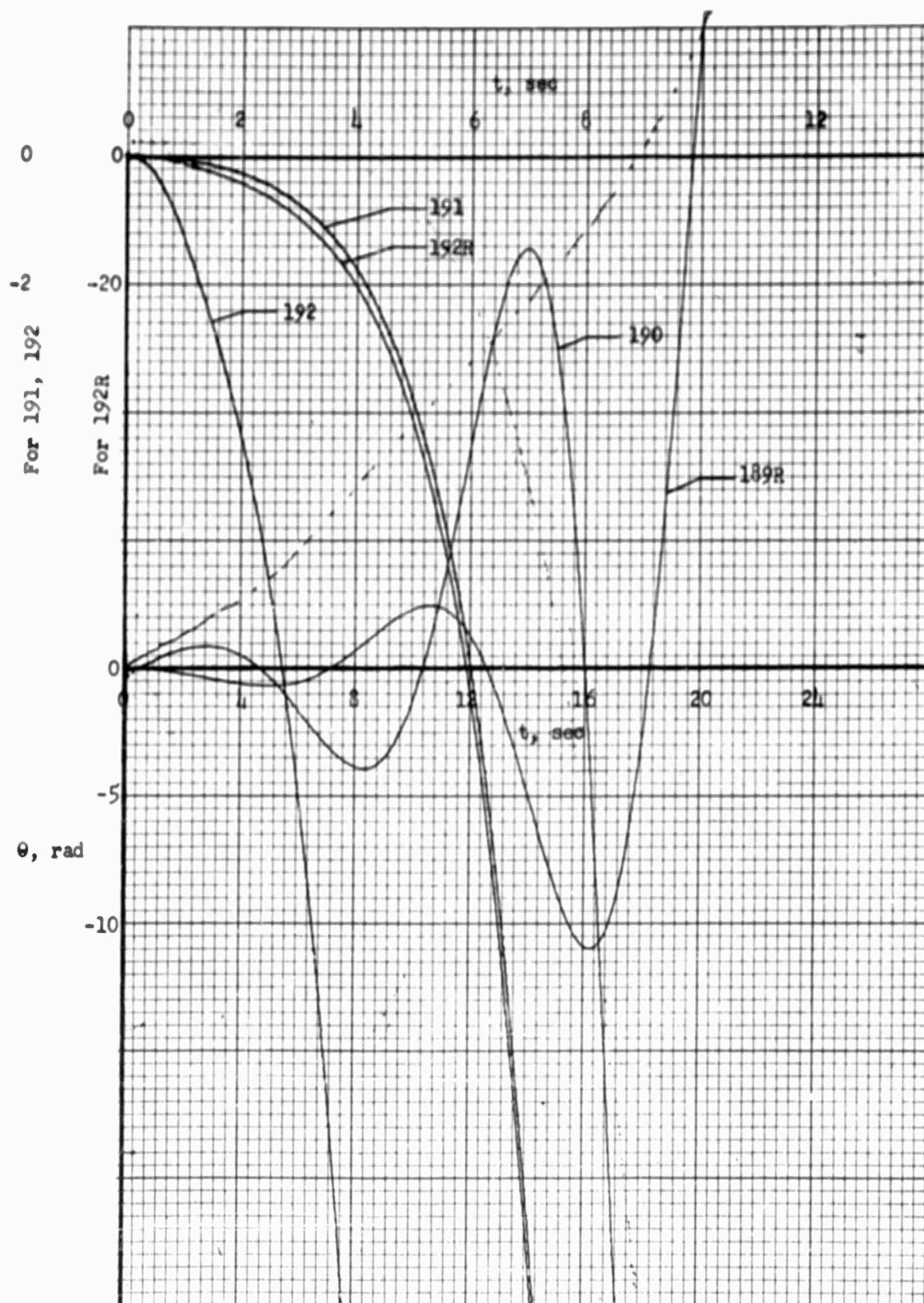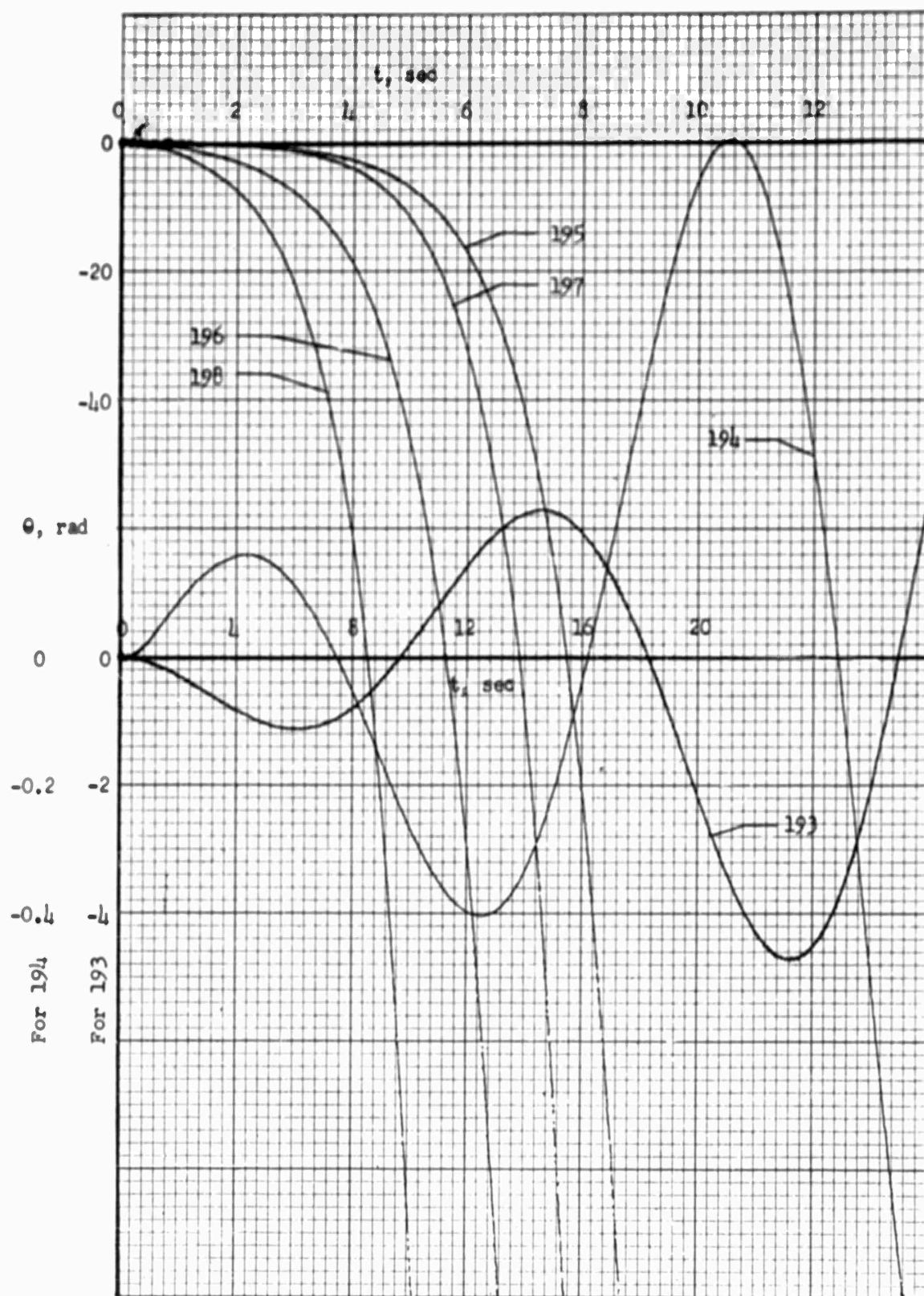FIGURE 49: PITCH ANGLE RESPONSE TO CONTROL MOMENT STEP INPUT
FOR CASE NOS. 91, 93, 95
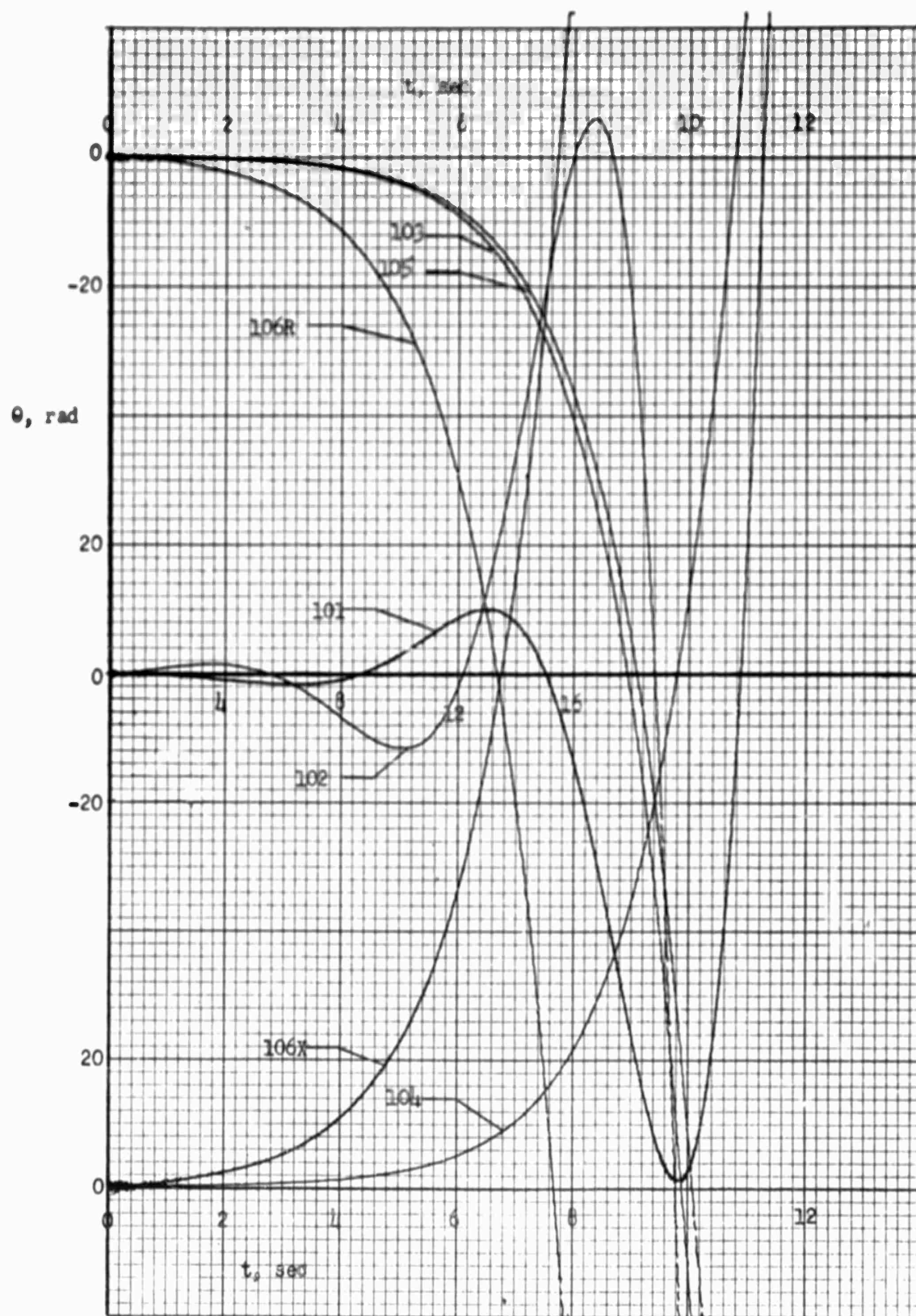
FIGURE 50: PITCH ANGLE RESPONSE TO CONTROL MOMENT STEP INPUT
FOR CASE NOS. 101, 103, 105 AND TO HORIZONTAL GUST
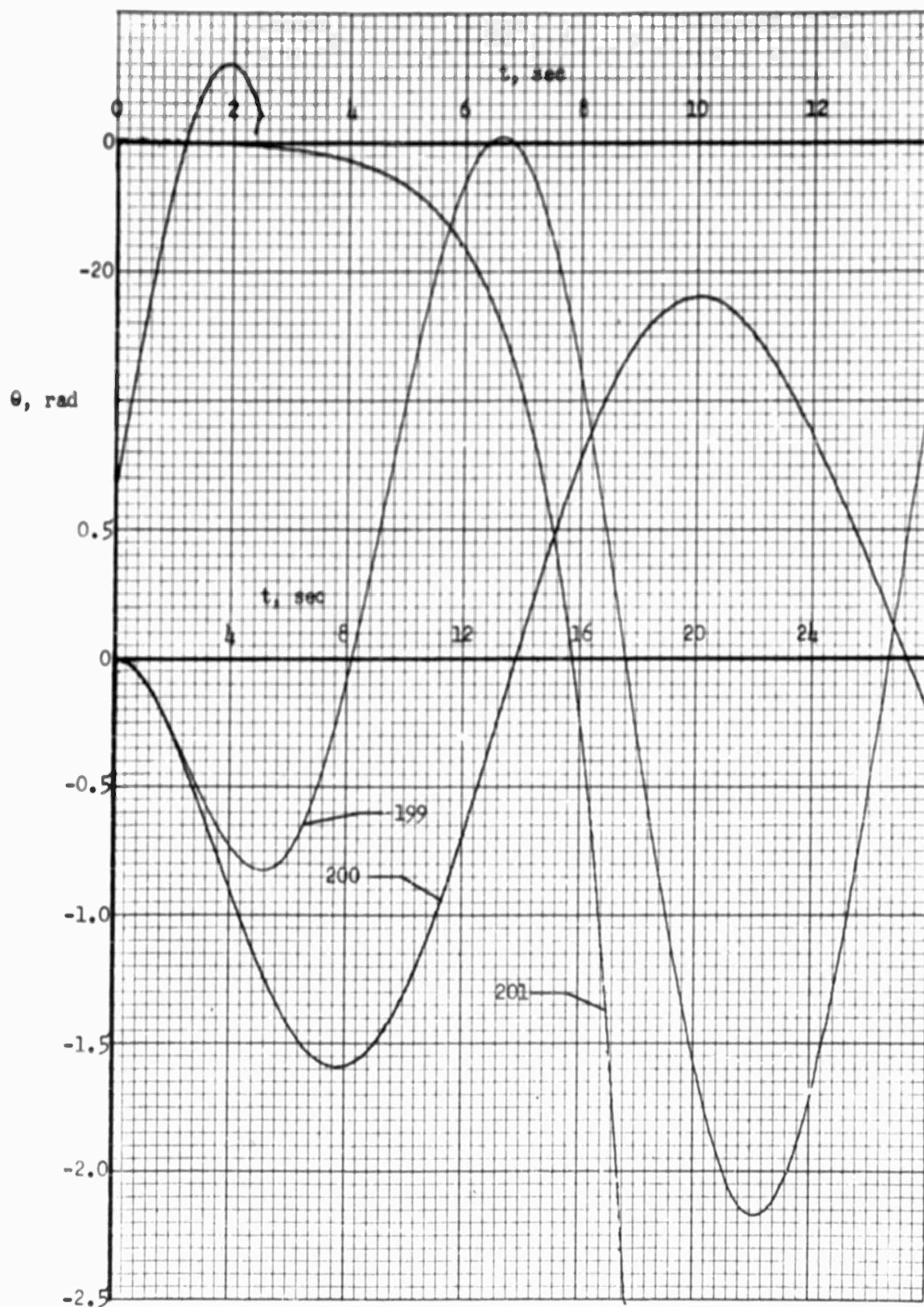PULSE INPUT FOR CASE NOS. 102, 104, 106R
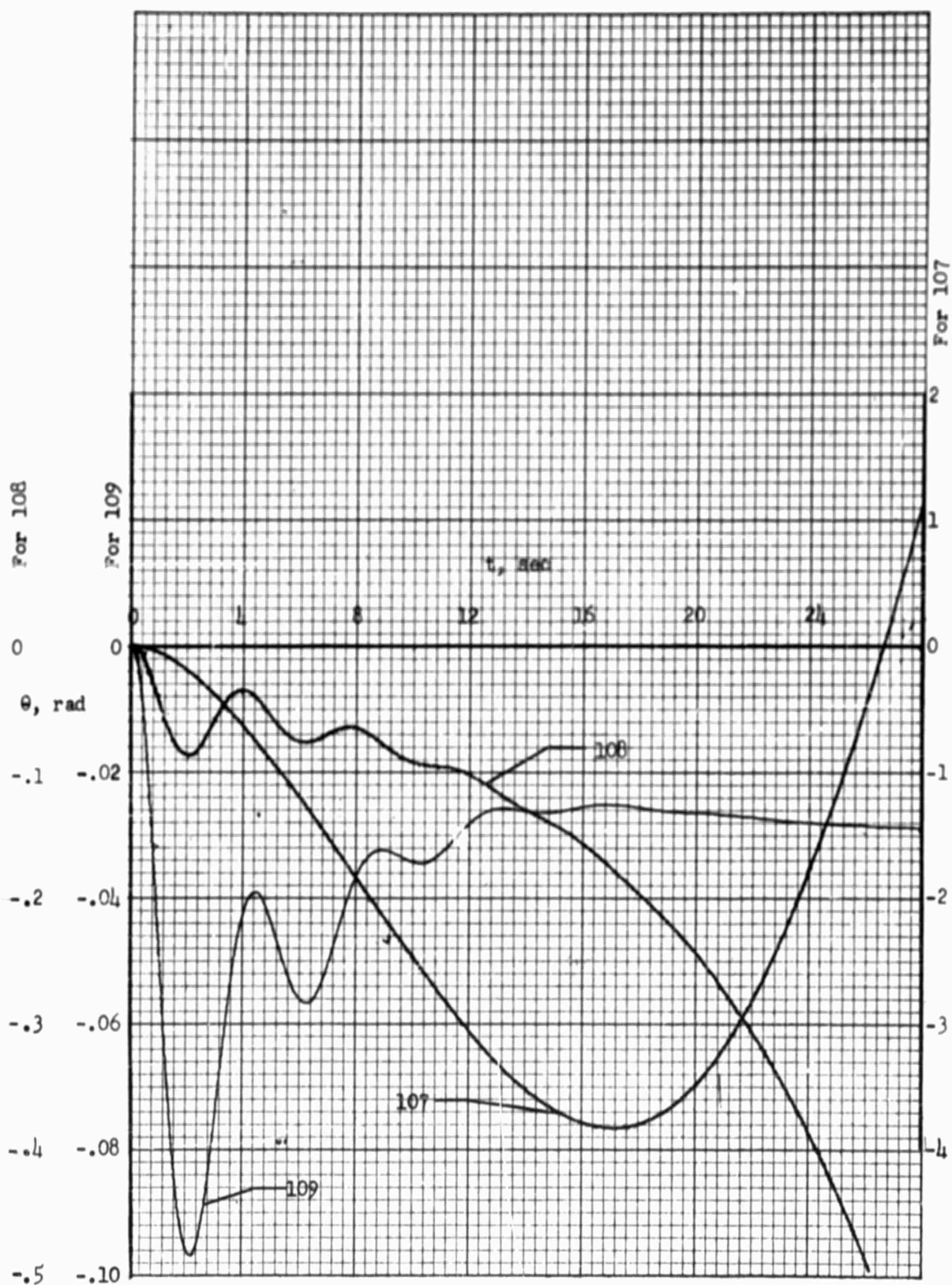
FIGURE 51: PITCH ANGLE RESPONSE TO CONTROL MOMENT STEP INPUT
FOR CASE NOS. 107, 108, 109

FIGURE 52: PITCH ANGLE RESPONSE TO CONTROL MOMENT STEP INPUT
FOR CASE NOS. 110, 111, 112
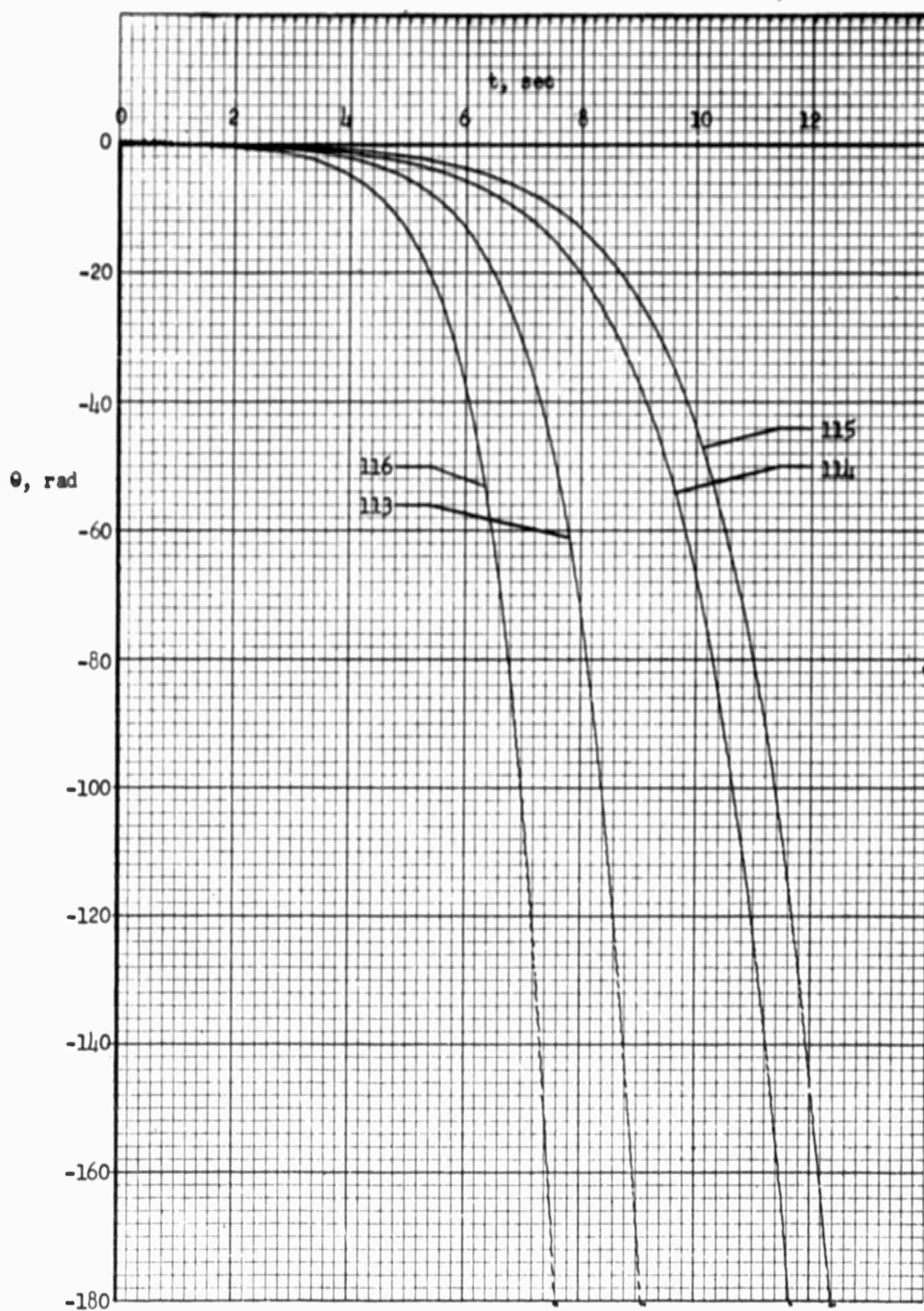
FIGURE 53: PITCH ANGLE RESPONSE TO CONTROL MOMENT STEP INPUT
FOR CASE NOS. 113, 114, 115, 116
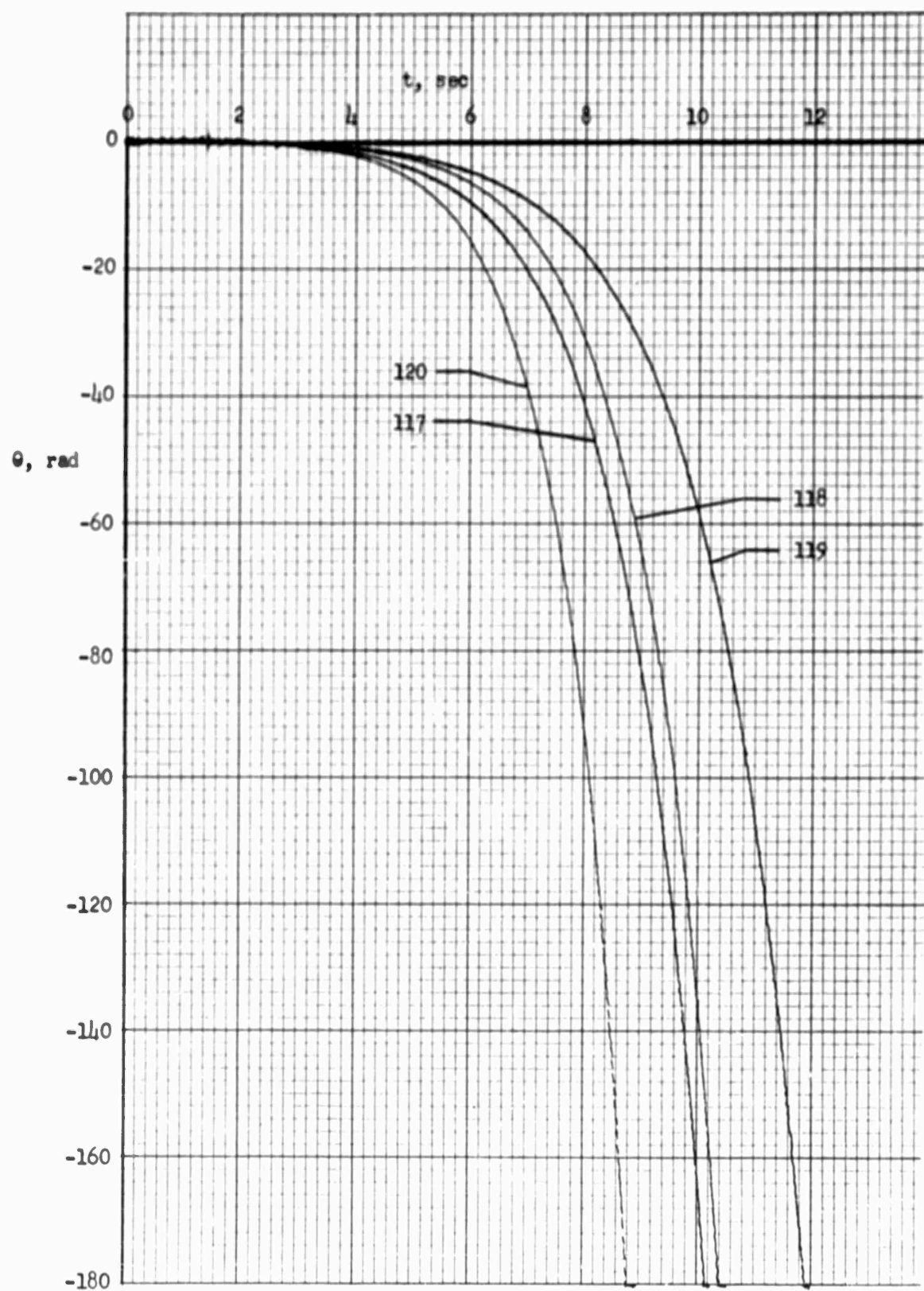
FIGURE 54: PITCH ANGLE RESPONSE TO CONTROL MOMENT STEP INPUT
FOR CASE NOS. 117, 118, 119, 120
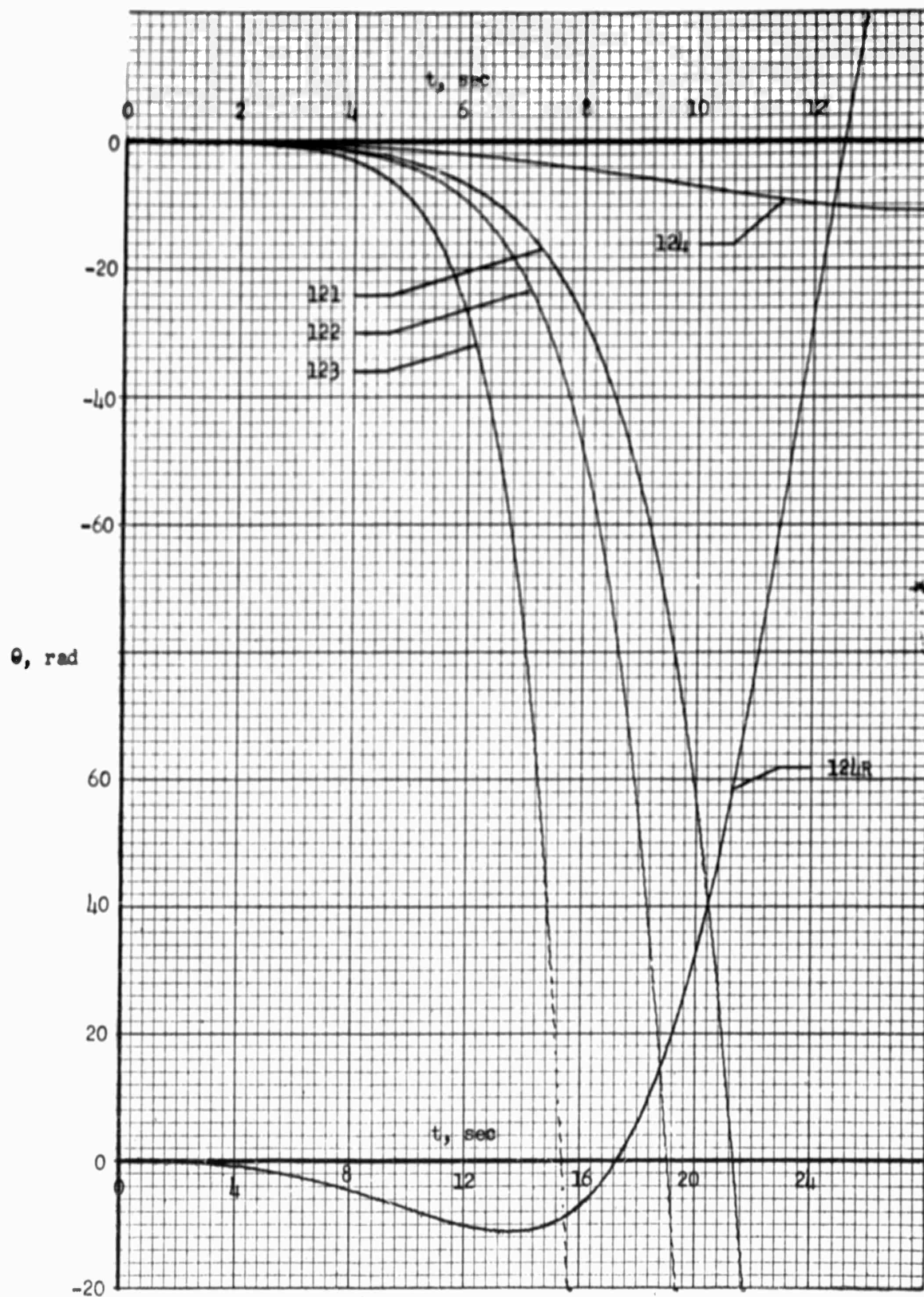
FIGURE 55: PITCH ANGLE RESPONSE TO CONTROL MOMENT STEP INPUT
FOR CASE NOS. 121, 122, 123, 124R
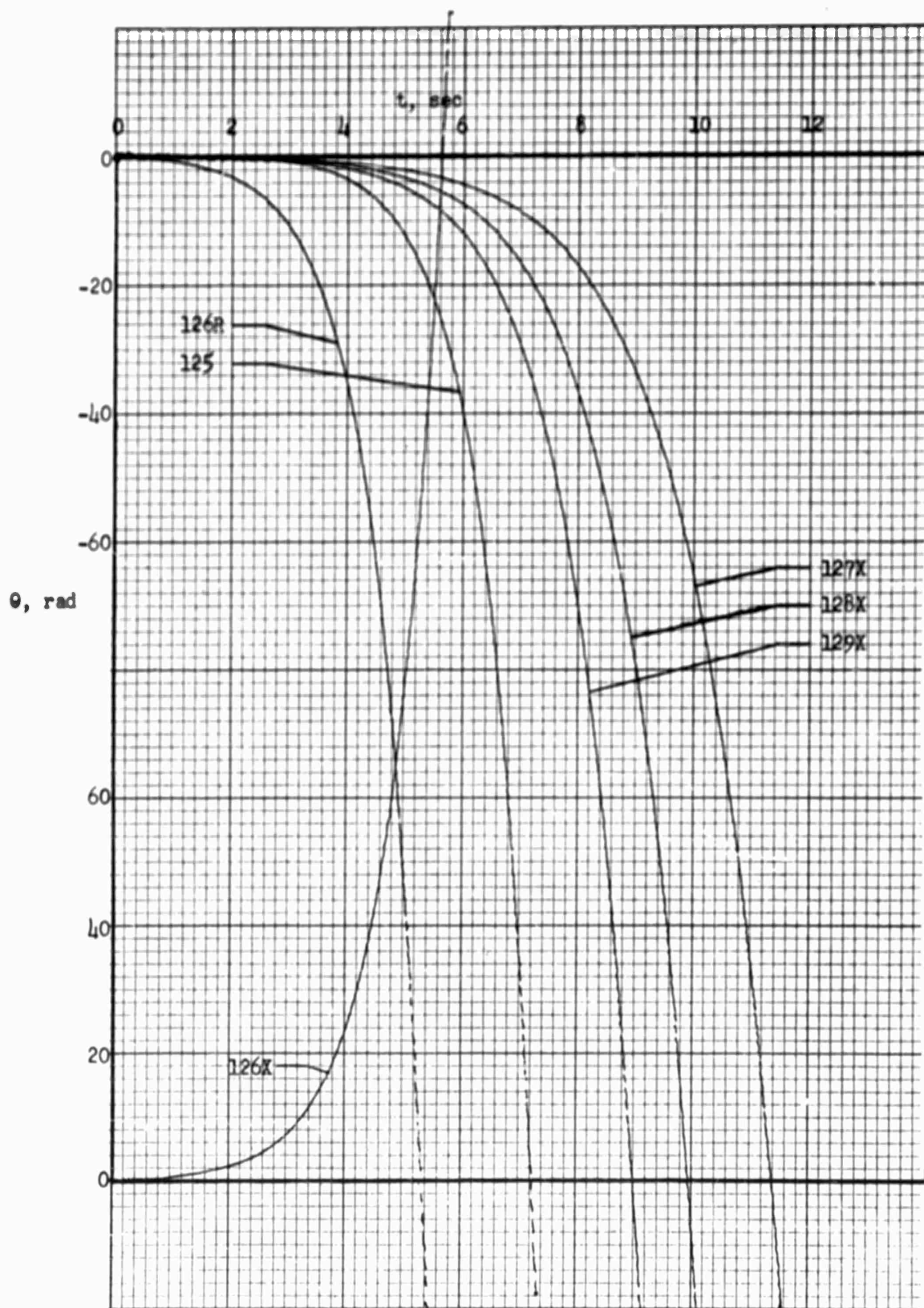
FIGURE 56: PITCH ANGLE RESPONSE TO CONTROL MOMENT STEP INPUT
FOR CASE NO. 125 AND TO HORIZONTAL GUST PULSE INPUT
FOR CASE NO. 126R

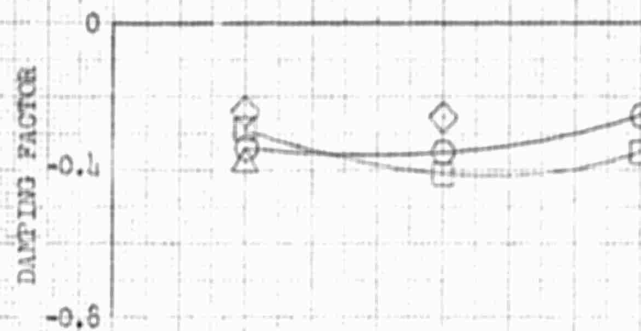FIGURE 57: PITCH ANGLE RESPONSE TO CONTROL MOMENT STEP INPUT FOR CASE NOS. 127, 128, 129

FIGURE 58: PITCH ANGLE RESPONSE TO CONTROL MOMENT STEP INPUT
FOR CASE NOS. 130, 131, 132

FIGURE 59: PITCH ANGLE RESPONSE TO CONTROL MOMENT STEP INPUT
FOR CASE NOS. 133, 134, 135

FIGURE 60 : PITCH ANGLE RESPONSE TO CONTROL MOMENT STEP INPUT
FOR CASE NOS. 136, 137, 138

FIGURE 61: PITCH ANGLE RESPONSE TO CONTROL MOMENT STEP INPUT
FOR CASE NOS. 139, 141, 143 AND TO HORIZONTAL GUST
PULSE INPUT FOR CASE NOS. 140, 142R, 144R

FIGURE 62: PITCH ANGLE RESPONSE TO CONTROL MOMENT STEP INPUT
FOR CASE NOS. 145, 146, 147

For 148, 150R, 151, 152, 153

For 148R, 149, 150

FIGURE 63: PITCH ANGLE RESPONSE TO CONTROL MOMENT STEP INPUT FOR CASE NOS. 148R, 150R, 152 AND TO HORIZONTAL GUST PULSE INPUT FOR CASE NOS. 149, 151, 153

FIGURE 64: PITCH ANGLE RESPONSE TO CONTROL MOMENT STEP INPUT
FOR CASE NOS. 154, 155R, 156

FIGURE 65: PITCH ANGLE RESPONSE TO CONTROL MOMENT STEP INPUT
FOR CASE NOS. 157, 158, 159, 160, 161, 162

FIGURE 66: PITCH ANGLE RESPONSE TO CONTROL MOMENT STEP INPUT
FOR CASE NOS 163, 164, 165, 166, 167, 168

FIGURE 67: PITCH ANGLE RESPONSE TO CONTROL MOMENT STEP INPUT
FOR CASE NOS. 169, 171, 173 AND TO HORIZONTAL GUST
PULSE INPUT FOR CASE NOS. 170, 172, 174

FIGURE 68 : PITCH ANGLE RESPONSE TO CONTROL MOMENT STEP INPUT
FOR CASE NOS. 175, 176, 177

FIGURE 69: PITCH ANGLE RESPONSE TO CONTROL MOMENT STEP INPUT FOR CASE NOS. 178, 180, 182 AND TO HORIZONTAL GUST PULSE INPUT FOR CASE NOS. 179, 181R, 183

FIGURE 70: PITCH ANGLE RESPONSE TO CONTROL MOMENT STEP INPUT
FOR CASE NOS. 184, 185, 186

FIGURE 71: PITCH ANGLE RESPONSE TO CONTROL MOMENT STEP INPUT
FOR CASE NO. 187 AND TO HORIZONTAL GUST PULSE INPUT
FOR CASE NO. 188

FIGURE 72: PITCH ANGLE RESPONSE TO CONTROL MOMENT STEP INPUT
FOR CASE NOS. 189R, 191 AND TO HORIZONTAL GUST PULSE
INPUT FOR CASE NOS. 190, 192R

FIGURE 73: PITCH ANGLE RESPONSE TO CONTROL MOMENT STEP INPUT
FOR CASE NOS. 193, 195, 197 AND TO HORIZONTAL GUST
PULSE INPUT FOR CASE NOS. 194, 196, 198

FIGURE 74: PITCH ANGLE RESPONSE TO CONTROL MOMENT STEP INPUT
FOR CASE NOS. 199, 200, 201
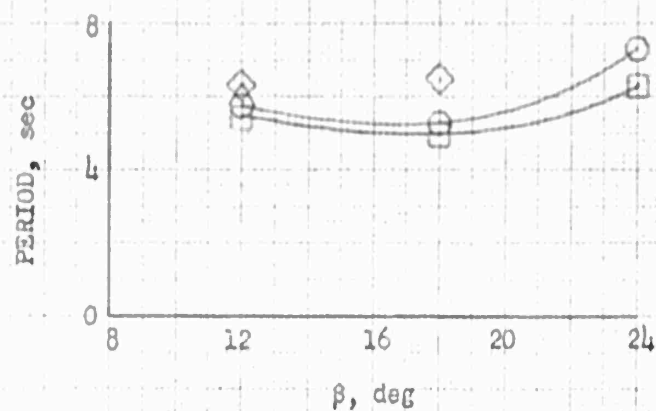
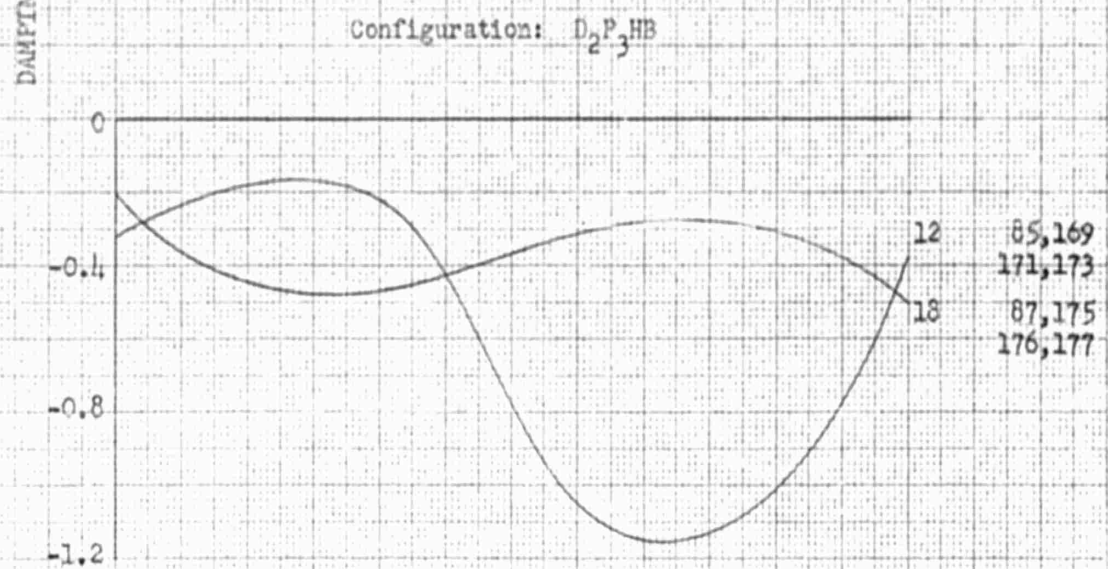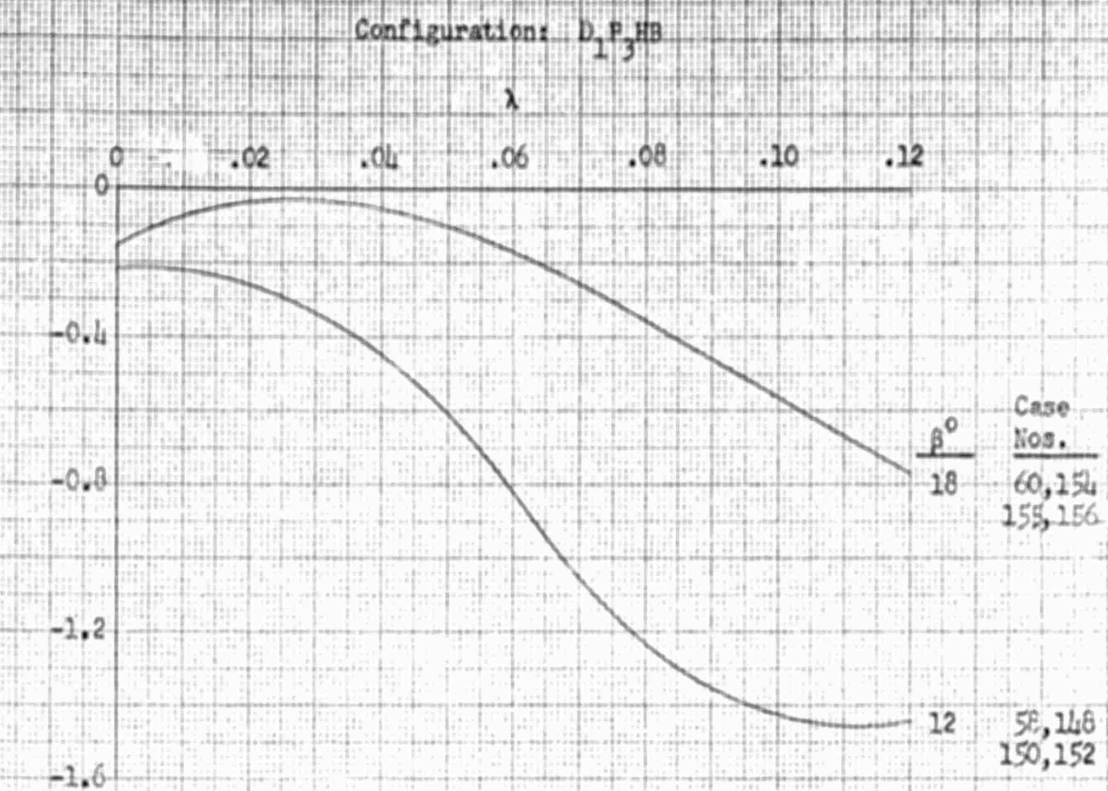FIGURE 75: HOVERING DAMPING FACTOR AND PERIOD OF
OSCILLATION VS PITCH SETTING (DUCT 3)
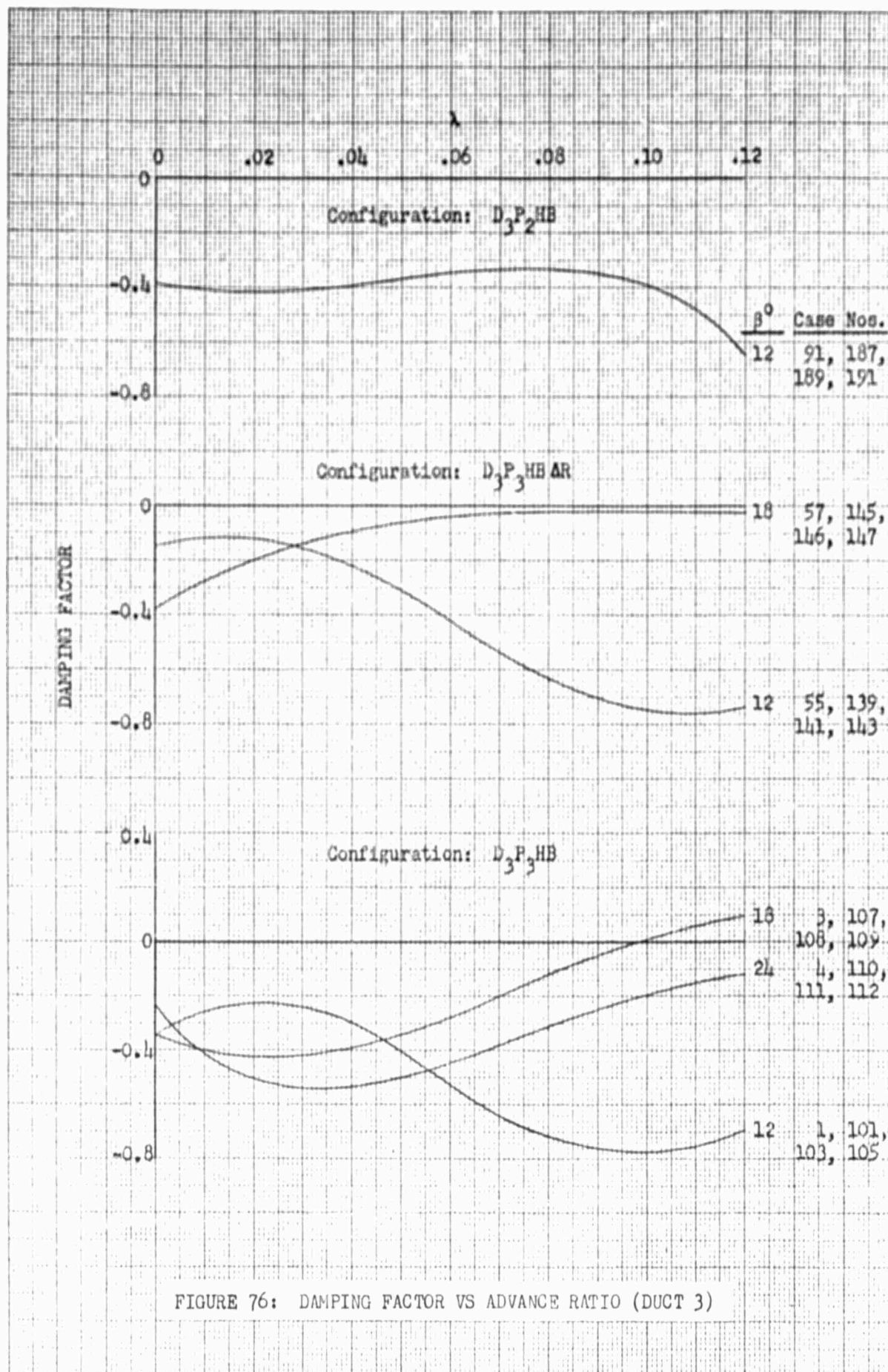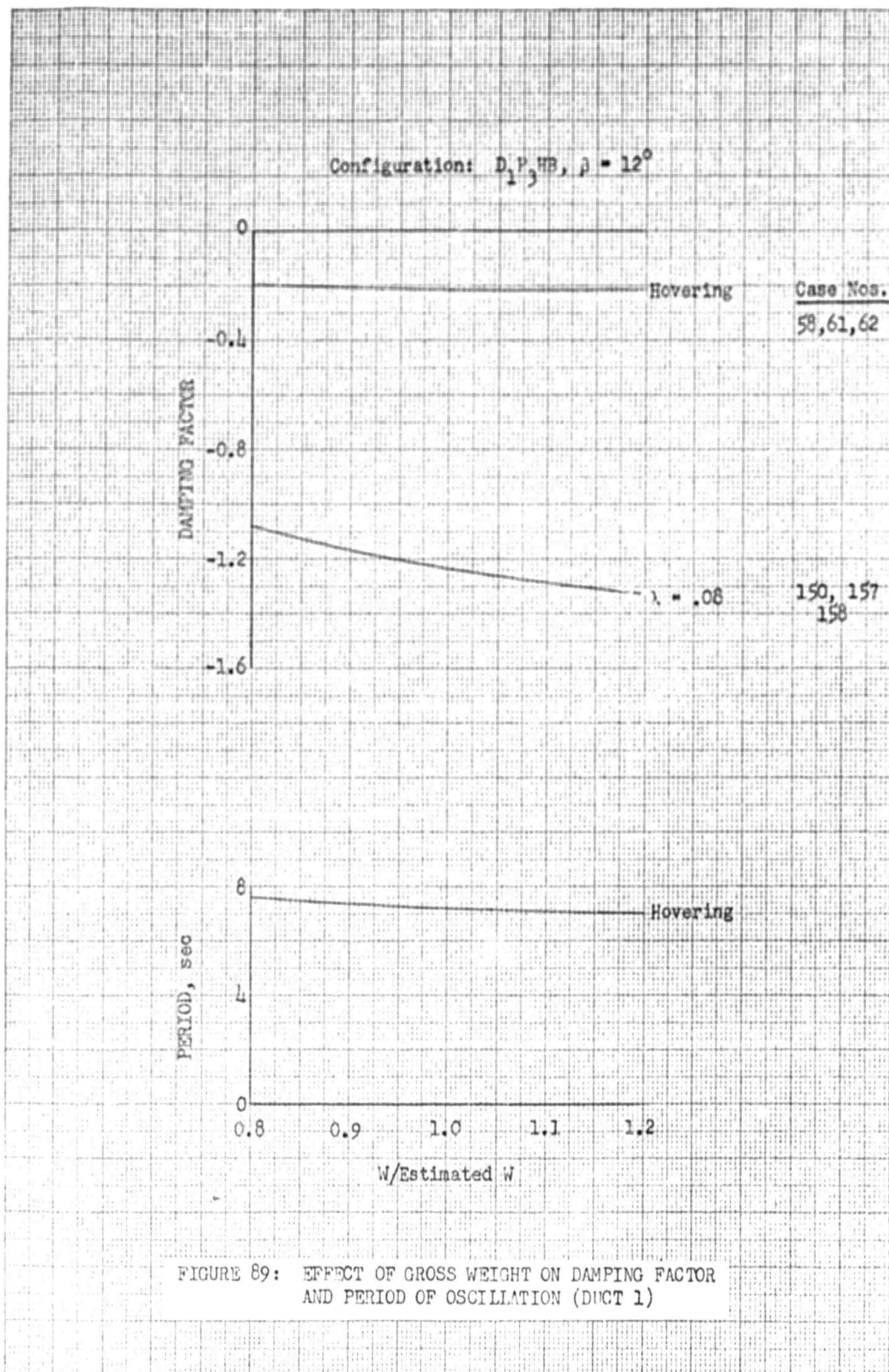
FIGURE 76: DAMPING FACTOR VS ADVANCE RATIO (DUCT 3)
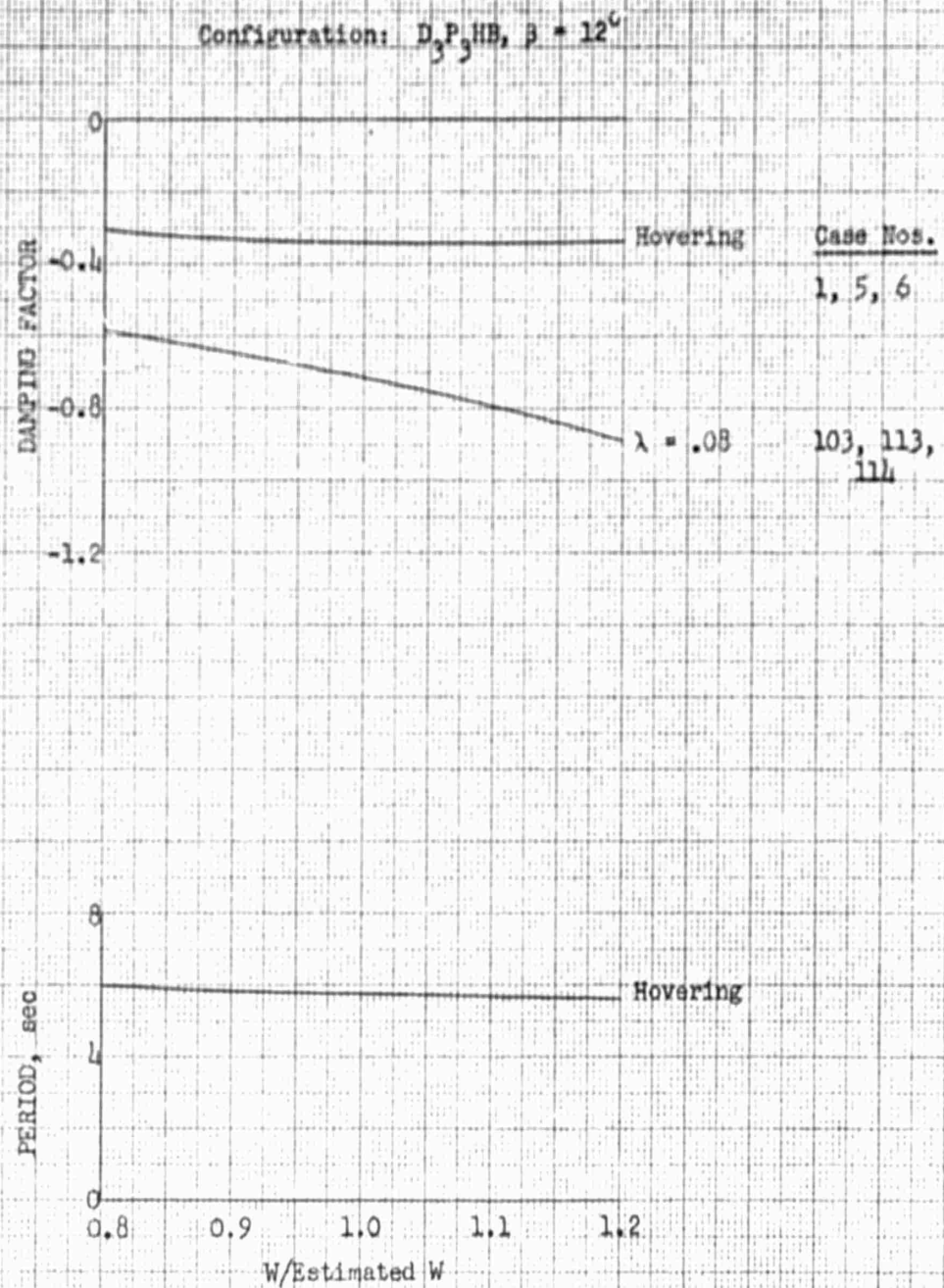
FIGURE 77: EFFECT OF GROSS WEIGHT ON DAMPING FACTOR
AND PERIOD OF OSCILLATION (DUCT 3)
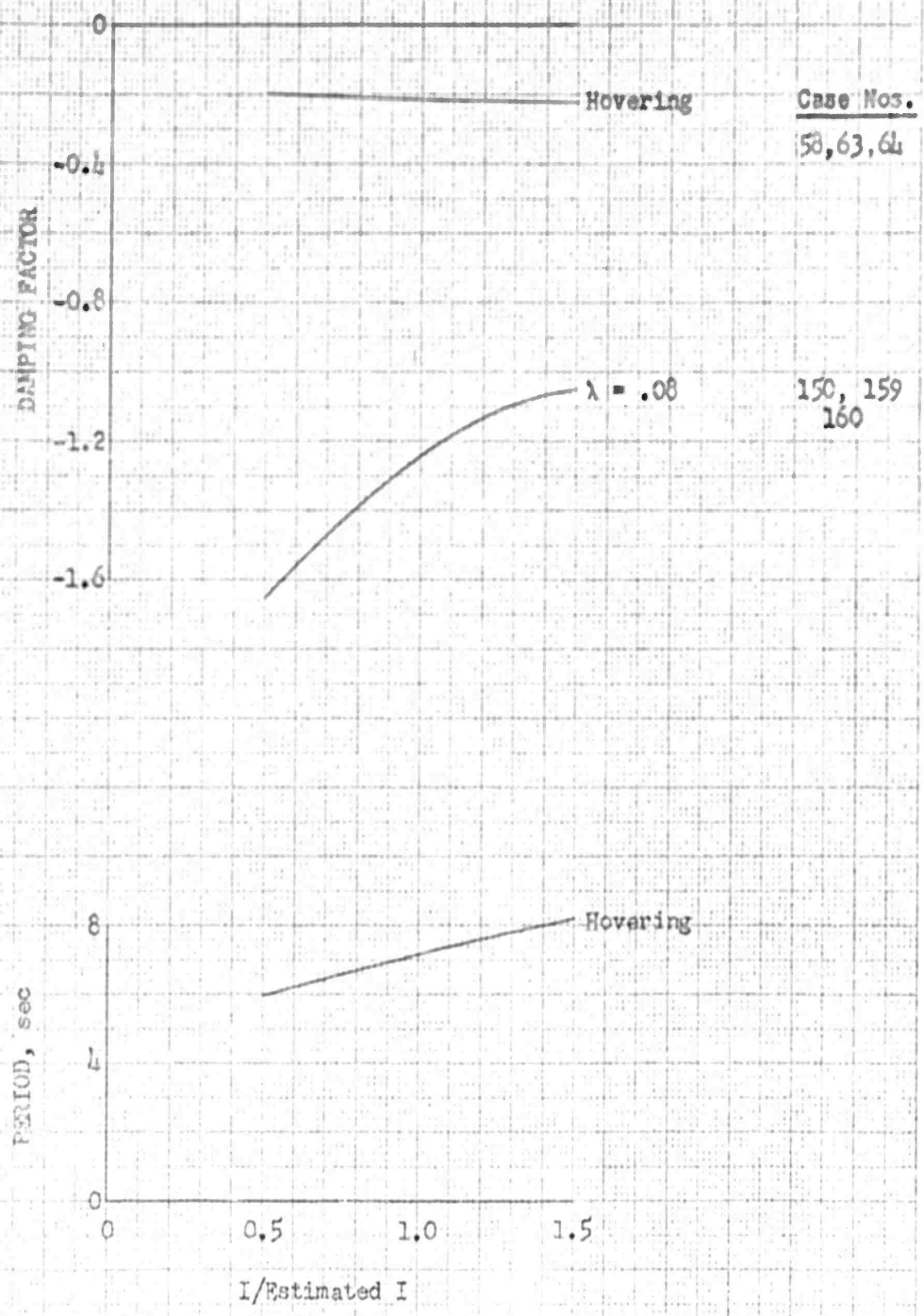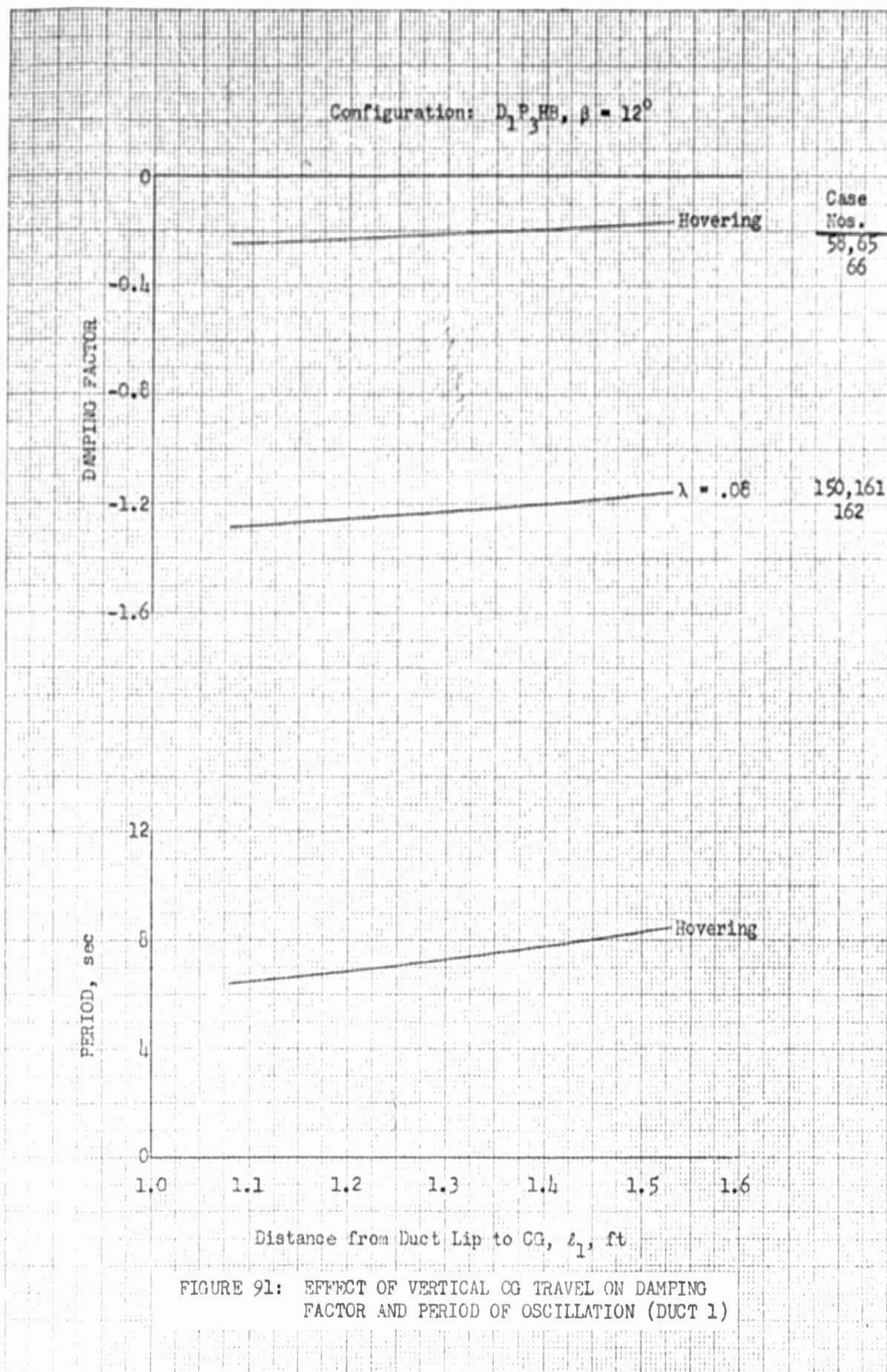
Configuration: D_3P_3HB, $\beta = 12°$
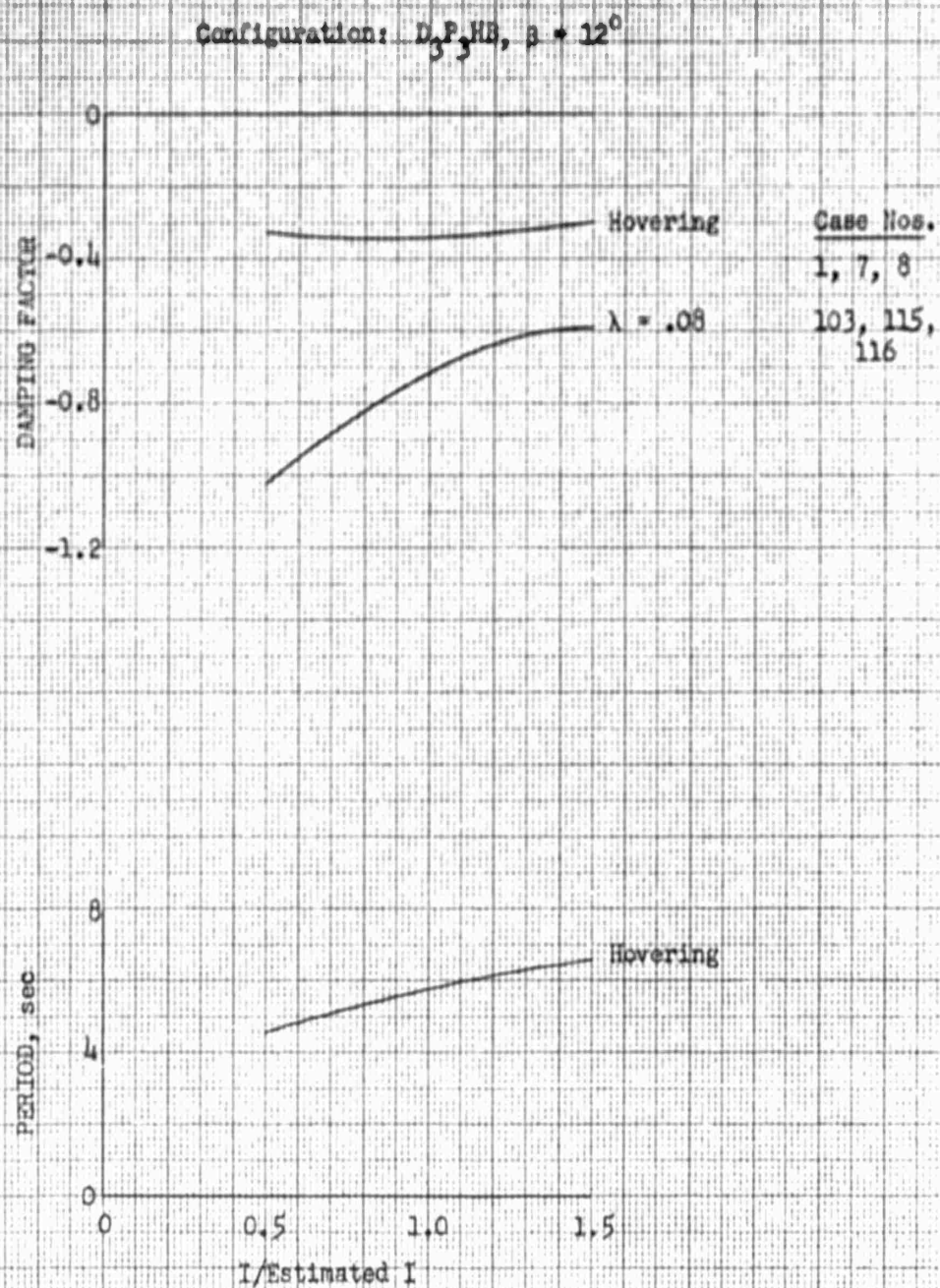
FIGURE 78:   EFFECT OF MOMENT OF INERTIA ON DAMPING
FACTOR AND PERIOD OF OSCILLATION (DUCT 3)
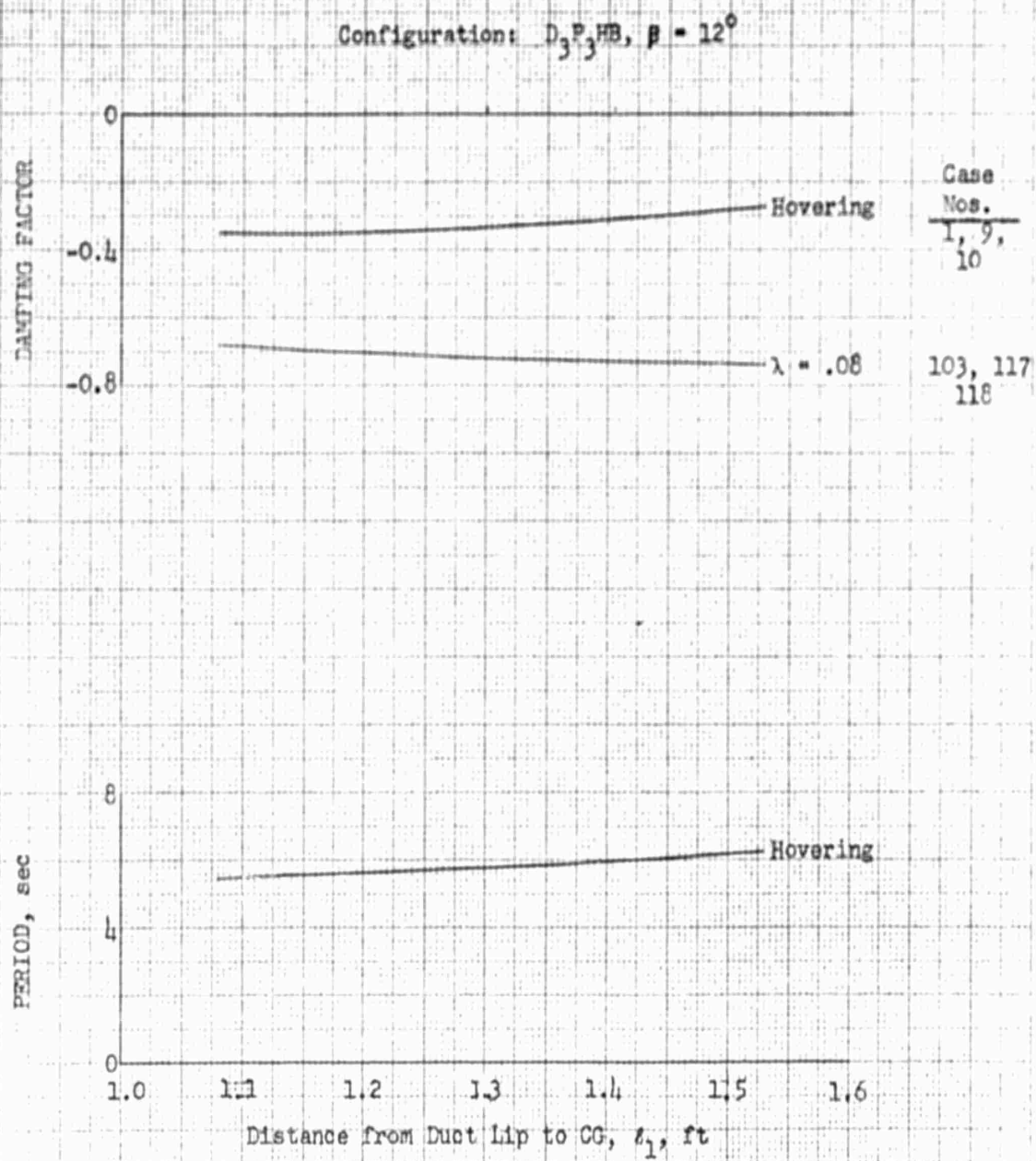
FIGURE 79: EFFECT OF VERTICAL CG TRAVEL ON DAMPING
FACTOR AND PERIOD OF OSCILLATION (DUCT 3)

Configuration: D_3P_3HB, $\beta = 12°$
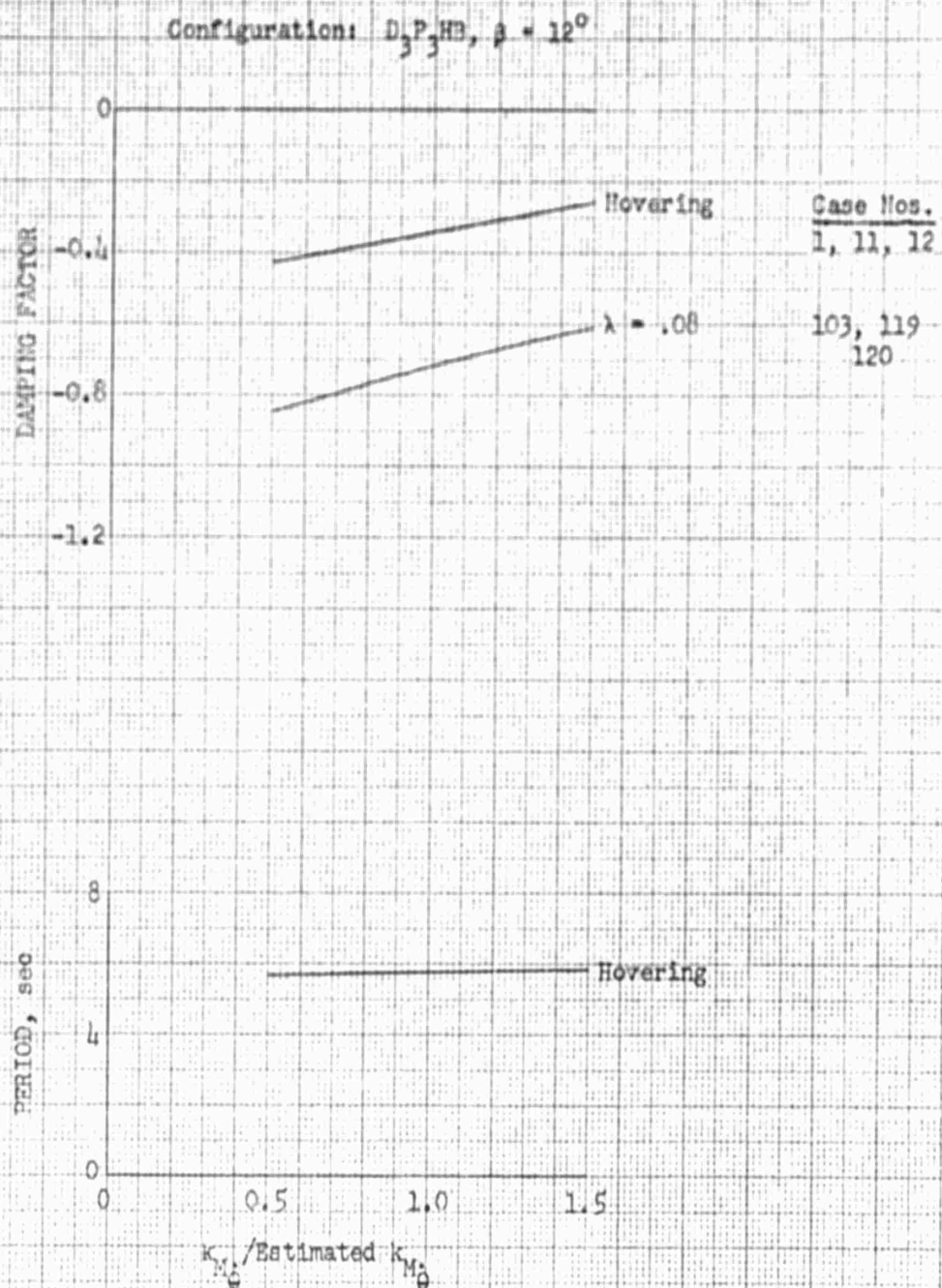
FIGURE 80: EFFECT OF DAMPING IN PITCH ON DAMPING
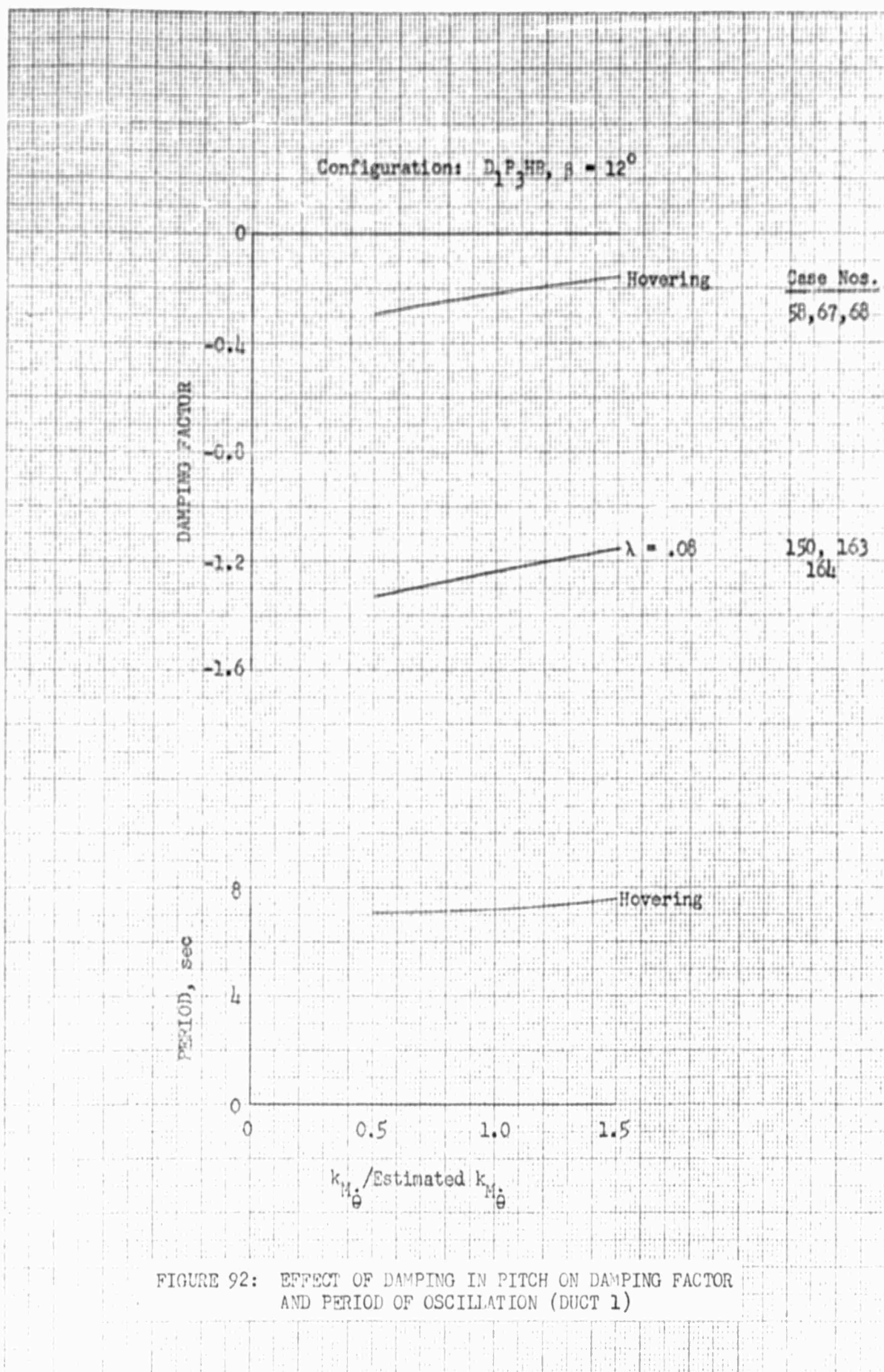FACTOR AND PERIOD OF OSCILLATION (DUCT 3)

Configuration: $D_3 F_3 WB$, $\beta = 12°$
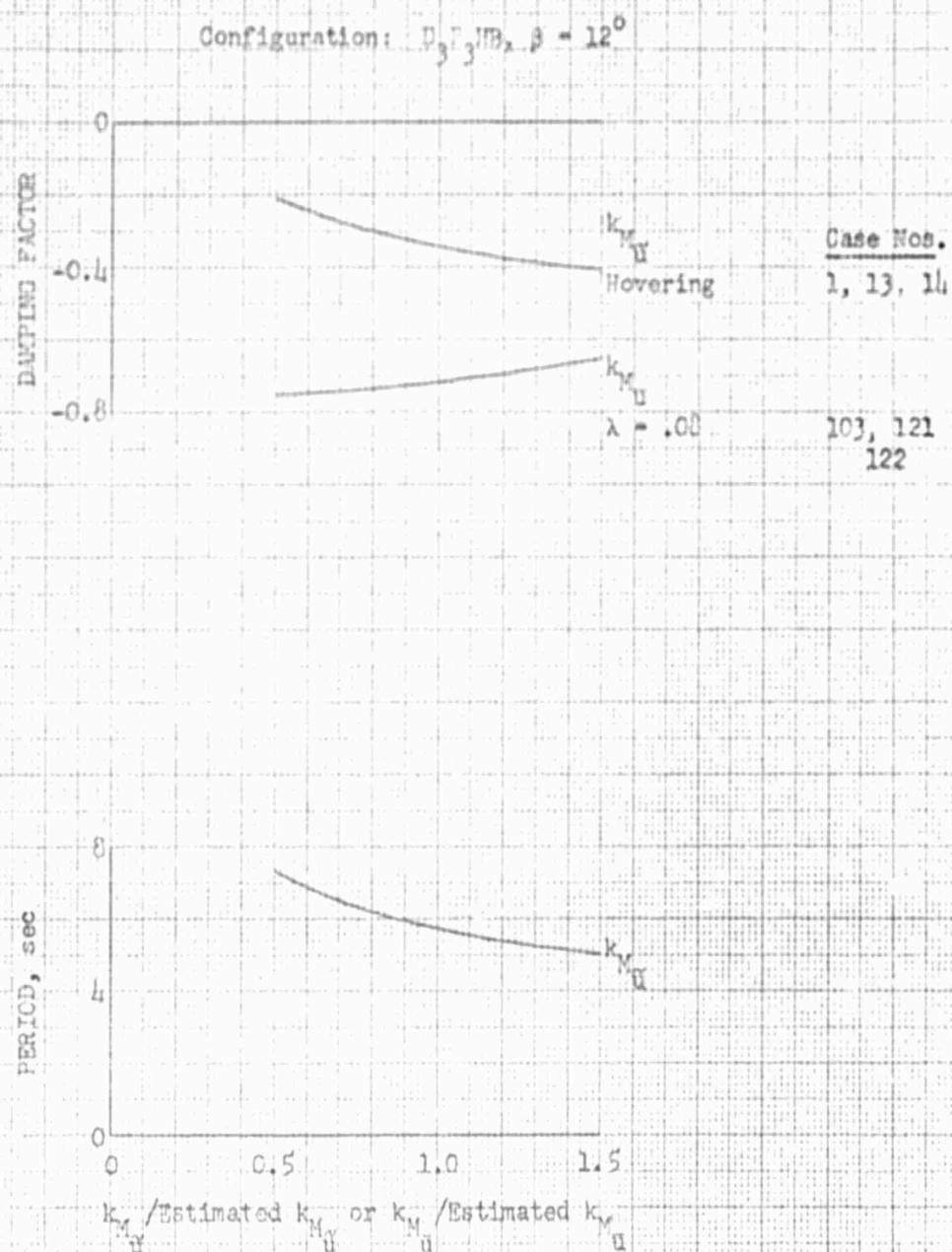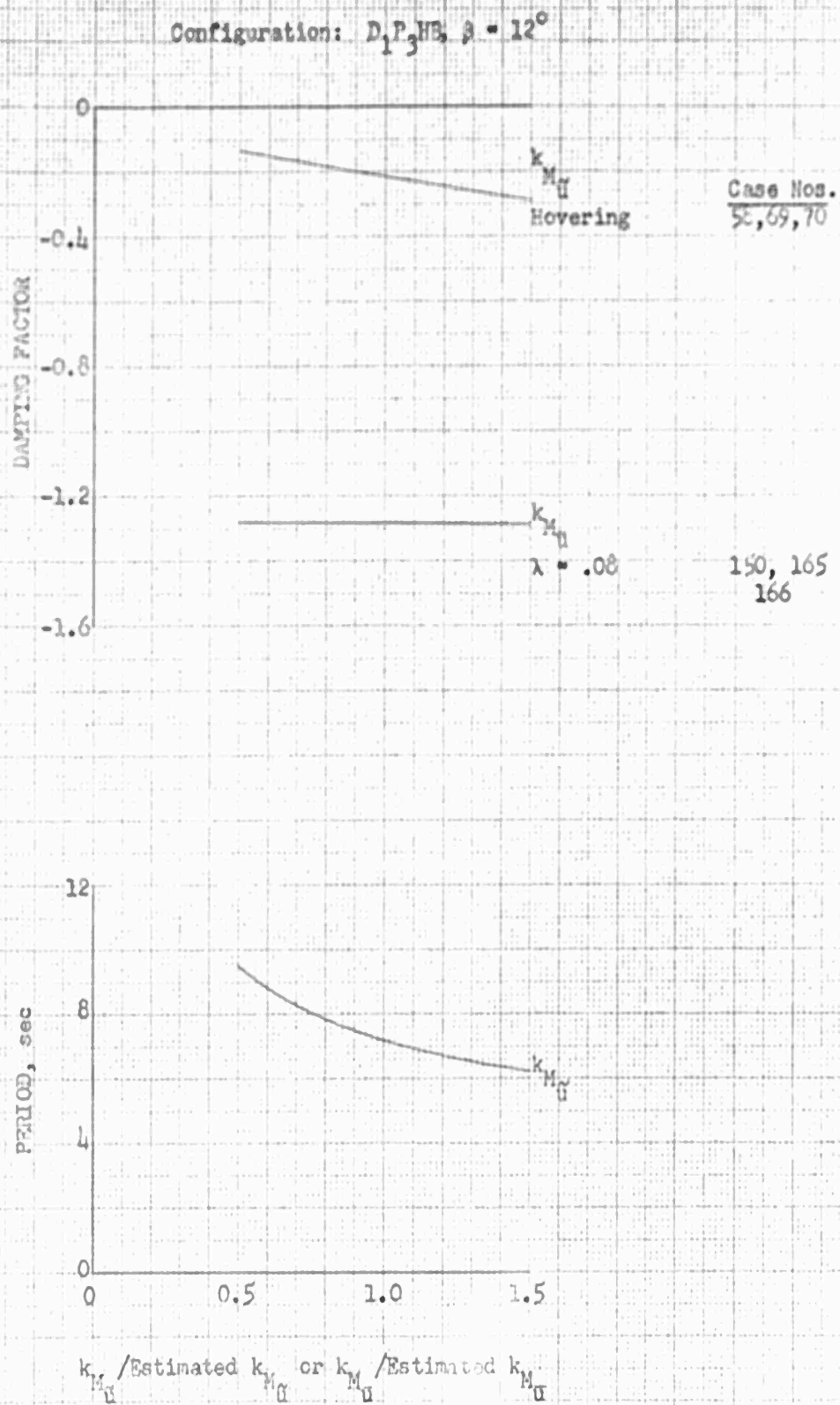

FIGURE 81: EFFECT OF SPEED STABILITY ON DAMPING
FACTOR AND PERIOD OF OSCILLATION (DUCT 3)

Configuration: D_3P_3HB, $\beta = 12°$

k_{M_W}/Estimated k_{M_W}
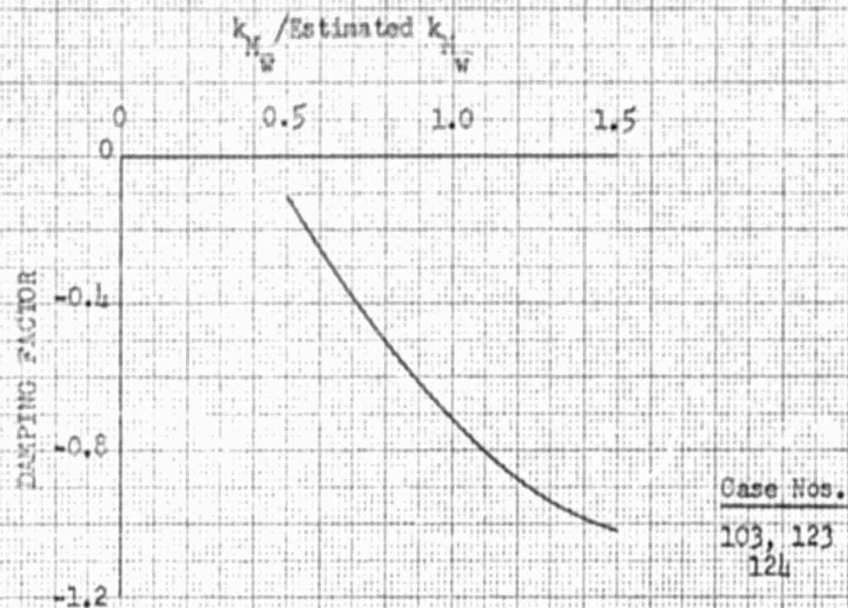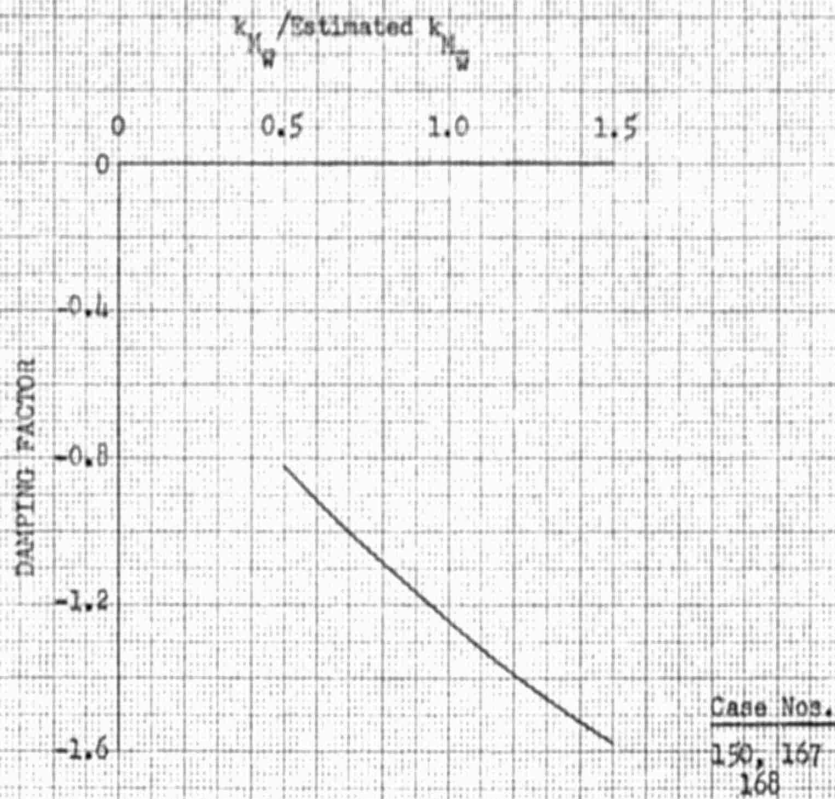
Case Nos.
103, 123
124

FIGURE 82: EFFECT OF ANGLE-OF-ATTACK STABILITY
ON DAMPING FACTOR AT $\lambda = .08$ (DUCT 3)

FIGURE 83: EFFECT OF GYROBAR STABILIZER ON DAMPING FACTOR, PERIOD OF OSCILLATION AND OVERSHOOT IN HOVERING WITH $\beta = 12^{\circ}$ (DUCT 3)
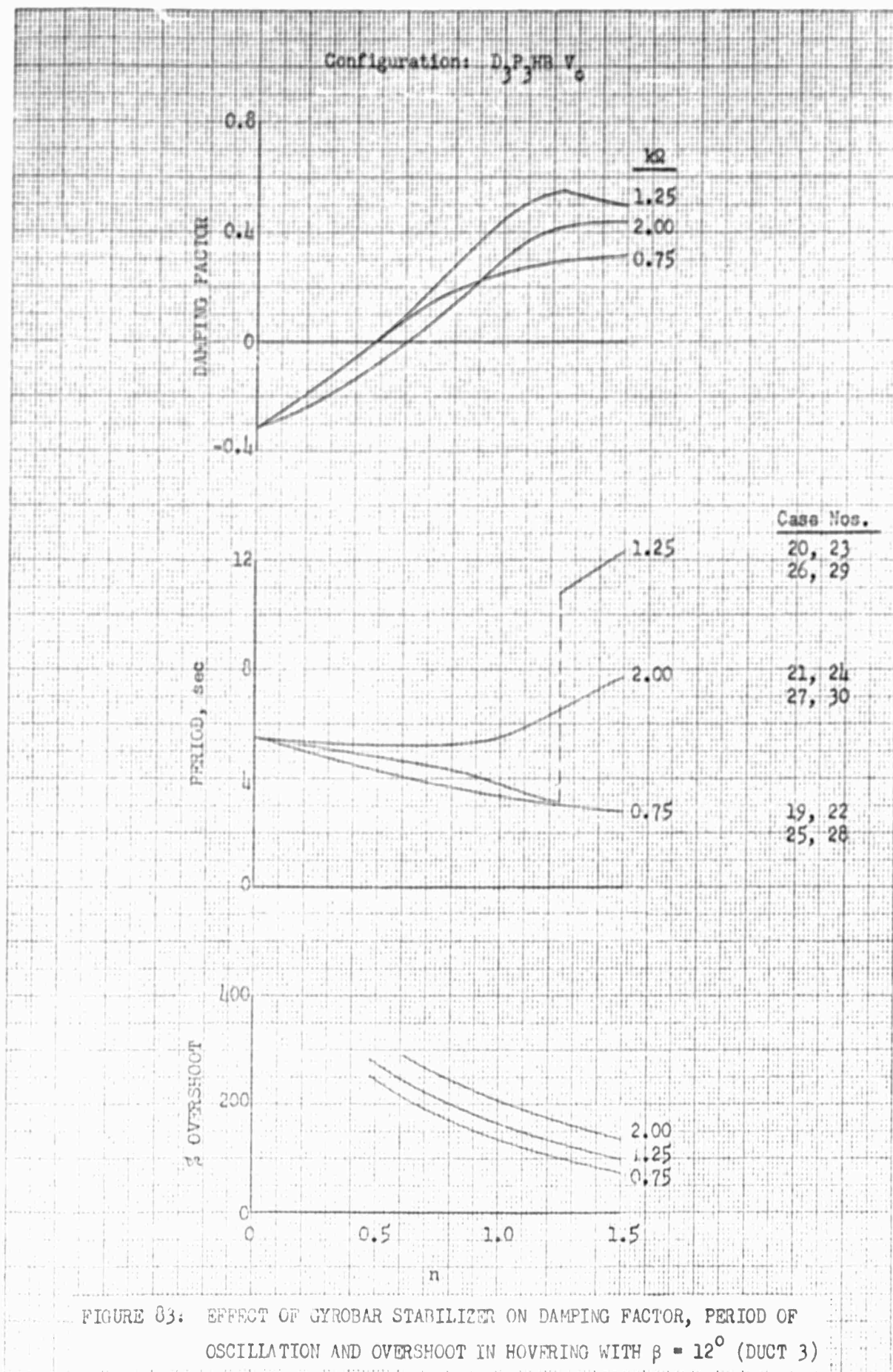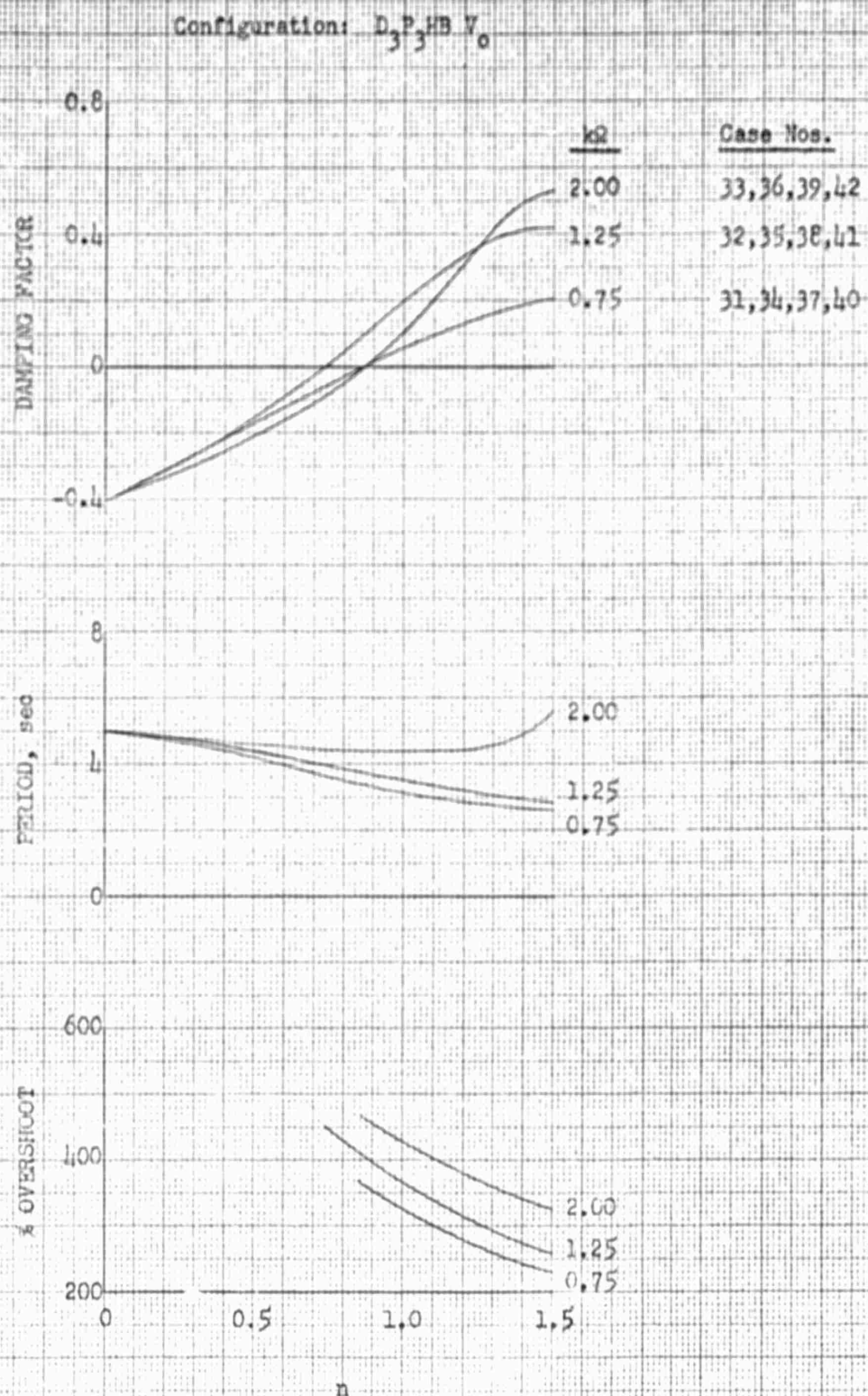
FIGURE 84: EFFECT OF GYROBAR STABILIZER ON DAMPING FACTOR, PERIOD OF OSCILLATION AND OVERSHOOT IN HOVERING WITH $\beta = 18°$ (DUCT 3)

FIGURE 85: EFFECT OF GYROBAR STABILIZER ON DAMPING FACTOR, PERIOD OF OSCILLATION AND OVERSHOOT IN HOVERING WITH $\beta = 24°$ (DUCT 3)
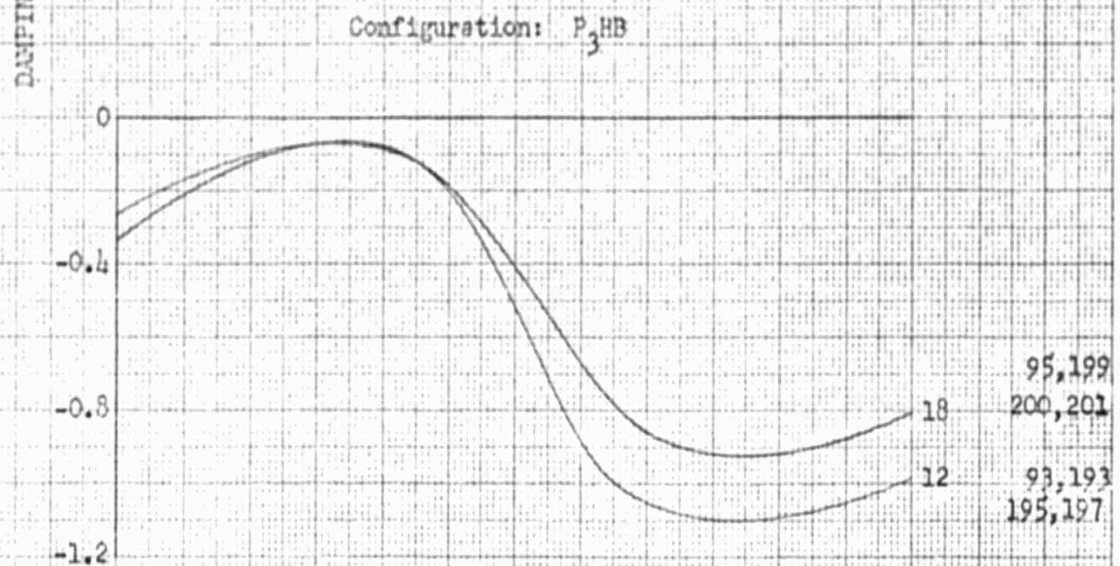
Configuration: $D_3F_3HB\ V_o$

$\beta = 12°$

n

| 0 | 0.5 | 1.0 | 1.5 |

DAMPING FACTOR

-0.4

-0.8

-1.2

kΩ

0.75

1.25

2.00
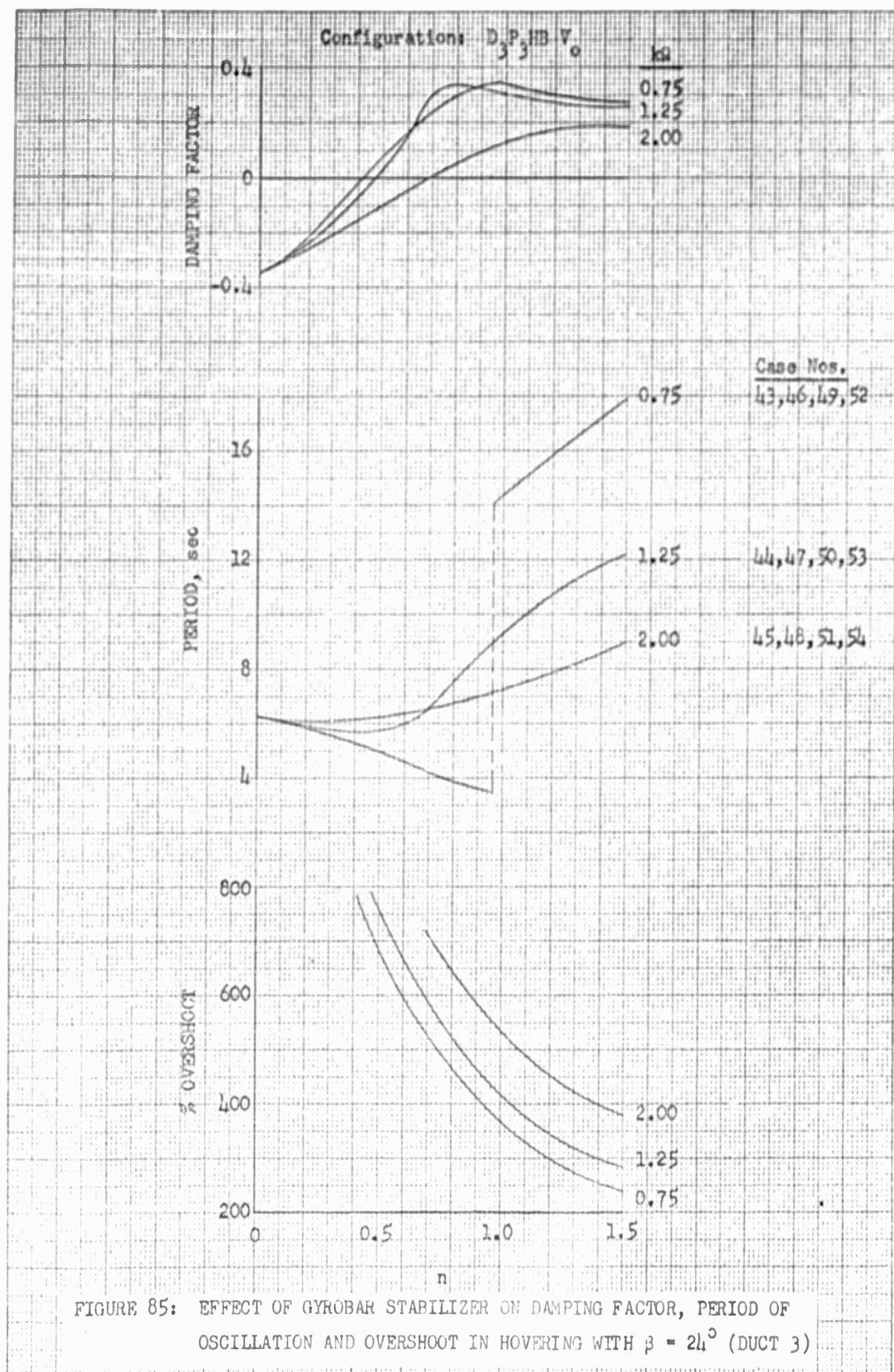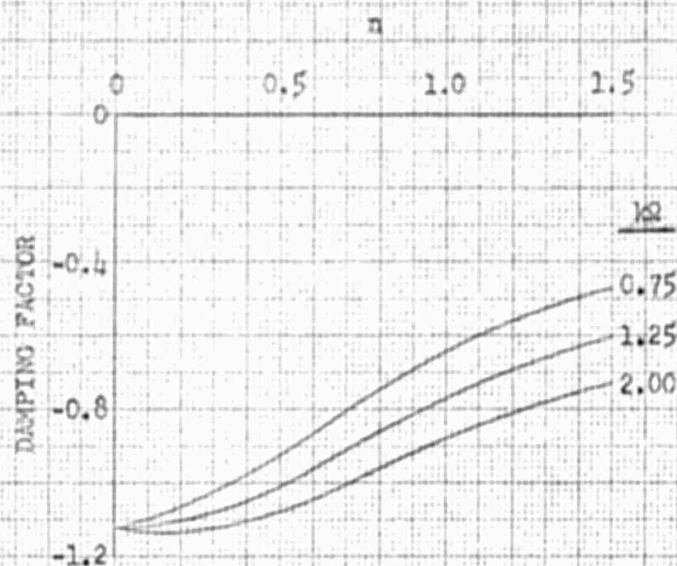
kΩ	Case Nos.
0.75	127,130,133,136
1.25	128,131,134,137
2.00	129,132,135,138

FIGURE 86: EFFECT OF GYROBAR STABILIZER ON DAMPING
FACTOR AT $\lambda = .08$ (DUCT 3)

FIGURE 87: HOVERING DAMPING FACTOR AND PERIOD OF OSCILLATION VS
PITCH SETTING (DUCTS 1, 2, 4 AND UNSHROUDED PROPELLER)

FIGURE 88: DAMPING FACTOR VS ADVANCE RATIO (DUCTS 1 AND 2)

FIGURE 89: EFFECT OF GROSS WEIGHT ON DAMPING FACTOR
AND PERIOD OF OSCILLATION (DUCT 1)

FIGURE 90: EFFECT OF MOMENT OF INERTIA ON DAMPING FACTOR
AND PERIOD OF OSCILLATION (DUCT 1)

FIGURE 91: EFFECT OF VERTICAL CG TRAVEL ON DAMPING
FACTOR AND PERIOD OF OSCILLATION (DUCT 1)

Configuration: D_1P_3HB, $\beta = 12°$

FIGURE 92: EFFECT OF DAMPING IN PITCH ON DAMPING FACTOR AND PERIOD OF OSCILLATION (DUCT 1)

Configuration: $D_1 P_3 HB$ $\beta = 12°$

FIGURE 93: EFFECT OF SPEED STABILITY ON DAMPING FACTOR
AND PERIOD OF OSCILLATION (DUCT 1)

FIGURE 94: EFFECT OF ANGLE-OF-ATTACK STABILITY
ON DAMPING FACTOR AT λ = .08 (DUCT 1)
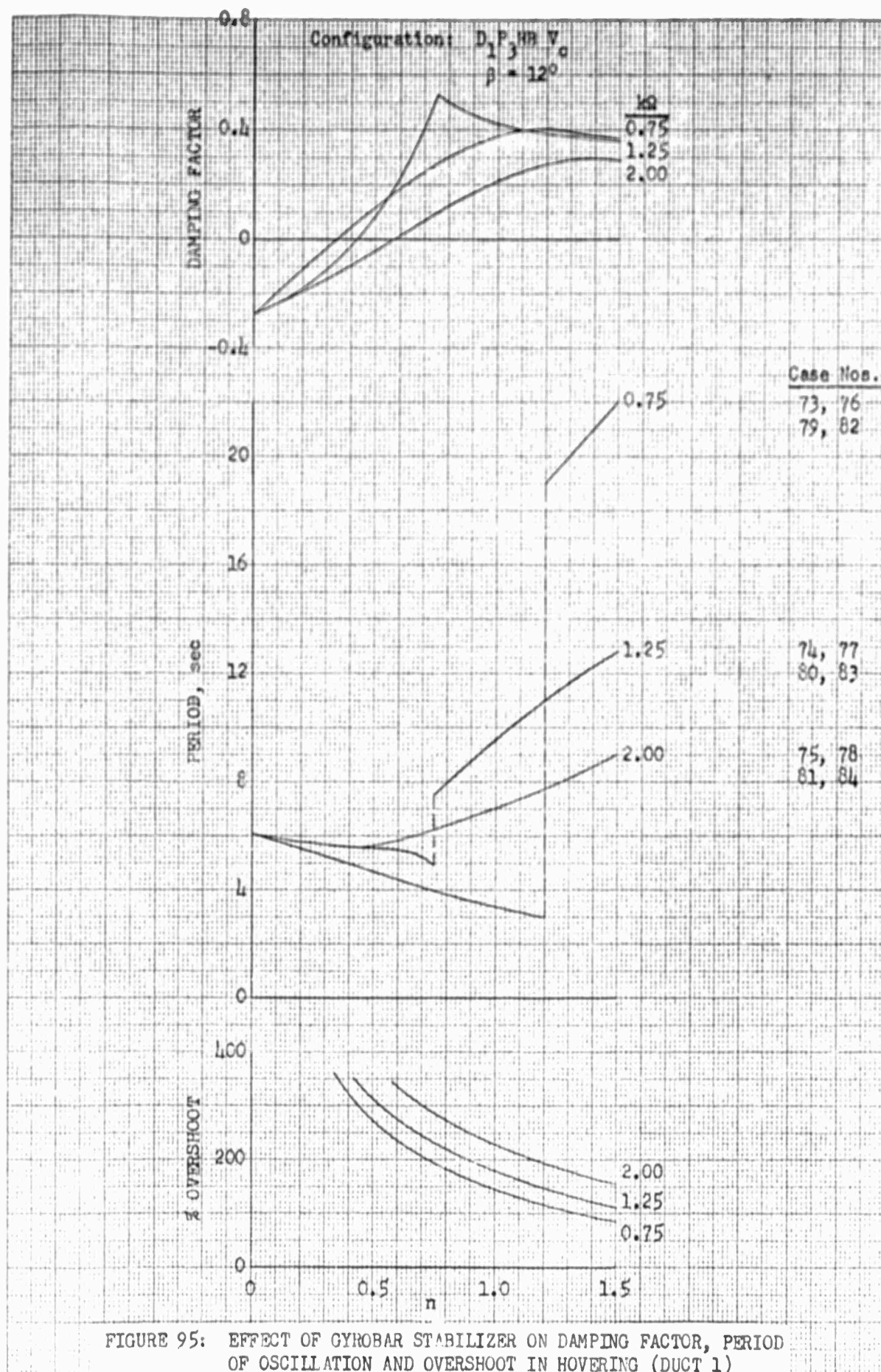
FIGURE 95: EFFECT OF GYROBAR STABILIZER ON DAMPING FACTOR, PERIOD OF OSCILLATION AND OVERSHOOT IN HOVERING (DUCT 1)
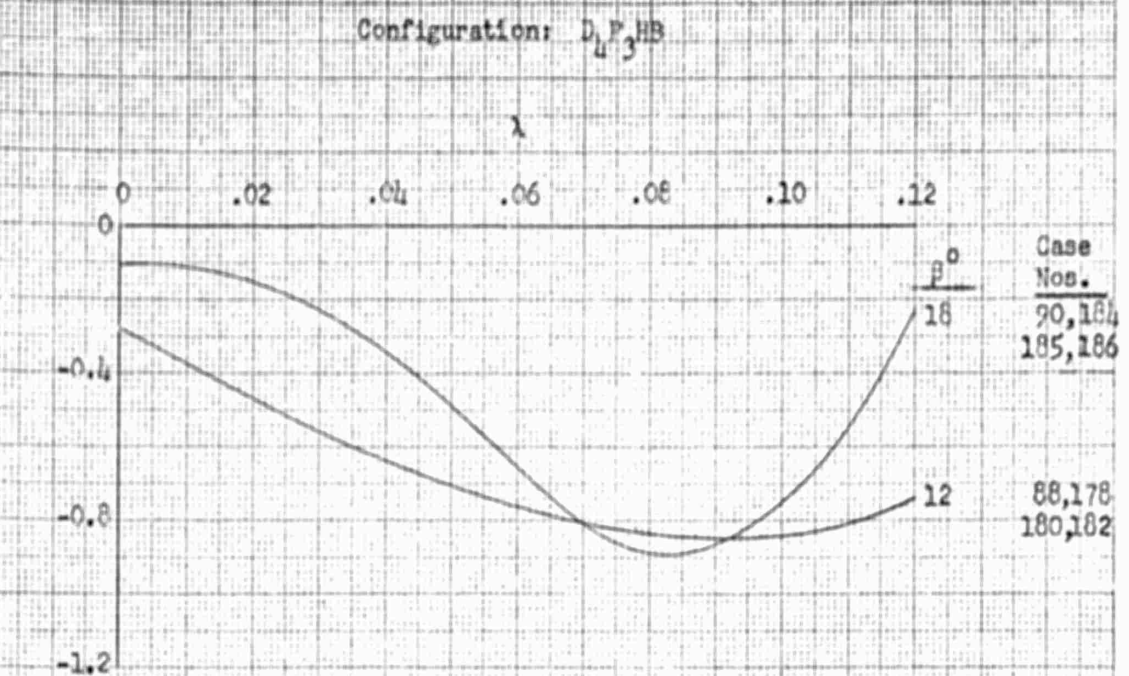
FIGURE 96:   DAMPING FACTOR VS ADVANCE RATIO (DUCT 4 AND UNSHROUDED PROPELLER)

Configuration: D_3P_3HB

$\beta = 12°$
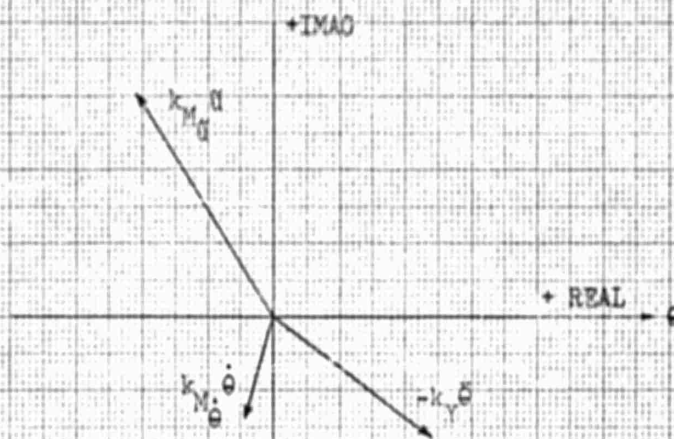
FIGURE 97:   VECTOR DIAGRAM OF MOMENT EQUILIBRIUM IN HOVERING
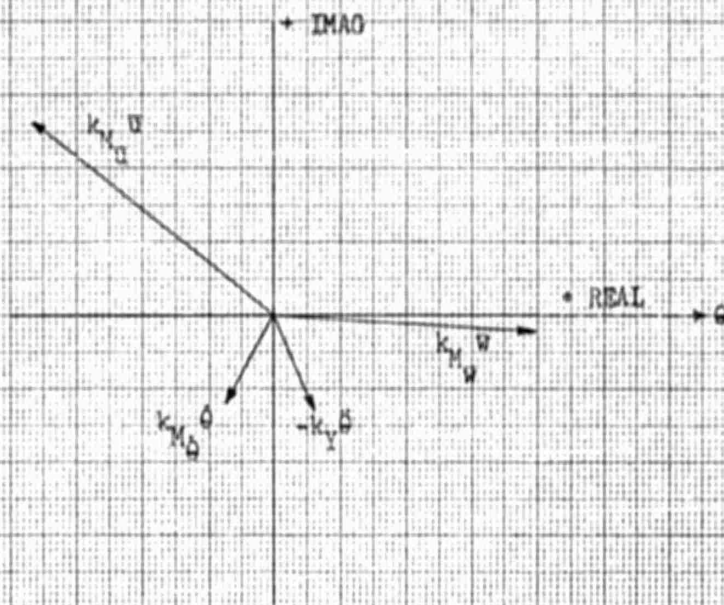
FIGURE 98: VECTOR DIAGRAM OF MOMENT EQUILIBRIUM AT $\lambda = .04$

Configuration: D_3F_3WB

$\beta = 12°$
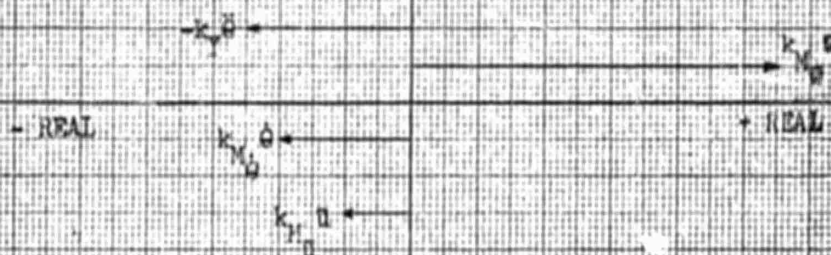
FIGURE 99: MOMENT EQUILIBRIUM AT $\lambda = .08$

FIGURE 100: VECTOR DIAGRAM OF MOMENT EQUILIBRIUM
IN HOVERING WITH GYROBAR STABILIZER
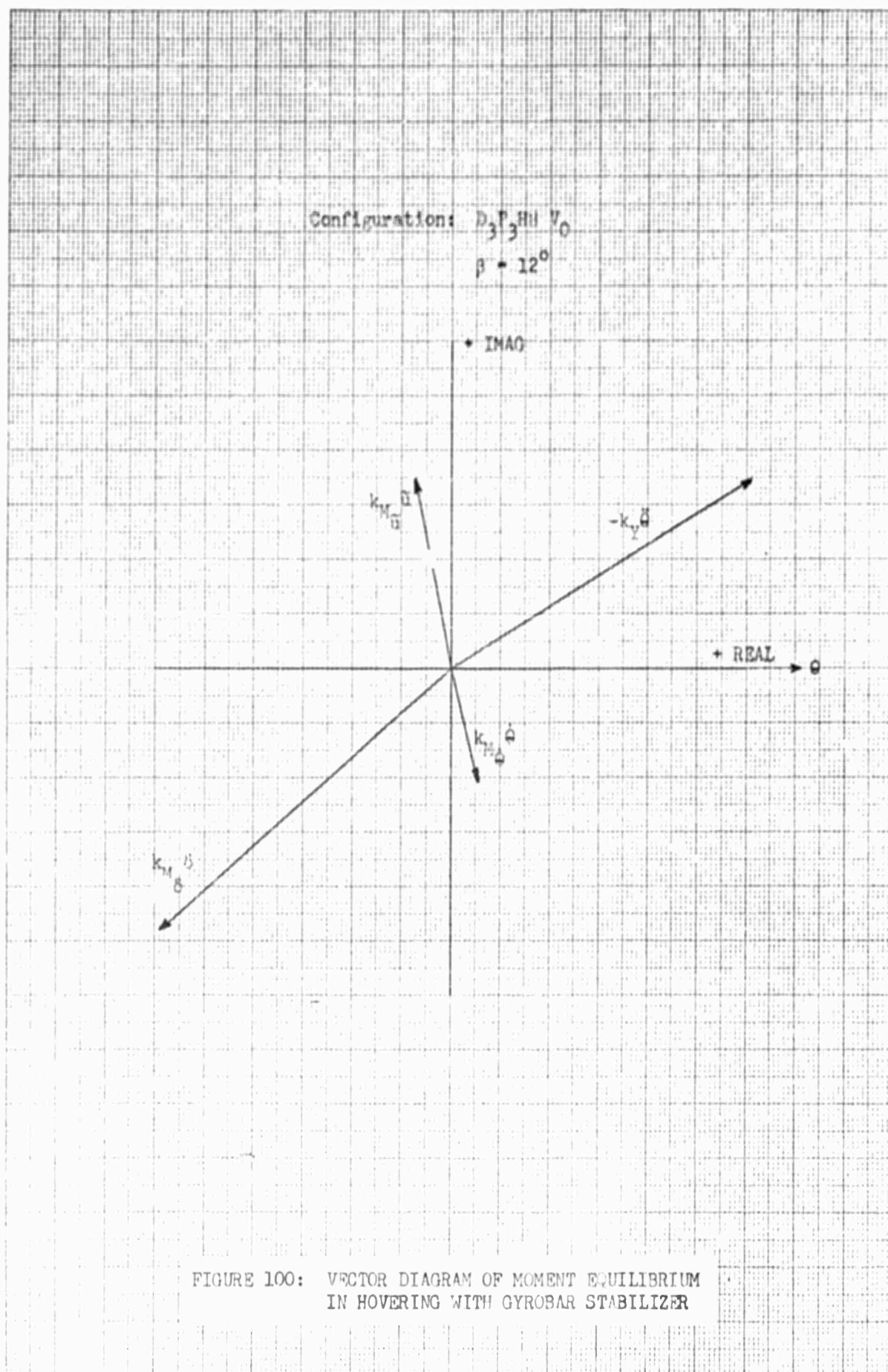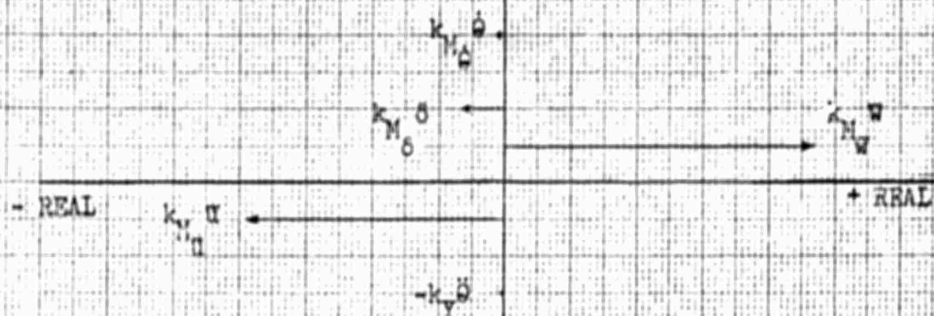
FIGURE 101: MOMENT EQUILIBRIUM AT $\lambda = .04$ WITH GYROBAR STABILIZER
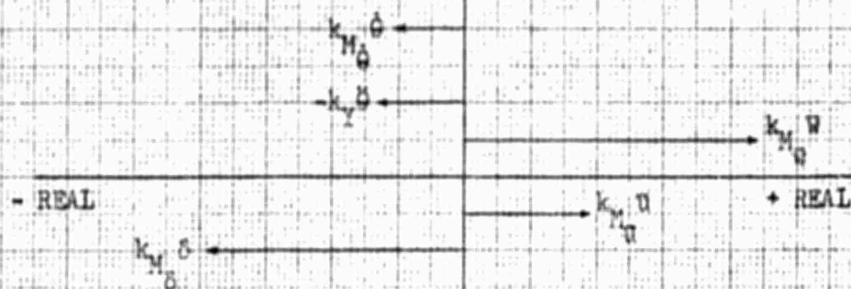
FIGURE 102: MOMENT EQUILIBRIUM AT $\lambda = .08$ WITH GYROBAR STABILIZER

$\beta = 12°$

Present ship

UNSTABLE

STABLE

k_{M_θ}

k_{H_u}

Configuration
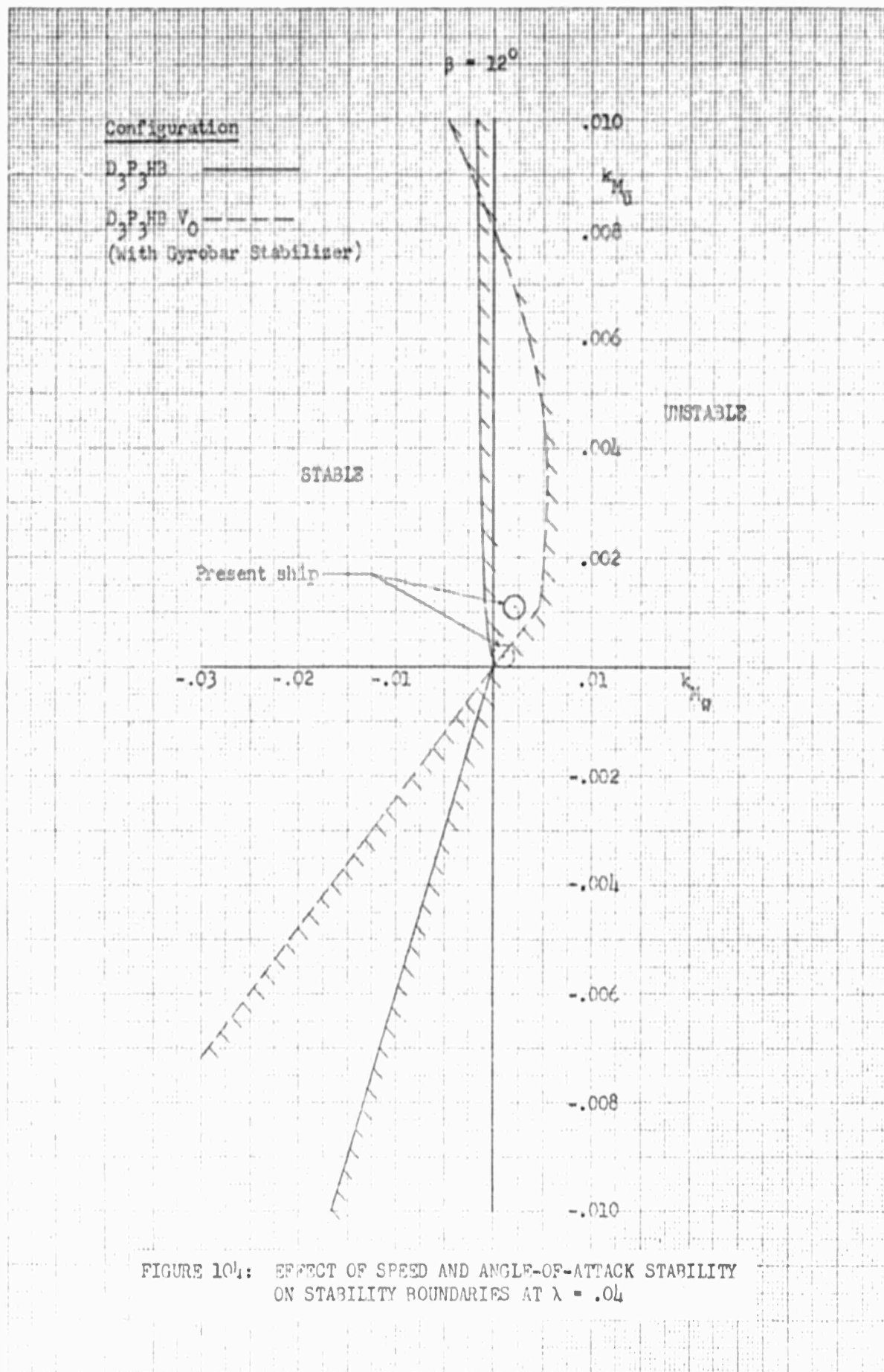
D_3P_3HB

$D_3P_3HB\ V_0$
(With Gyrobar Stabilizer)
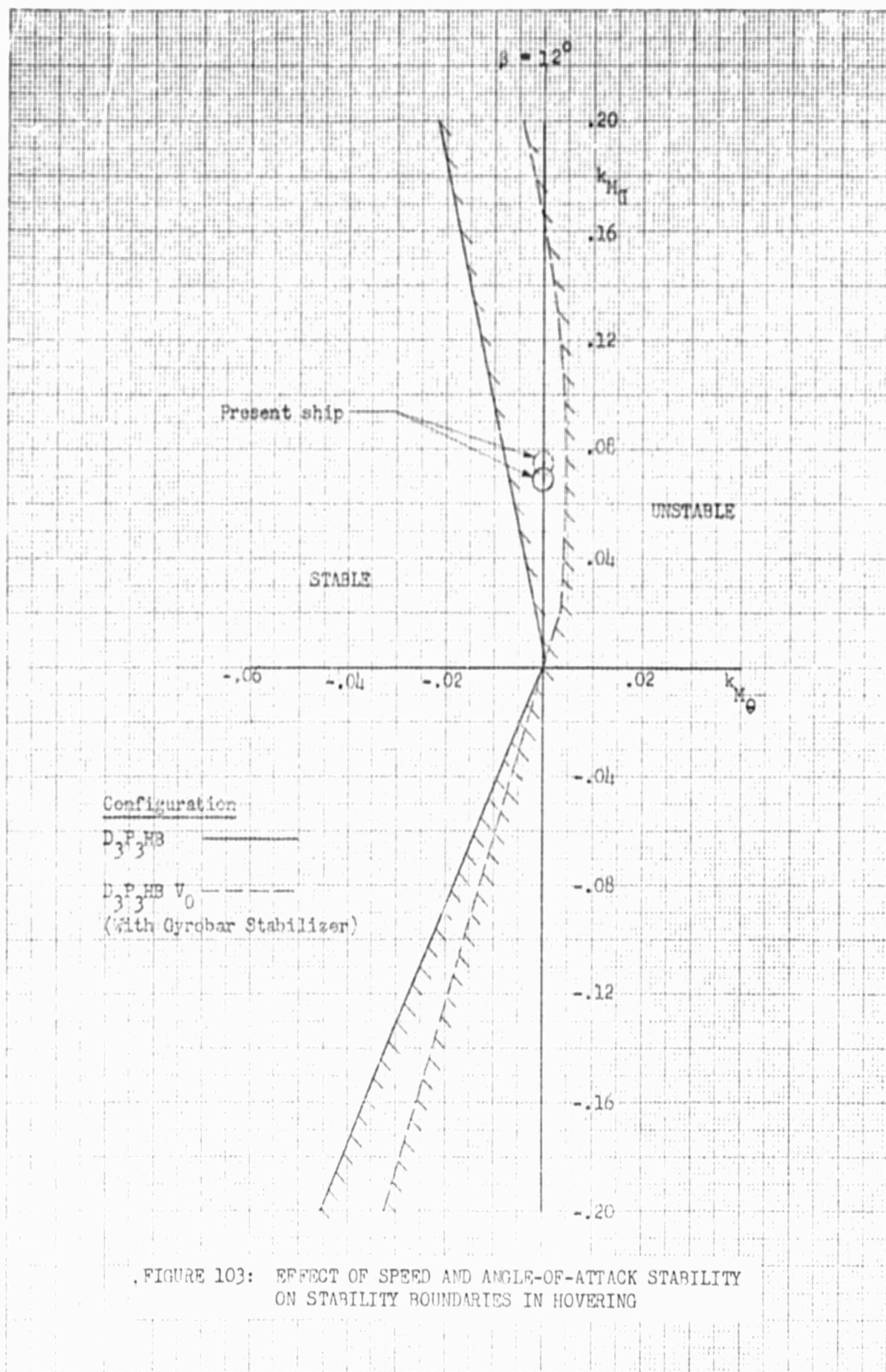
FIGURE 103: EFFECT OF SPEED AND ANGLE-OF-ATTACK STABILITY
ON STABILITY BOUNDARIES IN HOVERING

FIGURE 104: EFFECT OF SPEED AND ANGLE-OF-ATTACK STABILITY
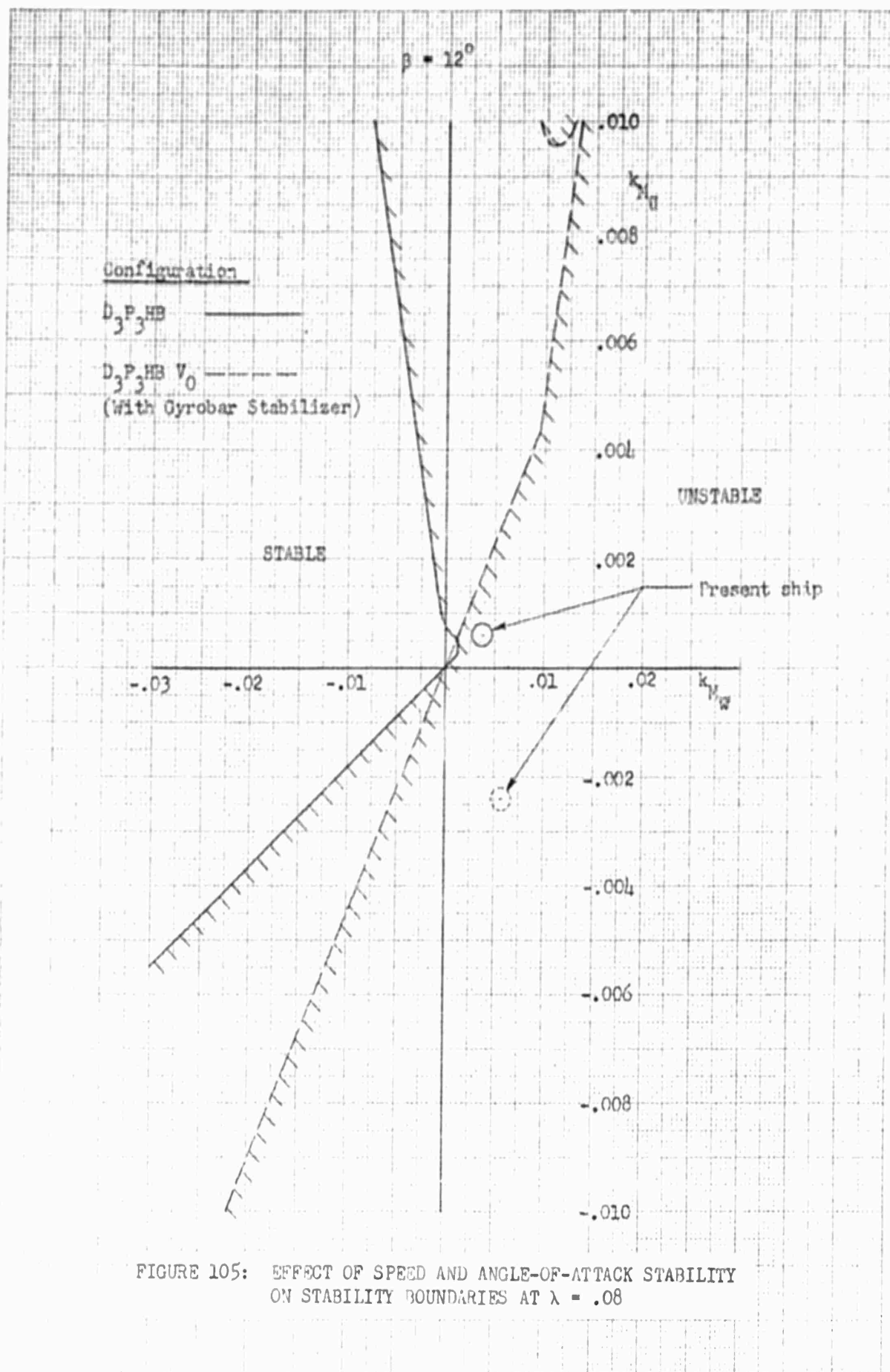ON STABILITY BOUNDARIES AT $\lambda = .04$

FIGURE 105: EFFECT OF SPEED AND ANGLE-OF-ATTACK STABILITY
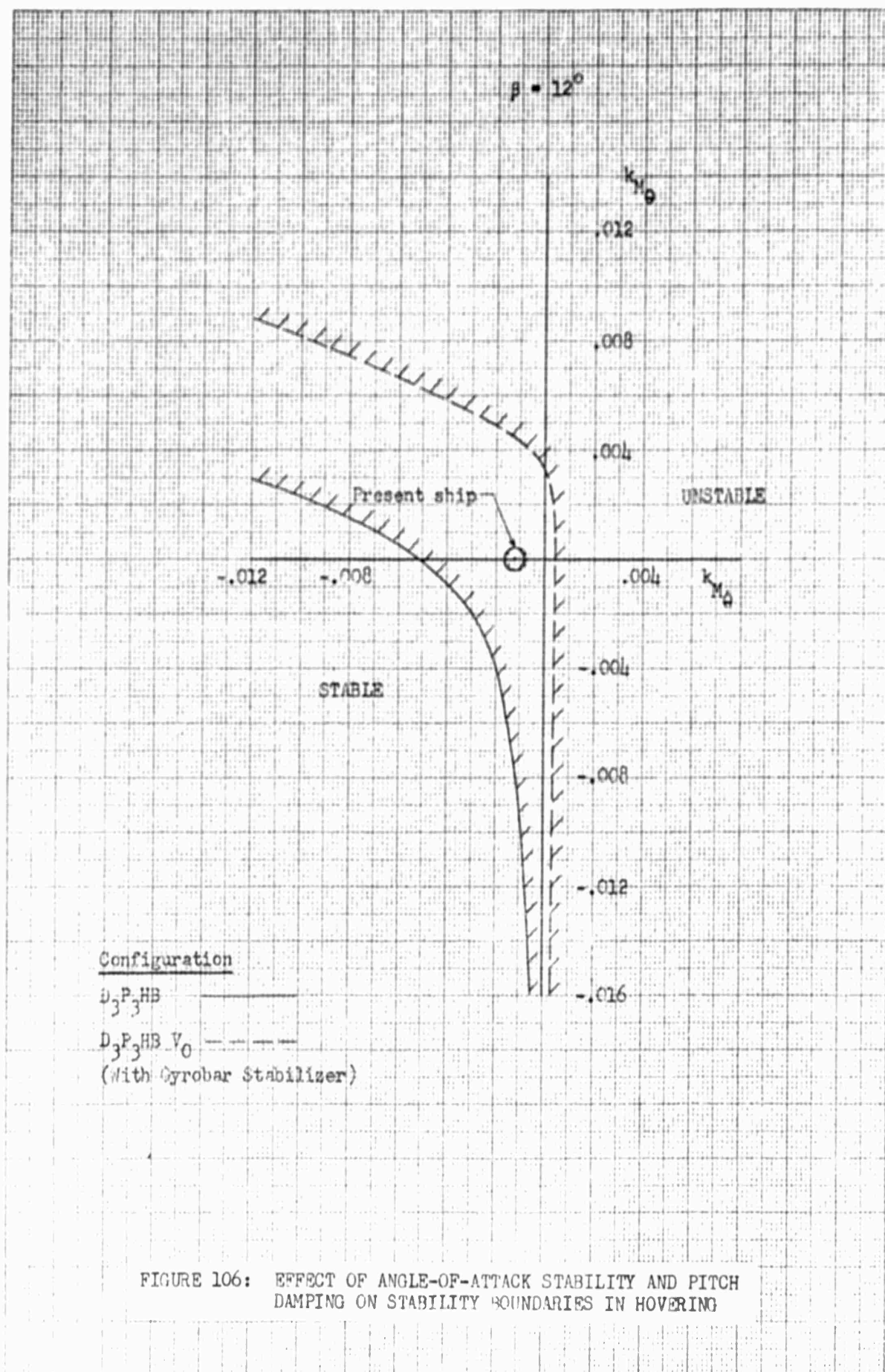ON STABILITY BOUNDARIES AT $\lambda = .08$

FIGURE 106: EFFECT OF ANGLE-OF-ATTACK STABILITY AND PITCH DAMPING ON STABILITY BOUNDARIES IN HOVERING
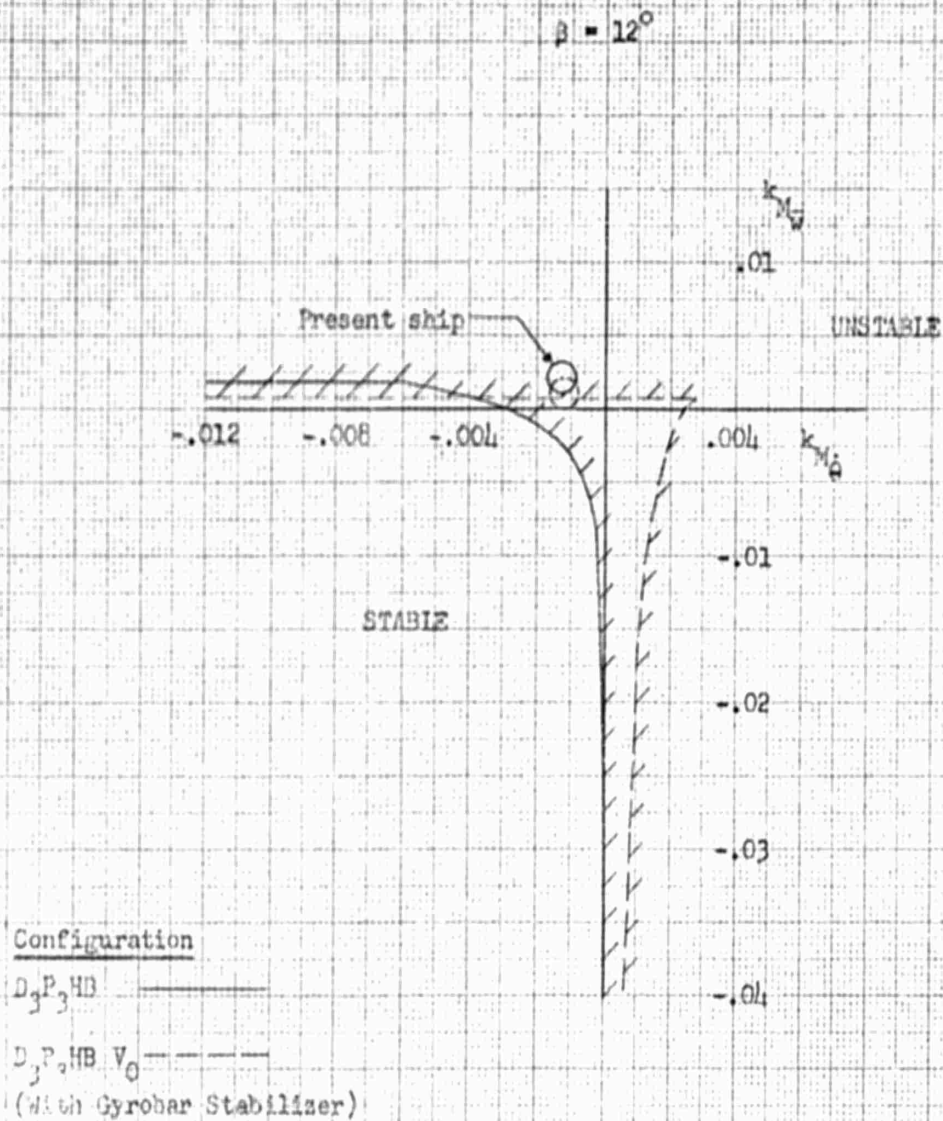
FIGURE 107: EFFECT OF ANGLE-OF-ATTACK STABILITY AND PITCH
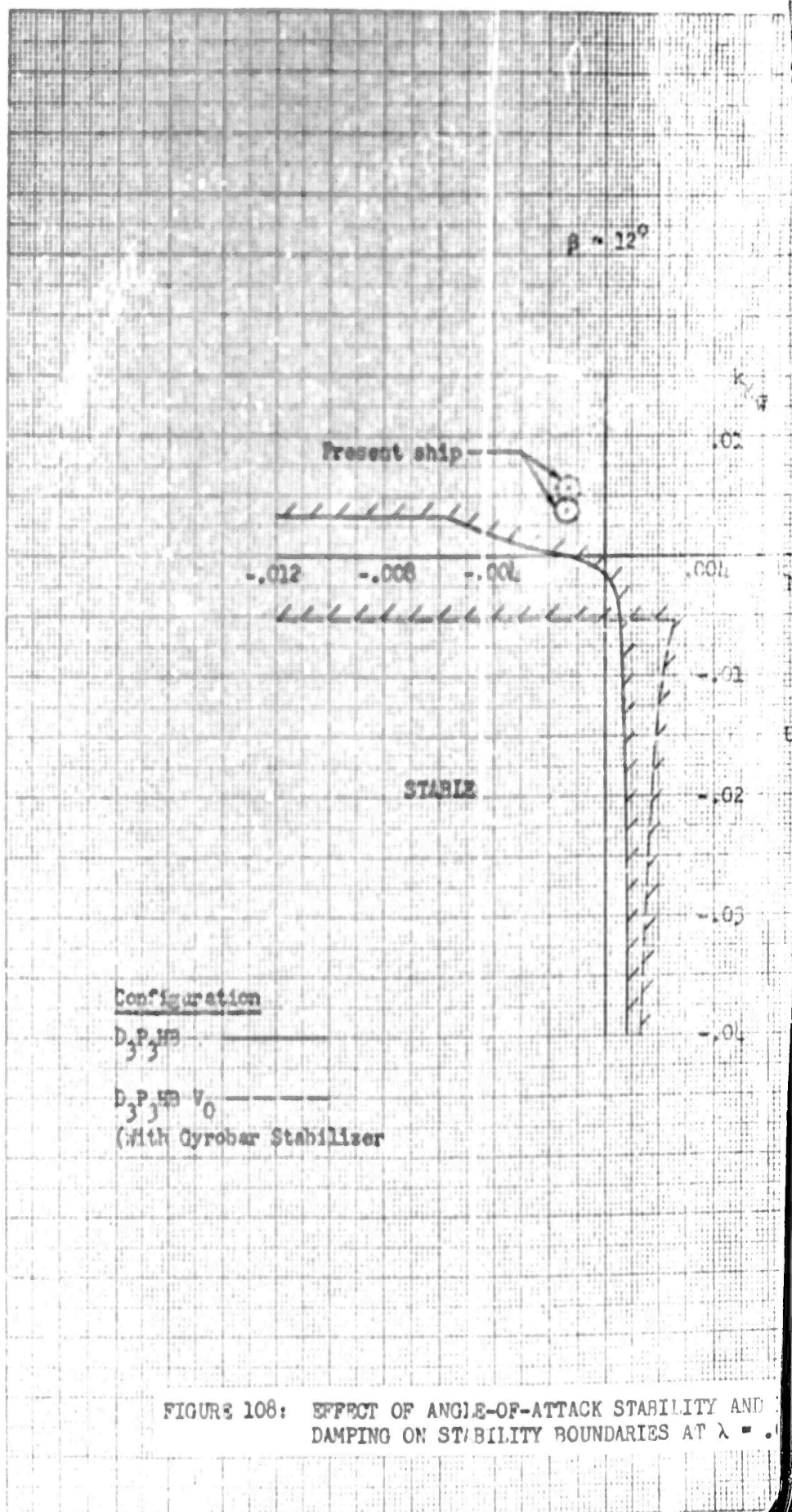DAMPING ON STABILITY BOUNDARIES AT $\lambda = .04$

FIGURE 108: EFFECT OF ANGLE-OF-ATTACK STABILITY AND
DAMPING ON STABILITY BOUNDARIES AT λ = .